UNIVERSITY OF SOUTHAMPTON

FACULTY OF ENGINEERING AND THE ENVIRONMENT

Engineering Sciences

Investigation of the Biophysical Role of Acoustic Environment for Cartilage Tissue Engineering

by

Umesh Sai. Jonnalagadda

Thesis for the degree of Doctor of Philosophy

March 2017

UNIVERSITY OF SOUTHAMPTON

ABSTRACT

FACULTY OF ENGINEERING AND THE ENVIRONMENT

Engineering Sciences

Doctor of Philosophy

INVESTIGATION OF THE BIOPHYSICAL ROLE OF ACOUSTIC ENVIRONMENT FOR CARTILAGE TISSUE ENGINEERING

by Umesh Sai. Jonnalagadda

Osteoarthritis is characterized by degradation of the articular lining in the joints and surgical measures, such as microfracture, result in mechanically dissimilar repair tissue. An alternative repair strategy utilizes tissue engineering to generate tissue *in vitro* using a combination of cells, substrates, and bio-chemical/-mechanical cues. Ultrasound has been explored as a means of applying mechanical stimulation onto the tissue and, more recently, acoustofluidics has exploited the potential of levitating cells within a fluid channel to allow 3-dimensional culture in the absence of a physical scaffold. The purpose of this research is to identify the biophysical relevance of the acoustic trap on the cells during tissue culture. A layered resonator assembly was designed to culture cell aggregates in static fluid conditions. Pellet co-culture of human articular chondrocytes and skeletal stem cells was accomplished to identify an optimal chondrogenic population to use within the acoustofluidic bioreactor. The acoustic field interactions with the cells and streaming interactions with the fluid were visualized through high-speed imaging and quantified through particle tracking and analysed by finite element modelling. The acoustic field was manipulated by modifying the driving frequency range (sweep) and cycle speed through the sweep (sweep repetition rate). The long-term effects of modulating the acoustic field was determined through 21 day tissue culture with chondrocytes and quantification of the matrix composition using histology.

The results from this thesis demonstrated more robust cartilage formation from human articular chondrocytes relative to skeletal stem cell pellets, therefore, long-term tissue culture experiments involved chondrocytes as the cell source of interest. The chondrocyte-acoustic interactions were quantified by mathematical modelling based on the experimental results at day 0. The fluid shear stress on the cells was found to oscillate and the stress amplitude varied in relation to the sweep repetition rate and frequency sweep. Following this, long-term bioreactor culture with the chondrocytes was performed at low and high stress conditions. The resulting histology demonstrated more robust cartilage development when the cells are supplied with a higher oscillatory shear and further modification of the culture environment to include parathyroid related hormone resulted in engineered cartilage structurally and mechanically similar to native cartilage. The conclusion from this thesis is that the acoustic field is a tunable system with biomechanical relevance that, combined with relevant biochemical factors, allows for the culture and development of hyaline-like cartilage and potentially other cell types.

Contents

List of Figures

List of Tables

Nomenclature

α-MEM α-modification minimal essential media

β	Compressibility
λ	wavelength
μ	Dynamic viscosity
ν	Kinematic viscosity
ω	Angular frequency
Φ	Acoustic contrast factor
ρ	Density
τ	Fluid Shear Stress
θ	Angle
v	incident unperturbed and uniform acoustic field velocity
a	Particle radius/length
c	Speed of sound
E_{ac}	Acoustic energy density
f_1	Monopole scattering coefficient
f_2	Dipole scattering coefficient
F_B	Bjerknes forces
F_{rad}	Acoustic radiation force

k Wavenumber

p_{ac} Acoustic pressure

U^{rad} Acoustic radiation potential energy/Gor'kov potential

V_o Velocity amplitude

Ocn Osteocalcin (gene from mouse)

Opn Osteopontin (gene from mouse)

ACI Autologous cell implantation

ACL Anterior Cruciate Ligament

AEC 3-amino-9-ethylcarbazole

Akt Protein kinase B

ALP Alkaline phosphatase

BSA Bovine serum albumin

CACI collagen-membrane ACI

CFU-F Colony forming unit-fibroblastic

COL Collagen

COX2 Cyclooxygenase-2 (gene from human)

CTGF Connective tissue growth factor

Cyr61 Cysteine-rich angiogenic inducer 61

d Interparticle distance, centre-to-centre

DPX Colony forming unit-fibroblastic

EB Embryoid body

ECM Extracellular matrix

ERK Extracellular signalregulated kinase

ESC Embryonic stem cell

FAK Focal adhesion kinase

FBS Fetal bovine serum

GAG Glycosaminoglycan

GPCR G-protein couple receptor

HAC Human articular chondrocytes

HCl Hydrochloric acid

HIFU High-intensity focused ultrasound

iPSC Induced pluripotent stem cell

ITS Insulin Transferum Selenium

LIDUS Low-intensity diffuse ultrasound

LIFUS Low-intensity focused ultrasound

LIUS Low-intensity ultrasound

MACI matrix-induced ACI

MACS Magnetically activated column separation

MAPK Mitogen-activated protein kinase

MPIV PIV toolbox for MATLAB

MSC Mesenchymal stem cell

OA Osteoarthritis

OPN Osteopontin (gene from human)

PBS Phosphate-buffered saline

PI3K Phosphoinositide 3-kinase

PIV Particle image velocimetry

PSC Pluripotent stem cell

PTHrP Parathyroid homormone-related protein

RT-qPCR Real time quantitative-polymerase chain reaction

Sox9 SRY (sex determining region Y)-box 9

SSC Skeletal stem cells

STRO-1 Trypsin resistant antigen 1

TGF-β Transforming growth factor beta

TGF-β3 Transforming growth factor beta-3

US Ultrasound

USWF Ultrasonic standing wave field

YAP Yes-associated protein

Acknowledgements

I would like to thank my supervisors for their patience and guidance in helping me develop this final thesis, as well as the various members of the Ultrasonic Wave and Bone and Joint groups for their assistance and further insight into the theories and practices I have employed for my experiments. Additionally, my parents Radha and Prasad Jonnalagadda for their love and support over the past two and a half decades to bring me to this point and beyond. Last and most importantly, I want to acknowledge ChinYee Ho, whose support and assistance were always a guiding light over the years, even in the darkest of times.

Declaration of Authorship

I, Umesh Sai. Jonnalagadda , declare that the thesis entitled *Investigation of the Biophysical Role of Acoustic Environment for Cartilage Tissue Engineering* and the work presented in the thesis are both my own, and have been generated by me as the result of my own original research. I confirm that:

- this work was done wholly or mainly while in candidature for a research degree at this University;
- where any part of this thesis has previously been submitted for a degree or any other qualification at this University or any other institution, this has been clearly stated;
- where I have consulted the published work of others, this is always clearly attributed;
- where I have quoted from the work of others, the source is always given. With the exception of such quotations, this thesis is entirely my own work;
- I have acknowledged all main sources of help;
- where the thesis is based on work done by myself jointly with others, I have made clear exactly what was done by others and what I have contributed myself;

Signed:.....

Date:.....

Chapter 1

Introduction

1.1 Background and Relevance

Articular cartilage is an avascular, alymphatic, and aneural tissue that covers the ends of bones and enables smooth joint movement by acting as a low friction shock absorber [1, 2]. Cartilage consists of chondrocytes, which are sparsely distributed throughout the tissue, but nonetheless important in maintaining the extracellular matrix (ECM) and mechanical properties of the tissue [3]. As a result of the avascular nature of the tissue, the articular lining has a limited self-repair capacity. As such, defects within the articular lining can lead to changes in the cartilage structure and ultimately osteoarthritis (OA), a disease characterized by deterioration of the articular lining of the joints. Present surgical treatment options—such as microfracture, mosaioplasty, and variants of autologous chondrocyte implantation (ACI)—involve further damage the articular lining to harvest cells and tissue to re-implant into the major defect site(s). As the biological material would be harvested from less damaged, or non-load bearing regions of the tissue lining, the repair tissue would be either less well formed or mechanically dissimilar to the surrounding tissue. As a result, the structural stability will be compromised, leading to degradation of the repair tissue and further damage and thinning of the native articular lining. The limited sustainability of present treatment options motivates the exploration of other, more robust treatment options. For this reason, researchers have investigated the potential of generating cartilaginous tissue *in vitro* for eventual implantation via the field of tissue engineering.

Tissue engineering aims to repair, maintain, or enhance native, host tissue [4, 5]. These goals are accomplished through the *in vitro* culture of cells, supported by the application of appropriate growth factors, scaffolds, and bioreactor system to generate a tissue structure for the eventual implantation into patients. To date, several groups have shown promising results in developing various tissue structures, such as bone [6, 7] and cartilage [6, 8]. In the case of cartilage engineering, literature has shown that it is possible to generate the tissue from a variety of modalities—from deposition printers [9, 10] to micro-scale bioreactors [11] and stackable cell sheets [12, 13].

In an effort to generate robust cartilage, recent work reports tissue culture which subject the cells to various physicochemical influences [14, 15]. Most notably, hydrostatic, cell stretching, and other forces have been used to activate mechanotransduction pathways and promote chondrogenesis in the cells [16, 17]. It has been reported that dynamic stimulation (e.g. cyclic shear or dynamic compression) of the cells results in generation of more robust cartilage, compared to stimulating cells with static forces [16]. Dynamic and cyclic stimulation has generally been exerted through cell stretching on flexible membranes or manipulation of the pressure within the culture system.

In recent years, cell manipulation through acoustic fields has been discussed in the field of bio-acoustofluidics using ultrasonic standing wave fields (USWFs). USWFs, or acoustic traps, have been shown to have potential to alter the cellular or substrate structure [18–21] through either surface or bulk acoustic wave (SAW and BAW, respectively) configuration in a microfluidic system. Literature has shown a number of trap configurations for both SAW and BAW-based traps for cell manipulation, and on BAW-based systems for vascular and cartilage tissue development [21, 22], and preliminary findings in engineering functional hepatocyte and neuronal aggregates within scaffold-based and scaffold-free methodologies [23, 24].

A recent advancement in bioacoustofluidics has been the continuous perfusion-based culture of chondrocytes within an acoustofluidic bioreactor [22]. This study discusses the potential of acoustic forces to trap and levitate chondrocytes to from a 3-dimensional cluster, which is viable and capable of secreting relevant matrix proteins to create a functional cartilage construct following 21 days of active culture. Another study has also expressed how acoustic force modulation can mechanically deform cells

[25], thus, suggesting that the acoustic standing wave field may be mechanically relevant for a biological system.

1.2 Objectives and Aims

Given that the acoustic forces within the culture environment are mechanical forces that may influence chondrogenesis, the primary aim of this thesis is to characterize and understand how manipulation of the acousto-mechanical environment can affect the cells and resulting tissue. To address this aim, the specific objectives of the study are:

1. Identification of an optimal cell source from a population of human primary chondrocytes and STRO-1 selected skeletal stem cells, which is capable of generating robust cartilage. This would be accomplished using pellet culture, a well established technique for developing cartilage tissue models.
2. Design and application of an acoustofluidic bioreactor for high-throughput and reproducible tissue engineering using the acoustic field as the only source of biomechanical stimulation and media exchange.
3. Parametric analysis of the biomechanical forces exerted onto the cells and fluid motion within the trap as a result of streaming. Determination of these forces will be accomplished by particle tracking algorithms to obtain spatially-averaged displacement vector fields, which will then be introduced into a computational model to assess the stress and flow magnitude within the fluid layer of the trap.
4. Parametric analysis of modulating acoustic forces on the cells and histological assessment of the resulting tissue and matrix composition.

1.3 Research Contributions

This thesis provides novel contributions in the following areas:

1. Analysis of co-culture performance of human chondrocyte and STRO-1+ skeletal stem cells.

2. System characterization by image analysis and computational modelling of the acoustic environment to provide mechanical stimulation onto cells during culture.

3. Biological quantification by histology and nano-indentation of the biomechanical role of the acoustic environment on cartilage engineering.

Additionally, the following papers are in preparation (projected publication in 2017) from the work developed in this thesis:

1. Jonnalagadda, U. S.; Messaoudi, W.; Cook, R. B.; Oreffo, R. O.; Hill, M. & Tare, R. S. Acoustically modulated mechanical stimulation bioreactor for the growth of tissue-engineered cartilage *Nature Communications*, **2017**

2. Jonnalagadda, U. S.; Oreffo, R. O.; Hill, M. & Tare, R. S. Bioacoustofluidics for Tissue Engineering and Biological Function *Lab on a Chip*, **2017**

The following publications have also been contributed to and the methods within to further the current thesis work:

1. Zmijan, R.; Jonnalagadda, U. S.; Carugo, D.; Kochi, Y.; Lemm, E.; Packham, G.; Hill, M. & Glynne-Jones, P. High throughput imaging cytometer with acoustic focusing *RSC Advances*, **2015**, 5, 83206-83216

2. Li, S.; Glynne-Jones, P.; Andriotis, O. G.; Ching, K. Y.; Jonnalagadda, U. S.; Oreffo, R. O.; Hill, M. & Tare, R. S. Application of an acoustofluidic perfusion bioreactor for cartilage tissue engineering *Lab on a Chip, Royal Society of Chemistry*, **2014**

1.4 Layout of Thesis

Chapter 2 summarizes the background literature of the thesis, specifically, the clinical relevance of the research and how ultrasound is currently being implemented for bioengineering, including mechanotransductive pathways. The results from this thesis have been partitioned into three chapters; Chapter 3 discusses the use of stem cells and chondrocytes to find an optimal cell population for robust cartilage generation.

Chapter 4 details the thought process involved in designing the final acoustofluidic bioreactor system and Chapter 5 discusses the mechanical and biological findings from the bioreactor culture. Finally, Chapter 6 summarizes the conclusions from the results chapters and potential future work that can be accomplished from this thesis work.

Chapter 2

Literature Review

2.1 Overview

This literature review is divided into four main sections: the first section provides an overview of hyaline cartilage physiology and how thinning of the articular lining may lead to osteoarthritis. In the second section, cartilage tissue engineering methods have been summarized. The third section details physical acoustic theory and phenomena, including their biological relevance. Additionally, this section discusses how acoustics has been implemented for bioengineering and tissue engineering. The final section provides a brief discussion of the cell sources presently used for cartilage engineering and chondrogenesis.

2.2 Articular Cartilage Physiology and Structure

The primary function of cartilage is to provide structural and mechanical support. The tissue is generally characterized as an avascular, alymphatic, and aneural structure and the matrix composition further classifies the tissue as elastic cartilage, fibro-cartilage, fibro-elastic and hyaline cartilage [1, 2, 26]. Articular cartilage is a specialised type of hyaline cartilage that functions as a low-friction surface to allow for smooth articulation. Articular cartilage is also organized into distinct regions where the cellular morphology and the matrix composition differ from the surface to the deep layer (Figure 2.1). Cartilage consists of chondrocytes, which are sparsely distributed throughout the tissue, but nonetheless important in maintaining the extracellular matrix (ECM) and mechanical properties of the tissue [3]. The matrix of articular cartilage comprises of a network of collagen and proteoglycans. The collagen network consists of types II, VI, IX, X, and XI. Collagen type II comprises most of the cartilage structure and contributes to its tensile strength. Collagen Type IX and XI regulate fibril size, network cross-linking, and interaction with proteoglycans [3, 27]. Aggrecan is the main proteoglycan found in articular cartilage, which consists of a protein core with negatively charged chondroitin sulfate and keratin sulfate glycosaminoglycan (GAG) chains branching out from the core [27]. The polar charge of the GAG chains allows aggrecan to trap water molecules within the matrix, which can assist in translating the compressive load from the surface to the deeper regions of the tissue. Both the collagen network and proteoglycan concentration vary between the surface and deep layer that affects mechanical loading and also changes how the cells react to applied loads [27].

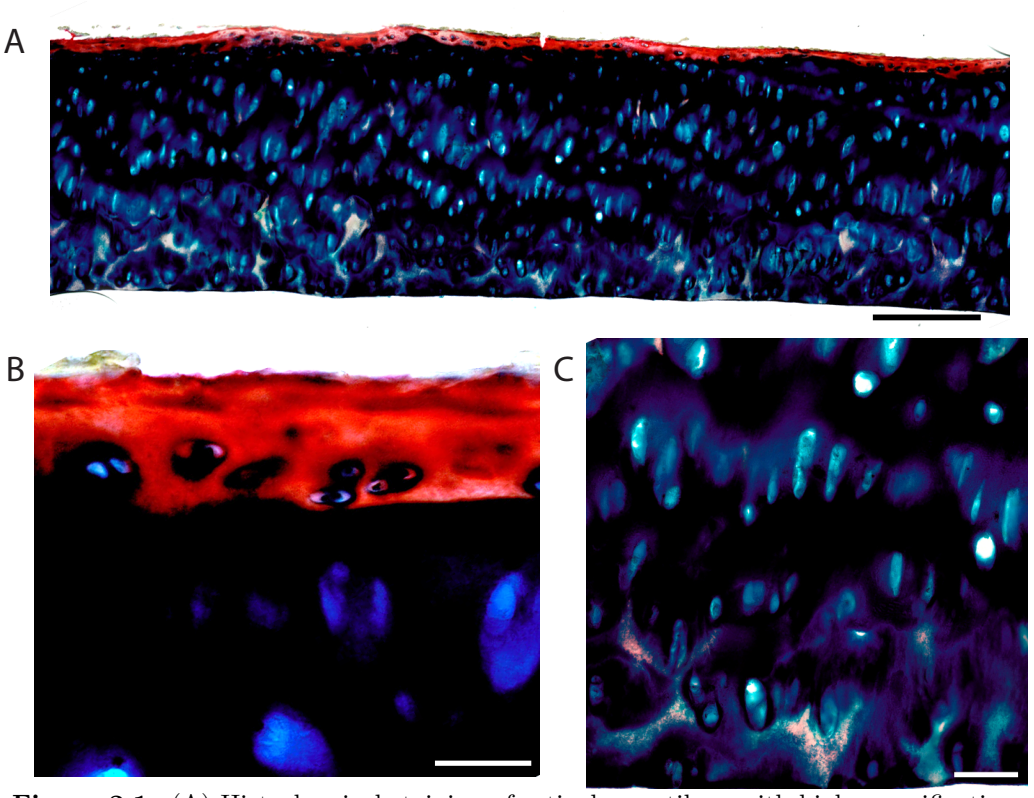

Figure 2.1: (A) Histochemical staining of articular cartilage with high magnification images of the (B) superficial layer and (C) deep layer. Scale bars are (A) 500 µm and (B, C) 100 µm.

The superficial layer of the tissue contributes to approximately 10%–20% of the total thickness of articular cartilage [27]. Because the articular surface interacts with other surfaces in the joint, the collagen fibrils are oriented parallel to the surface in order to withstand the shear and tensile loading [27]. Additionally, the cells within this zone are flat and clustered together. They secrete lubricin, a proteoglycan which functions in lubricating the surface [26–28]. Towards the middle layer (20%-70% of the total thickness), the cells are more randomly distributed and spherical in structure. The collagen network is typically randomly organized and overall serves to transition to the deep layer, where the fibrils are oriented perpendicularly to the subchondral bone [27, 28]. Collagen type X is also found in the deeper matrix, which is indicative of hypertrophic cartilage. As such, cells in this layer are also larger and organized into columns [28].

2.3 Osteoarthritis

Given that articular cartilage is avascular in nature, the tissue's self-repair capacity following injury is limited. As such, defects within the articular lining can lead to changes in the cartilage structure and ultimately osteoarthritis (OA), a disease characterized by deterioration of the articular lining of the joints, typically in older patients.

Due to the ageing process, chondrocytes may experience decreased anabolism and the tissue will begin to accumulate advanced glycation end products [28]. The end result of these cellular and tissue-level changes is increased stress and enhanced collagen cross-linking with ageing, which alters the tissue mechanics and composition. The altered tissue structure generates lesions along the tissue, which further cause damage to the tissue (Figure 2.2). These lesions are categorized as microfractures and chondral defects, the severity of which is classified using various scaling systems, such as the Outerbridge Classification System [14]. For this system, grade 0 (Figure 2.3A) is considered normal cartilage structure while grade I defects exhibit swelling and softening of the articular cartilage [14]. Grades II–IV (Figure 2.3B–C) refers to chondral defects of increasing size and depth with Grade IV (Figure 2.3D) referring to lesions penetrating the subchondral bone [14].

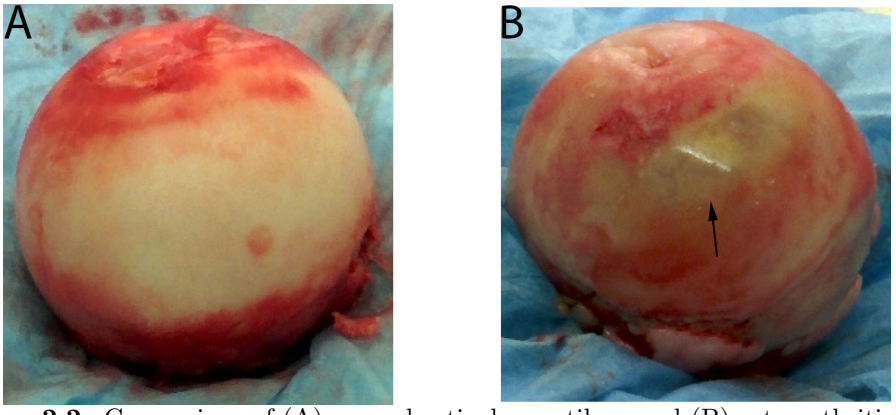

Figure 2.2: Comparison of (A) normal articular cartilage and (B) osteoarthritic cartilage in femoral heads. OA cartilage is thinner to non-existent in some regions, thus exposing the underlying subchondral bone (arrows), relative to normal cartilage.

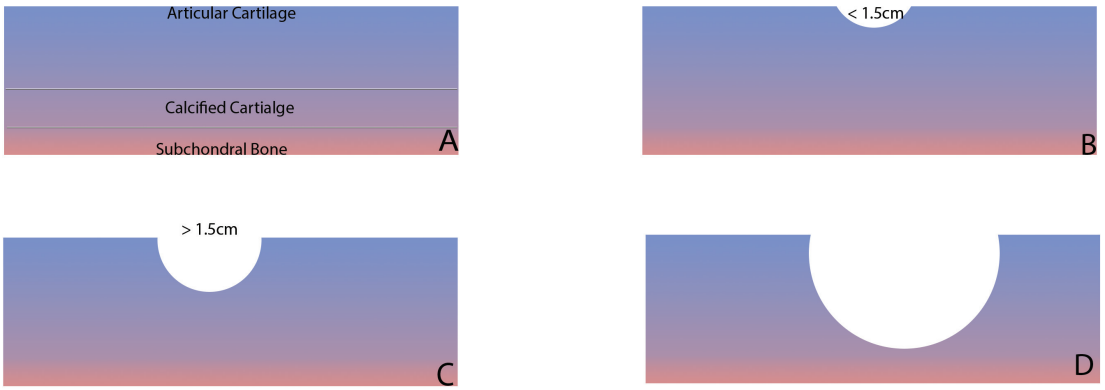

Figure 2.3: Outerbridge classification system chondral defects. (A) Grade 0 to indicate normal cartilage. (B) Grade II defects are classified as chondral lesions 1.5cm in diameter. (C) Grade III defects are chondral lesions greater than 1.5cm in diameter. (D) Grade IV refers to lesions penetrating the subchondral bone (osteochondral defects).

In the case of Grade II (Figure 2.3B), or partial thickness defects, the damage remains within the cartilage and given the avascular nature of the tissue, self-repair is limited. In contrast, full-thickness defects (Grade III, Figure 2.3C) penetrate the underlying bone, thereby allowing access to vasculature and bone-marrow derived stem cells to initiate self-repair. The resulting scar tissue is, unfortunately, mechanically inferior to hyaline cartilage. In either case, the tissue structure is further affected and the cartilage degrades over time. As the cartilage structure degrades, patients exhibit stiffer articulation and joint pain. Other than age, OA can manifest through trauma to the articular surface as a result of direct injuries to the tissue (e.g. fracture or excess loading) or induced by surgery (iatrogenic injuries) [29].

It has been reported that specific signalling pathways and biomechanical factors promote OA onset and propagation [29, 30]. Specifically, changes to loads and moments along the joint surface initiate cartilage degradation and propagation of OA in the hip, knee and foot/ankle [29]. The articular surface is categorized into the load bearing and non-load bearing regions, the latter of which is thinner and less mechanically resistant to contact loads. It is important, therefore, to understand how loading changes along articular cartilage influences the bearing and non-load bearing regions during OA propagation.

For healthy patients undergoing a walking cycle, the femur simultaneously rotates and translates over the articular surface of the tibia and most of the loads are absorbed by the lateral facet of the tibia. In contrast, OA patients experience increased femoral

rotation relative to the translational motion of the condyle along the tibial plateau [29]. This change in movement alters loading in the joint from the lateral facet to the medial facet of the tibia. As the loading patterns along the articular surface shifts to the non-load bearing tissue, the tissue undergoes fibrillation of the collagen network and the force changes also alter cell signalling. The combined matrix and pathway changes ultimately result in degradation of the cartilage and further loading changes as OA progresses [29]. The reason for this change is typically a result of failure of the anterior cruciate ligament (ACL), which stabilizes the knee during flexion/extension [29]. It should be noted that both ACL injury as well as reconstruction of the ligament can alter the kinematics within the knee as the original stability cannot be fully restored [29]. Adduction or specifically, the resulting load distribution across the tibial plateau during gait has been reported to be correlated with OA progression. Increased loading along the medial side of the tibia, due to vargus deformity (bow-legged) or malalignment, has been associated with OA progression and can serve as a marker for disease onset [29].

2.3.1 Current Treatments

Given that the defects within damaged cartilage do not heal spontaneously, certain surgical repair strategies, such as microfracture, involve further damaging the joint in order to reach the underlying subchondral bone to promote self-repair[31, 32]. Unfortunately, this strategy can lead to formation of scar tissue in the defect site, which is mechanically dissimilar from normal cartilage. Subsequently, this can further intensify degeneration of the cartilage and create full thickness defects [2]. Repair of articular cartilage through the use of autologous transplantation techniques, such as mosaioplasty and autologous cell implantation, is possible; however, the implanted cartilage is typically harvested from non-load bearing sources within the patient [31]. As a result, the implanted tissue may be mechanically compromised and, due to the nature of autologous transplants, the possibility of donor site morbidity is introduced, which can further exacerbate the patient's condition [27].

Autologous cell implantation (ACI) is a well established treatment for articular cartilage lesions [33]. The procedure involves obtaining a biopsy from non-load bearing cartilage to harvest the chondrocytes and expand in culture. A secondary procedure is

then undertaken to clean the defect site and a periosteal flap from the tibia is sutured over the defect before injecting the cells into the site [31]. While this treatment does provide pain relief to the patient [31] and the repair tissue has been shown to degrade at a slower rate than joints treated with mosaioplasty [34], successful candidates for ACI are typically young, athletic patients with little to no history of joint damage [33]. Additionally, the periosteal flap used to cover the cell suspension has been reported to cause complications during surgery due in part to its osteogenic nature and because its extraction increases surgery time and can induce donor site morbidity [35]. This has led to the use of porcine derived collagen type I/III membranes (collagen membrane ACI, CACI) as alternatives to the periosteum and other biodegradable scaffolds to seed chondrocytes into prior to implantation (matrix-induced ACI, MACI). CACI outcomes have been reported to be comparable to classical ACI, albeit with few incidences of hypertrophy, and MACI's lack of reliance on host tissue material and sutures improves procedure timing [35]. Osteochondral transfer surgeries are procedures used to treat larger, deeper defects [31]. Autologous grafts are harvested by removing plugs of osteochondral tissue from the patient's non-load bearing cartilage tissue and transplanted into full-thickness defect. Allogenic grafts from cadavers has also been used, but with varying degrees of success [31].

The limited sustainability of present treatment options incentivizes the exploration of other, more robust treatment options. For this reason, researchers have investigated the potential of generating cartilaginous tissue *in vitro* for eventual implantation via the field of tissue engineering.

2.4 Current Approaches for Tissue Engineering

Tissue engineering aims to repair, maintain, or enhance native, host tissue [4, 5]. These goals are accomplished through the *in vitro* culture of cells, supported by the application of appropriate growth factors, scaffolds, and bioreactor systems to generate a tissue structure for the eventual implantation into patients. To date, several groups have shown promising results in developing various tissue structures, such as bone [6, 7] and cartilage [6, 8]. In the case of cartilage engineering, literature has shown that it is possible to generate the tissue from a variety of modalities—from deposition printers [9, 10] to micro-scale bioreactors [11] and stackable cell sheets [12, 13].

Development of a repair construct can be accomplished either with or without the aid of scaffolds. Strategies utilizing scaffolds offer a support structure for cells to adhere and assemble tissue upon. The cells are either encapsulated into the scaffold or seeded onto the surface and eventually penetrate throughout the structure. The scaffolds themselves can be developed from a multitude of materials, from natural and synthetic polymers [36, 37] to ceramics [38, 39]. Additionally, these scaffolds can be manufactured as composite or biphasic compounds [2, 6, 40, 41] for the purposes of developing tissue with multiple cell types. In contrast, scaffold-free modalities, require the cells to develop their own structure and matrix during development [42]. While this also occurs in biomaterial-based strategies, the existing material, ideally, needs to be degraded in order to provide space for the extracellular matrix. As a result, there is an increased possibility that the scaffold-based construct will be mechanically compromised upon implantation, illicit an immunogenic response due to the consequence of material choice or differ biologically to scaffold-free constructs. Scaffold-free engineering approaches are also compromised by the lack of structural support for the cells, low throughput/long production times, and technical challenges in defining the tissue structure [42–46]. A general list of the currently applied scaffolding and scaffold-free approaches are summarized in Table 2.1 and Table 2.2, respectively.

Tissue Engineering Approaches		Description	Pros	Cons
Bioprinting [9, 47, 48]	*InkJet* [48]	Non-contact printing technique which patterns ink droplets onto a substrate to generate tissue. Droplets of "bio-ink" are generated from the printer head using thermal, electromagnetic, and piezoelectric approaches	—Robust fabrication of complex structures. —Thermal printer heads are easily modifiable for biological application and maintain a high degree of cell viability. —Bioink is generally water-based and cell density is more easily quantifiable.	—Injection volumes dependent on numerous factors for thermal systems, including nozzle size and heating of the printer head. —Cell density must be kept low enough to prevent nozzle clogging.
	Laser/Light−Based [10, 48]	Utilization of lasers to heat a surface and deposit cells onto a surface for 2D or 3D patterns.	—Suitable for top-down and bottom-up printing.	Precision and versatility varies with set up and printing concept.
Hydrogels/Scaffolds [49–51]	*Natural* [52]	Scaffolds provide a three-dimensional (3D) structure for developing tissue. Proteins and polysaccharides naturally developed in organisms, such as silk, type I collagen, and alginate.	—Biocompatible —Collagen, hyaluronan, and fibrin reported to promote chondrogenesis of both chondrocytes and stem cells.	—Some polymers can induce an adverse biological response. —Mechanical properties are not as easily tunable.
	Synthetic [52]	Artificially generated scaffolds consisting of polymers containing varying structure and densities based on fabrication technique.	—Easily manipulative mechanical properties. —PEG scaffolds enhance stem cell differentiation to chondrocytes.	—Limited biocompatibility. —Tend to require grafting of certain peptides to promote cell adhesion.

Table 2.1: List of scaffolding approaches known to have been used for cartilage tissue engineering, detailing the benefits and limitations of each strategy.

Tissue Engineering Approaches	Description	Pros	Cons	References
Scaffold-Free	Promote development of tissue structure and function to better integrate with native tissue.	Immunogenic response minimized	Reliance on cells and environment to provide structure	[44, 45, 52, 53]
Cell Sheets	Generation of monolayer sheets that can be stacked or rolled in order to form the desired tissue. These sheets are created by growing cells to confluency on a thermo-responsive polymer.	—Sheets can be stacked or rolled to form 3D structure. —With other technologies, can generate sheets containing multiple cell types.	—Durability of sheet dependent on cell adhesion. — More complex sheets require intermediate steps to better localize cells.	[12, 13, 48, 54, 55]
Microfluidic	Employ lithographic procedures commonly used in the electronics industry. Applications range from micro-contact printing to tissue generation in microfluidic channels.	—Formation of small tissue structures can be useful for high throughput analysis of disease or function.	—Developed tissue may not be suitable for implantation due to scale.	[47, 56–58]

Table 2.2: List of scaffold-free and microfluidic approaches known to have been used for cartilage tissue engineering, detailing the benefits and limitations of each strategy.

2.4.1 Biomicrofluidics for Tissue Development

To compliment scaffold-based methodologies, bioprinting technologies, such as laser-based and ink-jet [8, 59] provide the ability to generate 3D structures more representative to the native tissue. Lastly, microfluidic devices have been applied to understanding biological phenomena over the years and several groups have explored the use of BioMEMS to generate tissues within these microfluidic devices [5, 60].

The development of precise structures is desired in tissue engineering as to better mimic the complex architectures and vascular networks found in native tissue. Present techniques, such as electrospinning and solvent casting, permit the assembly of microstuctures. Unfortunately, the porosity and size within micro-scaffolds by these techniques are process-driven and can be difficult to reproducibly control [61]. The advent of micro-fabrication modalities, such as photolithography and micro-moulding, allow for the development of biomimetic structures to improve and direct cell

behaviour. A recent review discusses micro-scale assembly of structures for tissue engineering [62], so this review will briefly summarize specific findings to create both functional and biomimetic tissue structures.

A limiting factor in fabricating large scale tissue and organ structures is replication of the native tissue micro-architecture, such as the lack of an integrated micro-vasculature to provide necessary nutrients to the composing cells. To this end, researchers have attempted to fabricate micro-capillary networks within microdevices for clinical use. Literature has shown that it is possible to generate functional vascular tissue by introducing human umbilical vascular endothelial cells (HUVECs) into microchannels generated within hydrogels. The channels are generated by either polymerizing hydrogels around sacrificial networks [63] or micromoulds [64]. These modalities to generate functional vasculature can allow for the further study and development of models for disease and tissue generation, but may provide limited functionality for improving organ engineering.

To develop a more biomimetic vascular network *in vitro*, Chan *et al.* has shown that it is possible to introduce HUVECs into channels, where they were encouraged to sprout and generate micro-capillary networks following two weeks of culture [65]. Chan *et al.* and more recent work by the group state that the developed vascular beds mimic native vascular architecture and is capable of remodelling based on the hydrogel composition [65, 66]. While it has been shown that this methodology can behave like native vasculature, the group has repeatedly reported that finding an appropriate maturation time to ensure that functional tissue for clinical purposes is still elusive [65, 66].

It should be appreciated that development of a physiologically relevant tissue structure would require a complex strategy, combining multiple biofabrication and culture methods. The fluid mechanics within a microfluidic system, for example, may not stay constant as the system scales up from a micrometre scale to millimetre or higher scales. Thus, it may not be entirely possible to develop larger tissue constructs using only a fluidic approach. To address this issue, micro-bioreactors have been utilized in an attempt to express specific chemical and physical phenomena (e.g. chemical gradients and mechanical stimulation) on a smaller scale. One such methodology is the application of ultrasound (US) and exploiting the biophysical interactions between the cells and acoustic energy.

2.5 Acoustic Phenomena and their Influence in Biological Systems

Existing research has shed some insight into the biological effects of acoustic energy interaction with cells and tissue and the application of phenomena like sonoporation and acoustic streaming in biology [67, 68]. In addition to streaming, therapeutic ultrasound has also been reported to affect tissue in response to alterations to the radiation forces, and strain gradients [69]. This section will briefly discuss certain acoustic phenomena and their effect on cells and the cellular environment.

2.5.1 Acoustic Radiation Forces

For acoustofluidics, acoustic radiation forces are generated from the pressure gradient within the USWF and can be further defined as primary and secondary radiation forces. Primary radiation forces interact axially with suspended particles to direct them towards either the high pressure regions (pressure antinodes) or low pressure regions (pressure nodes) [70]. As particlescome into focus within a pressure region, such as the pressure node, the particles will encounter secondary radiation forces, or Bjerknes forces, which influence interparticle interactions (either particle attraction or repulsion) [71]. The aim of this section will be to provide a theoretical overview behind how radiation forces interact with particles entering the standing wave field.

The theory of acoustic radiation force generation, its correlation to scattering theory, and the full theoretical derivations are described in detail by Bruus [72]. To summarize, for an standing acoustic wave interacting with a particle in an inviscid, compressible fluid, the particle will scatter the incoming acoustic energy. The acoustic energy on the particle, with a radius a at some height z, is then defined as the interaction between the incoming and scattering wave. The following equations use subscript p to denote the particle density/compressibility/etc and subscript f to denote the corresponding properties of the fluid.

$$U^{rad} = \left[\frac{f_1}{3}\cos(kz) - \frac{f_2}{2}\sin(kz)\right] \times \pi\beta_f a^3 {p_{ac}}^2 \tag{2.1}$$

$$f_1 = 1 - \frac{\beta_p}{\beta_f} \tag{2.2a}$$

$$f_2 = \frac{2(\tilde{\rho} - 1)}{2\tilde{\rho} - 1} \tag{2.2b}$$

$$\tilde{\rho} = \frac{\rho_p}{\rho_f} \tag{2.2c}$$

Where f_1 refers to monopole scattering coefficient due to the presence of a particle and f_2 is the dipole coefficient related to the translational motion of the particle. The acoustic pressure is p_{ac}, wave number $k = 2\frac{\pi}{\lambda}$, where λ is the wavelength and β is compressibility, which is related to the speed of sound by $\beta = \frac{1}{\rho c^2}$. The dipole coefficient is determined through the density ratio between the fluid and particle.

The radiation forces applied onto a particle in an inviscid fluid is given as the gradient of an acoustic potential energy (U^{rad}) at some position z.

$$F_{rad} = - \bigtriangledown U^{rad} = -\frac{\partial}{\partial z} U^{rad} \tag{2.3}$$

The radiation force is then found by differentiating the acoustic energy potential:

$$F_{rad} = 4\pi k E_{ac} a^3 \Phi(\beta, \rho) \sin(2kx) \tag{2.4}$$

$$E_{ac} = \frac{{p_{ac}}^2}{4\rho_f c^2} \tag{2.5}$$

$$\Phi(\beta, \rho) = \frac{\rho_p + \frac{2}{3}(\rho_p - \rho_f)}{2\rho_p + \rho_f} - \frac{\beta_p}{3\beta_f} \tag{2.6}$$

E_{ac} refers to the acoustic energy density and $\Phi(\beta, \rho)$ is the acoustic contrast factor. The relationship between the particle's compressibility and density relative to that of the fluid (Equation 2.6) will affect how the acoustic radiation forces act on the particles and whether they will drive the particles towards a minimal potential zone (pressure nodes) or high potential zones (pressure antinodes) [21, 73–75]. Particles directed to either the pressure node or antinode will further encounter lateral energy variations and inter-particle forces, namely Bjerknes forces (F_B), which increase as inter-particle distance decreases (d, centre-to-centre) promoting clustering. The Bjerknes force on

particles (of similar radius a) at the pressure node, where the field has a velocity of v have been described by Weiser *et al.* and Crum [71, 76] can be written as:

$$F_B = -2\pi a^6 \rho_f v^2 \left(\frac{(\rho_p - \rho_f)^2}{3\rho_f d^4} \right) \tag{2.7}$$

In the context of cells, which are denser and less compressible than the surrounding fluid (culture medium), they tend to travel towards the pressure nodes [75]. The cells then aggregate within minutes [18, 77] to form sheets at the nodes and eventually interact with sheets from other nodes [73]. The formation of these aggregates is due to lateral acoustic energy variations at the nodes and inter-particle forces (Bjerknes forces, F_B) pulling cells and other particles to a nucleation cluster [70, 78, 79], which are then able to pull more cells in close proximity in order to increase the size of the aggregate. Furthermore, these aggregates also reduce interstitial voids over time as the cells form tighter junctions.

2.5.2 Acoustic Streaming

As the acoustic wave oscillates through a fluid, the energy from the pressure wave is attenuated, resulting in a displacement of the fluid molecules within the wave field space. This localized fluid displacement results in a change to the fluid flow and is a phenomenon referred to as acoustic streaming [80]. Streaming can be classified by how the particles move in relation to the surrounding space and boundaries, in which the commonly discussed forms are boundary streaming and Eckart streaming. These streaming forces occur normal to the transducer face; however, recently literature has observed the presence of streaming forces parallel to the transducer and discussed in more detail by Lei *et. al* [81].

Eckart streaming occurs as a result of acoustic energy absorption within the bulk of the fluid, resulting in attenuation of the acoustic pressure amplitude with distance from the transducer. This results in a fluid jet within the acoustic beam in the direction of the wave [80, 82]. It should be noted that for Eckart streaming to be significantly observed, the fluid chamber length must match or be greater than the

acoustic attenuation length (e.g. 8.2 mm in water at 50 MHz) and is inversely proportional to the square of the driving frequency [83].

Boundary streaming is generated through the dissipation of acoustic energy on the boundary between the fluid layer and a solid layer [80]. Boundary streaming can further be categorized as inner boundary (Schlichting) and outer boundary (Rayleigh) streaming, discussed in more detail by Wiklund *et. al* [80]. Schlichting streaming refers to acoustic energy absorption into the boundary layer at the solid-fluid interface, in the case of ultrasound travelling through water, this is on the order of 1 μm [80]. Rayleigh streaming is found near the boundary layer of solid surfaces in acoustic trapping devices [67, 80] and is particularly important for half-wave systems as it places a functional minimum limit on the size of particles which can be influenced by the primary radiation forces. Work by Spengler *et. al* [84] observed the lateral motion of particles 1–25 μm in size within a half-wave system driven at 3 MHz and generating 500 kPa for the acoustic pressure amplitude. The group's results have showed that the streaming forces were overcome with particles 10 μm, or larger, resulting in aggregates [84].

Further studies showed that radiation forces dominated over streaming forces on smaller particles through a reduction in chamber size and changing the nodal configuration [85, 86]. Streaming forces can be exploited to induce particle mixing and separation [87, 88], and a specific type of acoustic streaming, micro-streaming, can result from cavitation of micro-bubbles [80, 89, 90]. To this extent, acoustic streaming can be influential in inducing local media flow around levitating cell aggregates and potentially promote better cell-biochemical/cell-biomechanical interactions [91]. It should be appreciated that the fluid stress generated by acoustic streaming velocities is generally smaller than those stresses induced by acoustic radiation or other forces, but higher flow velocities can result in membrane rupture and cell lysis [91]. Depending on the application of acoustic streaming forces considered, such as cell lysis for nucleic acid extraction or cell maintenance in levitation, appropriate control is necessary within an acoustic system to ensure the appropriate bio-effect.

2.5.3 Thermal Effects

Similarly streaming, the thermal effects of ultrasound are driven by acoustic energy

absorption by the surrounding environment, primarily discussed in the context of ultrasonic attenuation by tissue [92]. The temperature rise in the tissue environment is dependent on a number of factors, including the absorption coefficient of the tissue and the ultrasound exposure parameters and configurations [92]. To better elucidate the effects of heating hermal effects for standing waves have been modelled in relation to acoustic streaming [93, 94] and extensively researched experimentally for therapeutic US [95]. In general, heat generation would occur from electromechanical losses from the piezoelectric transducer and adhesive elements (e.g. epoxy or other coupling materials) between the transducer and rest of the system. Thermal conduction would then occur from the transducer across to the fluid to cells and tissue [91]. While cells and tissue intrinsically contain protective mechanisms, such as heat shock proteins, to tolerate higher operating temperatures, prolonged exposure to temperatures higher or lower than 37 °C±1 °C may lead to reduced cell activity, cell cycle arrest, or death [91]. Active cooling mechanisms, such as fans and Peltier circuits can be used to reduce heat transfer to the cells, but feedback loops and general maintenance is still necessary to ensure a physiologically relevant temperature is maintained to ensure optimal cell viability and activity.

2.5.4 Cavitation and Sonoporation

Cavitation describes the interaction between a gas bubble and the radiation forces within the acoustic field, resulting in oscillation of the bubble. The primary radiation forces result in the attraction or repulsion of microbubbles at the pressure node or antinode. The secondary, or Bjerknes forces refer to the interaction between bubbles [76, 96]. The radiation force interaction with the bubble will change as the bubble displacements; for example, as the secondary force attracts two bubbles, the walls of the bubbles move against each other, leading to a phase shift in the interaction force and oscillation of the bubbles [96]. This oscillation influences the secondary Bjerknes forces, where the magnitude of attraction or repulsion is dependent on the resonant length of the bubbles in relation to the radial distance between bubbles [96].

The cavitation of bubbles in an acoustic field is classified as either stable or inertial cavitation. Both types of cavitation have been shown to enhance drug delivery with functional differences in application as reviewed by Lentacker *et. al* [97]. Stable

cavitation occurs when bubbles oscillate over several acoustic cycles about their equilibrium radius and generally at low acoustic intensities [91, 98]. Stable cavitation has been applied to enhance micro-mixing and drug delivery to cells and reversible permeabilizationn of membranes, such as the blood-brain barrier [99]. Additionally, this type of cavitation can result in changes to local streaming and may further disrupt cell aggregation proximal to the air bubble [91]. Despite this, stable cavitation would inflict minimal change to the cells within an acoustic field.

In contrast, inertial cavitation refers to bubbles expanding and contracting as a result of the fluctuations in the acoustic pressure at higher intensities, eventually resulting in their collapse. Bubble oscillation as a result of inertial cavitation occurs along smaller time scales (approximately 10 µs) than stable cavitation and the violent collapse of the bubbles would result in localized high pressures and high velocity fluid jets [91]. This type of cavitation is also commonly exploited with therapeutic US. Inertial cavitation has been used to improve drug delivery into deeper tissue, enhance tissue heating and chemical transport of larger molecules into cells via sonoporation [91, 97, 100, 101].

Inertial cavitation of bubbles and their subsequent collapse would result in a localized jetting force. The utilization of this force near the cell membrane has been shown to generate transient holes into the cell, termed sonoporation [80, 97, 102]. The exact mechanism by which sonoporation occurs is still under research as it is unclear whether this occurs through micro-streaming or inertial cavitation [80]. Nevertheless, sonoporation has applications in material transport into cells, such as for gene therapy and transfection [68, 97, 103, 104].

In summary, literature has expressed a number of ways, where acoustic phenomena have been exploited to pursue a biological problem. It should be appreciated, however, that many of the mechanical and thermal forces generated by ultrasound can be both beneficial and detrimental to cells and tissue. As such, it is necessary to control and regulate the acoustic environment both in terms of the force magnitude and activity time to exploit the desired bioeffect from acoustic interactions. Given that many of the aforementioned acoustic phenomena have been discussed in the context of microfluidic systems and tissue, acoustic interaction with biological systems generally occurs within the ultrasonic spectrum.

2.6 Ultrasonic Technologies for Biomedical Applications

Ultrasound refers to sound waves with a frequency 0.02 MHz or higher [105], with a range of 3-10 MHz used in the clinical setting for imaging and therapy [106]. In the 1950s, it was realized that US could be used to visualize tissue structure when a detector picked up reflected wave patterns that were transmitted by organ boundaries. By the 1960s, US was commonly used in the clinic as a non-invasive, diagnostic imaging tool [67, 107–109]. Since then, improvements to the technology have not only provided enhanced imaging of the material from surface topology down to the molecular level [110, 111], but also the ability to quantify the material properties of tissues and the state of tissue degeneration [111–114]. Another imaging modality brought on by US is elasticity imaging, or elastography, which allows for visualization and quantification of the material properties of soft tissue [115] via strain and shear wave imaging.

For tissue generation, US has predominantly been used in two ways:

1. Low-intensity ultrasound (LIUS) to stimulate cells.
2. Ultrasonic standing wave fields (USWFs) to generate acoustic traps for spatial manipulation of cells and proteins.

2.7 Therapeutic Ultrasound

Therapeutic US has been widely used to repair tissue over the decades, whereas USWF use for tissue development is emerging. Despite this, cell and tissue-level interaction with these technologies is still ongoing. This section will discuss how acoustic forces can interact with the physical environment as well as explaining the theory behind therapeutic US and USWFs and their application to regenerate vasculature, bone, cartilage and nerves. These areas have received considerable research interest and wide methodologies to apply US both *in vivo* and *in vitro*. This section will also discuss some of the physical theory behind US function as well as the mechanotransductive effects US has on stimulating cell growth and differentiation. In the case of bone and cartilage regeneration, this has been reported to occur through integrin signalling to the focal adhesion kinase (FAK), extracellular signal-regulated kinase (ERK), and

phosphoinositide 3-kinase (PI3K) pathways, in addition to numerous other pathways [116]. These mechanisms will be discussed in more detail in the relevant sections, but it should be noted that US promotes cell activity through a variety of signalling pathways and work is still required to fully understand how US induces differentiation of various cell types.

Therapeutic US has seen use by clinicians for its thermal and non-thermal effects to the physical environment surrounding cells [89, 108]. The two methods of therapeutic US application are high intensity US and LIUS. The distinguishing characteristic between these two modalities is that LIUS refers to acoustic stimulation of tissue to promote repair, whereas high-intensity US results in high energy absorption by tissue to induce heating [105, 117]. Commonly, high intensity US is also focused to apply acoustic stimulation to a small site as high intensity focused US (HIFU). This modality has been reported to readily "'micro-machine"' tissue through tearing or cutting of the tissue using inertial cavitation, localized heating, and streaming of fluids [117]. While LIUS has been reported to also result in temperature changes, these changes are minor in comparison to HIFU exposure. As a result, the physical effects LIUS exposure on tissue are predominantly non-thermal [69]. The non-thermal effects of LIUS are discussed in detail by Padilla *et al.* on the tissue level down to the molecular level, but it is speculated that LIUS generates oscillating strain tensors to apply cyclical loads onto the cell membranes as a means of mechanostimulation [69]. To translate the mechanical forces to cell signals, multiple mechanosensitive factors have been identified including integrins, ion channels, and intermediate filaments [118–122].

LIUS stimulation of tissue is typically accomplished through the use of either an unfocused transducer or array to generate a focused US beam. The acoustic energy output from the transducer is reported as the spatially and temporally averaged intensity (I_{SATA}). It should be noted that this is an indirect measure of the ultrasonic intensity and realistically less than the spatial and temporal averaged acoustic intensity [123]. As mentioned before, the distinction between LIUS and HIFU is how much acoustic energy interacts with tissue. To this end, LIUS treatments apply US in an intensity range from 0.125 Wcm^{-2} to 3 Wcm^{-2}, while HIUS treatments apply at least 5 Wcm^{-2} [124]. The effects of LIUS stimulation of tissue have been investigated with daily exposure times ranging from 1µs–20 minutes [69, 125]. The modalities of LIUS exposure commonly used are either pulsed bursts of LIUS (LIPUS) or continuous

stimulation over the exposure period. This wide variation in parameters is partly the result of cells from different tissue types reacting differently to the applied pressures, but also to induce certain phenomena in the local environment, which will be discussed later. Ultrasonic stimulation of tissue is complex and previous literature has shown a variety of bio-effects based on tissue/cell interaction with acoustic waves. The lack of a standardized set of experimental parameters (e.g. exposure duration, exposure intensity, frequency) has led to conflicting results both *in vivo* and *in vitro*, ultimately limits the interpretation of results [69, 126]. To this end, recent literature has stressed the importance of reporting US exposure settings and the boundary geometry of experimental rigs [69, 127].

2.7.1 Implementation of Therapeutic Ultrasound for Tissue Repair

2.7.1.1 Neural Tissue Regeneration and Mechanotransduction

Attempts to stimulate neural repair have been explored using low-intensity focused US (LIFUS) or LIUS [128–130]. There is evidence that LIFUS can be used to influence neuromodulation in the nervous tissue, thereby stimulating repair [129, 130]. The exact mechanism by which this occurs is unclear. However, one possible theory is that neuromodulation as a result of LIUS occurs as the sodium and calcium channels are physically stretched as a result of mechanical forces [121, 125]. Specifically, it was found that short pulses (as low as 0.5 msec [125, 131]) increased the amplitude and frequency of action potentials [125] and long pulses of LIUS inhibited depolarization. Additionally, as longer pulses can keep the gates in an activated state for a prolonged period of time, this can inhibit the generation of more action potentials until the membrane is brought back to its resting potential (refractory period). Tsui *et al.* [121] also noted that conduction speed eventually plateaued and decreased with longer pulsing. A side effect of longer pulses is the heat propagation, so it is possible that depolarization of the neurons is inhibited as a result of heating and deactivation of the ion channels, thereby preventing their function [121]. US manipulation of action potentials has proven to be therapeutic for a variety of central nervous system disorders, including epilepsy and Parkinson's disease [125].

For the peripheral nervous system, work was undertaken to investigate the effects of LIUS to direct neural differentiation and proliferation as a potential treatment for injury [128, 129, 132]. While the biological mechanisms behind this process are still unknown, the authors [129] also showed that US stimulation of injured rat sciatic nerve fibres induced axonal extension, relative to natural nervous repair by the body within 4 weeks post-trauma. Specifically, the study illustrated that LIUS exposure around the defect site resulted in the production of neural growth factor (NGF), which would promote neural proliferation and further axonal regeneration. Furthermore, histological assessment of the myelin sheaths for both the US and control groups indicated that the US-treated samples exhibited more regenerated myelin. This is important as myelin sheath repair facilitates axonal growth, thereby accelerating nerve regeneration [129]. Finally, the group also noted that growth slowed down as the fibres extended past the defect site and further away from the treatment point. Given these observations, it could be implied that US treatment might have reduced the inhibitory nature of the immediate repair environment, thereby allowing regeneration of the nerve through production of NGF. It remains to be demonstrated if this effect is the result of certain factors physically being moved by the ultrasound or if the acoustic energy might have damaged or denatured the inflammatory proteins in the area. Park *et al.* [132] had noted success in repairing damaged nerves via nerve guidance channels supplemented with LIPUS. The group suggested the improved repair might have been attributed to the guidance channel filtering inhibitory factors from the environment while US promoted Schwann cell propagation, thereby assisting in nerve repair. These findings combined with Chen *et al.* [129] suggest that nerve exposure to LIUS promotes regeneration of Schwann cells in conjunction with secondary effects of mechanical transduction in the environment.

2.7.2 Skeletal Tissue Regeneration and Mechanotransduction

2.7.2.1 Bone Remodelling

Utilization of LIUS for fracture and non-union healing has been well established [7, 133] and forms the basis for much of the expansion of US therapy into other tissue types [129]. The type of US stimulation for bone repair is typically LIPUS and the majority of treatment involves an acoustic intensity of 30 mW/cm^2 (I_{SATA}) for 20

minutes a day with a pulse repetition frequency of 1 kHz (200 µs of acoustic exposure, 800 µs off) [69].

LIPUS has been shown to promote expression of osteogenic genes, such as runt-related transcription factor 2 (*Runx2*), osteopontin (*Opn*), and osteocalcin (*Ocn*) [134, 135]. The mechanism behind the application of LIPUS for fracture repair is still under investigation and the potential to augment endochondral ossification remains the focus of study [136, 137]. Previous work has indicated that US exposure can mechanically stimulate chondrocytes to undergo hypertrophy and produce aggrecan and other matrix proteins [137]. Chondrocyte hypertrophy is important in the temporal process of endochondral ossification and Tang *et al.* demonstrated that LIPUS stimulation of osteocytes promoted cyclooxygenase 2 (COX-2) expression following a 20 minute treatment [120]. This increase in gene expression was found to be directly related to enhanced mineralization of tissue; however, the mechanotransduction pathway leading to COX-2 up-regulation has not been fully elucidated [116]. Other studies suggest LIUS can enhance repair in both long [116] and flat bones [134] indicating not only promotion of endochondral, but also intramembranous ossification. It has also been shown that LIPUS stimulation of osteoblasts promotes activation of either the ERK/mitogen-activated protein kinase (MAPK) or PI3K/Protein kinase B (Akt) pathways to promote osteogenesis [69, 120, 138]. This further indicates the role of US in promoting differentiation of cells and mineralization of the matrix, rather than proliferation [134, 135].

One of the main reasons why the mechanisms by which LIPUS promotes bone regeneration are still unclear is due to a lack of standardization within the field (summarized by [69]). In particular, experimental rigs may show the application of US in ways that may not take potential acoustic phenomena into account; such as streaming, standing wave production, and variations in the spatial acoustic intensity [69, 139]. Fung *et al.* [139] recently described the effect of near field versus far field LIPUS stimulation of bone tissue using a 2.2 cm diameter transducer driven at 1.5 MHz. The group noted that acoustic intensity extrema were prevalent in the near field (0–30 mm from transducer) with less destructive interference and wave complexity in the mid and far-field (60 mm and 120 mm away from transducer) [139]. It was shown that while the LIPUS treatment enhanced callus formation over the sham model, far-field stimulation of the tissue expressed augmented mineralization and bone volume

formation relative to the near-field. Additionally, it was found that mid-field stimulation of the fracture site enhanced chondrocyte hypertrophy and endochondral ossification, ultimately creating woven bone at a faster rate relative to the sham model [139]. This difference has been noted to be a result of the presence of extrema at the near-field, which may result in lower and less consistent energy densities interacting with the cells [139, 140]. Furthermore, this report indicates the necessity of careful analysis of the acoustic forces applied onto the tissue and potential bio-effects.

Fracture healing involves recruitment and differentiation of both osteoblasts as well as mesenchymal stem cells (MSCs) to the repair site. It has been suggested that LIUS promotes MSC recruitment via the Stromal cell-derived factor 1/C-X-C chemokine receptor type 4 (SDF-1/CXCR4) signalling pathway, which mediates MSC migration to an injury site [141]. Recently, Kusuyama *et al.* have shown that LIPUS stimulates MSC and progenitor cell differentiation down the osteogenic lineage [142]. Specifically, it was shown that LIPUS stimulation limited transcription of genes related to adipogenesis, such as fatty acid binding protein 4 (FABP4) and peroxisome proliferator-activated receptor gamma 2 (PPARγ2) even in the presence of induction medium. RUNX2 and osteocalcin, genes for osteogenesis, were reported to be enhanced by LIPUS stimulation [142]. It should be appreciated that this gene expression change was observed in a mouse MSC cell line (ST2) and mouse preosteoblast line (3T3-L1). To further elucidate the method by which LIPUS stimulation enhanced osteogenesis, the group looked into the phosphorylation levels of several proteins related to cell proliferation and differentiation (e.g. ERK 1/2 and rho-associated, coiled-coil-containing protein kinase, or ROCK) and as well as cell-specific markers downstream of ERK activation, such as Cot/Tpl2. It was found that LIPUS promoted activation of ROCK1 and correlate its activation to ERK phosphorylation and activation of Cot/Tpl2 [142].

2.7.2.2 Cartilage Development

LIUS have been used to direct cells into a chondrogenic lineage and promote cartilaginous matrix deposition to generate cartilage *in vivo* and *in vitro* [77, 89, 106, 109, 143–147]. Utilization of LIUS for cartilage tissue formation has yielded conflicting results for cell proliferation and matrix development as a result of

differing culture conditions (cell source, 2D vs 3D, etc.) [106, 146, 147]. A consistent detail about this methodology, however, is that LIUS promotes expression of SRY (sex determining region Y)-box 9 (Sox9), collagen type II, and other chondrogenic markers [77, 89, 143, 145, 146], which results in the formation of tissue that is comparable, if not marginally better, than producing cartilage via pellet culture [143, 147]. It should also be noted that cultures supplemented with transforming growth factor beta (TGF-β) and LIUS displayed more robust hyaline structure and stronger staining for cartilage matrix proteins (e.g. aggrecan) [143, 146]. With regard to *in vivo* studies of cartilage formation, it was reported that LIUS stimulation of cartilage explants promoted deposition of cartilage matrix proteins, such as aggrecan and type II collagen, but chondrocyte proliferation in 3D cultures and explants was unaffected [109]. Further to this, a recent study in humans showed that moderately and mildly afflicted osteoarthritic patients who have undergone LIUS treatment received minimal change in their tissue [88]. Scaffolds seeded with mesenchymal stem cells (MSCs) that have undergone LIUS stimulation to generate cartilage tissue have shown comparatively better integration and quality compared to TGF-β [144] and hyaluronic acid stimulated samples [148].

2.7.2.3 Investigation of Mechanical Role of Therapeutic Ultrasound in Bone and Cartilage Remodelling

A variation of LIUS stimulation for *in vitro* study involves a transducer transmitting acoustic waves throughout a chamber [122, 145, 149], referred to as low-intensity diffuse US (LIDUS) [150]. Functionally, this modality is similar to conventional LIUS, but designed to have the acoustic waves radiated throughout the sample chamber. This diffusive stimulation pattern has been shown to alter the morphology on chondrocytes in 2D monolayer as well as 3D culture to better assume a mesenchymal structure [122, 147, 149, 151]. In both cases, it was found that the mechanical effects of the US pulses affected the cell morphology and assisted in the chondrocytes better assuming a mesenchymal morphology onto the substrate. Due to the random stimulation pattern of the acoustic waves, however, it cannot be definitely stated whether this change in morphology was the result of the diffuse interference pattern or US exposure as a whole. Recent literature has shown that LIUS stimulates chondrocytes to proliferate and differentiate through the ERK/MAPK and PI3K/Akt

pathways [119, 147]. It has been reported that LIPUS stimulation of cells induces a frequency dependent expression of early response genes, c-Myc, c-Jun, and c-Fos, with the highest expression at 5 MHz compared to 2 MHz and 8 MHz [147]. Continuous, rather than pulsed, application of LIUS has also been reported to express higher phosphorylation of proteins associated with the ERK/MAPK pathway [152].

While the ERK/MAPK pathway is considered to be a general signalling pathway to promote cell proliferation, Takeuchi *et al.* have reported on the possibility of LIUS stimulating chondrocytes through the integrin/PI3K/Akt pathway [119]. This signalling pathway plays a role in chondrocyte growth, differentiation, and matrix remodelling. Recently, Cheng *et al.* [118] further investigated this pathway's role in cartilage repair and observed that LIPUS-stimulated rabbit chondrocytes expressed higher phosphorylation levels of FAK, PI3K and other proteins involved with the PI3K/Akt pathway relative to their normal and osteoarthritic (OA) control groups. Furthermore, higher levels of collagen type-II and aggrecan were observed in LIPUS-stimulated cells, relative to the control OA chondrocytes, while matrix metalloproteinase (i.e. MMP-1 and MMP-13) expression was reduced [118]. This would suggest that LIPUS activation of the integrin/PI3k/Akt pathway promotes chondrogenesis and rescue matrix degeneration in OA samples. The present work on elucidating the mechanotransductive effect of LIUS on chondrocytes is promising and shows that the interaction is not through a single signalling pathway, but rather the interaction is multifaceted and the mechanical forces affect the cells through intermediate filaments and multiple transcription pathways [116].

2.8 Bioacoustofluidics

Acoustic manipulation of cells is advantageous due to its biocompatibility and label-free nature [153]. For example, acoustofluidics utilize acoustic pressure waves in a fluidic system to manipulate cells. This has been used in microfluidics as surface acoustic wave fields (SAWs) [154–157] or bulk acoustic wave fields (BAWs) [158–161]. While cell patterning onto substrates is possible with acoustofluidics, either through the use of single or multiple planar transducers organized in an array [162–164], SAW-based patterning has also been shown to generate a variety of patterns (1D and 2D) in both flowing and stagnant fluids [155, 157]. Literature has further expressed

integration of acoustic elements into other modalities, such as 3D printers [165] and force spectrometers [166] to improve the overall performance of the system to generate the desired output, while maintaining a level of simplicity in the design.

2.8.1 Ultrasonic Standing Wave Fields

2.8.1.1 Surface Acoustic Waves

The application of surface acoustic waves (SAWs) for acoustofluidics is recent, relative to bulk acoustic waves (BAWs) [155], however, the methodology allows for greater precision and versatility when utilizing higher excitation frequencies to generate a trap (10–1,000 MHz) [167]. Additionally, SAWs do not rely on chambers consisting of acoustically resonant materials—allowing the use of common microfluidic materials, such as poly(dimethylsiloxane) (PDMS), which is acoustically dampened—and potentially easier integration on-chip to existing fluidic components [155]. Typically, a SAW device consists of at least one interdigitated transducer (IDT). IDTs comprise of interweaving metallic strips extending from electrode rails directly deposited onto a piezoelectric surface. As a signal is driven to the transducer, an electrical field is established, which is translated to the surface to propagate mechanical stress.

A variety of methods exist to generate SAWs and theory for which is covered extensively by Gedge and Hill [168], with Yeo and Friend recently covering their biological use [167]. This review will therefore summarize surface acoustic wave field generation and their biological application in the context of bioacoustofluidics. A single IDT generates a travelling wave, commonly a Rayleigh wave for microfluidic applications [155]. The characteristics of the generated wave can be altered by manipulating the physical properties of the IDT, specifically through modulation of the number of metallic strips, their interstitial spacing, or overlapping length [155]. Alterations to the IDT's physical dimensions or structure can result in the formation of waves varying spatially (e.g. focused IDTs) or by operating frequency, in the case of chirped or slanted finger IDTs. Additionally, the pairing of identical IDTs allows the formation of standing waves. This pairing allows for the formation of one and two dimensional wave fields, permitting the study of more complex biological solutions and patterning.

2.8.1.1.1 SAW-based Acoustic Separation and Patterning

The manipulation of cells with SAW devices is still in the initial phases, but allows for fine patterning of individual cells and sets of cells to facilitate understanding of localized interactions in 3D space [169]. In addition to patterning, cell enrichment using SAW-based devices has garnered interest. It has been reported that standing SAWs can be used to focus particles in flow and Chen *et al.* recently furthered this concept to better concentration cell samples during continuous flow [170]. The group designed a chip with two parallel IDTs positioned perpendicular to the microchannel, thereby generating a one-dimensional wave field also perpendicular to the flow. Activation of the trap allowed enrichment and saturation of the nodes within 10 minutes at 7 µL/min and a recovery efficiency of 93% (10^5 cells/mL concentration) [170].

Similarly to SAW-based enrichment methods, cell separation devices also utilize standing wave fields generated by parallel transducers. Through this method, pressure nodes form parallel to the flow, but limited by low separation efficiency and sensitivity (i.e. little to no separation between particles of similar sizes). To this end, recent literature has attempted to improve acoustic separation by altering node placement relative to the flow. Ding *et al.*, for example, attempted improved size separation by positioning two parallel transducers at a 30°angle (θ) to a microchannel [153]. Sheath flow focused the particles towards the centre of the channel and the acoustic radiation forces direct larger particles (10 µm beads) while smaller particles (2 µm beads) experience little movement. Fractionation within their system was optimized at a tilt angle of θ=15 deg and an operating power of 45 dBm (25 dBm equates to 2 W/cm^2) and further tuning of the recovery/purity fraction of cells could be tuned by adjusting the fluid flow towards or away from the collection duct [153]. The present application of SAW-based technologies for cell manipulation is promising and further iterations potentially expanding biological applications.

The application of surface acoustic waves is not limited to cell capture and filtration, but can be utilized to further cell penetration into a porous scaffold [154]. Bok *et al.* reported that SAW-based streaming translated forces into the scaffold pores, causing capillary bursting and an overall pressure drop within the scaffold. This pressure gradient was reported to promote cell penetration into the scaffold without adversely affecting the cell viability [154]. Additionally, Ahmed *et al.* reported on the exploitation of microbubbles within a SAW device to induce a rotation on single cells

and whole organisms (C. *elegans*) [171]. The relevance of this approach is that present literature has expressed the potential of using rotational behaviour as an indicator of cell morphology for diagnostics [172].

2.8.1.2 Bulk Acoustic Waves

There are a variety of methods to generate an acoustic field within a fluidic system, as reviewed by Lenshof *et al.* [159] and in a comprehensive review by Friend and Yeo [173]. For this review, USWFs will be discussed in the context of layered resonators [158]. In this type of system, acoustic waves are transmitted from the transducer at its resonance frequency where the pressure waves are transmitted through the carrier layer (i.e. the channel wall adjacent to the transducer) and reflected off of the reflector layer, or opposite wall. This reflected wave is in phase with the transmitted wave, creating a standing wave field within the fluid layer. The standing wave field generates a pressure gradient where acoustic radiation forces trap particles within the fluid layer.

It should also be appreciated that the number of nodes and their positions can be configured by manipulating the thickness or material of the different layers and the frequency of the US wave relative to the system's acoustic resonance [158]. The alterations to the layers can change the driving frequency and voltage applied to create the trap, therefore, care is needed to ensure that physical changes to the system do not greatly alter the trap configuration. Additionally, the positioning of pressure nodes can not only be altered vertically, but also laterally through the use of transducer arrays [163, 174]. Lateral manipulation of particles was accomplished by specifically activating individual elements within the transducer array in order to re-localize aggregates or to generate multiple focus points within a pressure node [174].

The most used configurations are referred to as: half wave, quarter wave, and thin reflector [158]. Half wave devices refer to when the fluid layer thickness is equal to half the wavelength of sound through the fluid, which results in the presence of a pressure node within the fluid layer, away from the channel walls. Quarter wave devices bring particles towards the reflector layer [158]. The quarter wave configuration is sensitive to changes in the thickness of the system's reflector layer due to balancing the total resonance tuning throughout the device and the resonance of the fluid layer [158]. Lateral variation in the system can also vary the node's location between the fluid

layer and reflector, thereby leading to non-uniform localization of particles onto the surface. A thin reflector configuration is considered to be an alternative to quarter wave systems in that it also brings particles towards the reflector/fluid interface [158]; however, in contrast to the quarter wave configuration, the thin reflector configuration is rather insensitive to the layer thickness. The main caveat with this configuration is that the reflector, fluid and carrier layers are all thin compared to the wavelength (e.g. 0.1λ) [158]. These configurations can all serve different biological and non-biological applications [78, 158, 175] and further show the versatility of acoustic traps.

It is widely accepted that USWFs can selectively manipulate cells and proteins within the wave field [19–21, 67, 73, 158, 176]. Furthermore, when compared to other trapping methods, such as optical and dielectrophoresis, ultrasonic trapping is a relatively inexpensive technique [18]. Acoustic traps typically do not require any modification of the cells or fluid medium, in contrast to dielectrophoretic traps, which require the cells to have a different conductivity from the medium [75, 177]. USWF traps are also capable of trapping individual to tens of thousands of cells [18, 74, 75, 176]; which allows for more scalable development of tissue. Edwards *et al.* [77] noted that while the cell aggregates are levitating in space, assuming a spheroidal morphology, the actin fibres near the membrane orient themselves similarly to confluent cells in 2-D monolayer cultures. This patterning feature is important as it provides some insight into intracellular interactions in 3D aggregates, which could be useful in creating and understanding tissues, such as epithelial linings. Additionally, this interaction can also suggest a type of minimum structure which could be useful when creating more complex patterns of cells [23].

2.8.2 Biophysical Investigation

Atomic force microscopy (AFM) has proven to be a valuable resource in quantifying biophysical interactions. Unfortunately, AFM and other methodologies that permit investigation of single molecule interactions are generally complex, limiting their general use outside of specialized labs, and low throughput [166]. To address these limitations, single molecule imaging techniques have focused on smaller scale, microfluidic systems, using mechanical forces such as centrifugal forces [178] to assess molecular interactions. More recently, Sitters *et al.* [166] integrated an acoustofluidic

method to an existing flow cell to manipulate DNA-tethered microparticles to study the intermolecular tension within DNA. Due to the planar nature of acoustic trapping within the bulk space, the group was able to perform high-throughput imaging of polystyrene beads as they were pushed towards the pressure node. The time-dependent force on the particles as a result of the acoustic force and DNA strand tension was determined using image analysis [166]. The group noted that their acoustic force spectroscopy system allowed for a wide range of force application on the samples and the simplified implementation into microfluidic systems, relative to other contemporary techniques, would allow for more widespread application in non-specialized labs [166]. In addition to nano-force investigations, Mishra *et al.* has demonstrated the potential of USWFs as a means of mechanically deforming single cells [25]. The study investigated the degree of erythrocyte compression in a range of acoustic pressure amplitudes (i.e. 12.9 – 978kPa) and observed significant changes to the aspect ratio of the cells with increasing acoustic output. Overall, the study exhibited how acoustic fields can physically deform cells, potentially affecting their differentiation potential and internal mechanisms [25].

2.8.3 Probing for Biological Function

Acoustic traps have been shown to be useful in their ability to generate small-scale tissue models to understand cell-cell interactions and elucidating biological responses on a more dynamic time scale. USWFs have been used to levitate neural cells to study cell-cell and cell-environment interactions [162, 179, 180]. These studies offer valuable insight into how cells react in such close proximity to one another and how the acoustic waves may influence the individual cells and the cell aggregates as a whole. Bazou *et al.* [180] indicated that cells influenced by the USWF still remain viable and localize f-actin over time. Additionally, levitation of the cells using USWFs appears to have resulted in relatively little influence on the differentiation potential of the cells. The study reported that cell-cell junctions formed within 30 minutes of aggregation and the cells are positive for a neuron specific adhesion molecule (NCAM) [179, 180]. Furthermore, an additional study by the group has shown that pluripotent gene expression by embryonic stem cells is retained as the cells are levitated [74]. These findings suggest that levitation of cells and formation of aggregates using USWFs neither influences cell viability nor their lineage.

Literature has shown that natural killer (NK) cells, a class of lymphocytes in the vascular supply, are capable of recognizing aberrant cells and are important in the body's immune response against tumour cells. Given the complexity and response time of the body's immune system to incoming threats, many of the present techniques are limited in their ability to precisely control single cell interactions. Christakou *et al.* devised a multi-well transverse resonator system [181] to investigate the NK cell interaction and response to immortalized hymphoblastoid cells [182]. Ultrasonic levitation and aggregation of NK cells with tumour cells revealed clustering of immune-specific ligands at the interface between the two cells. This behaviour was maintained over the experimental time period with no cell death, further enforcing that cell behaviour is not dramatically affected by the acoustic forces maintaining its levitation and aggregation [182]. This system was further expanded in a more recent study, whereby a tumour cell spheroid was generated to study the NK cell response to a more 3-dimensional mass of cells [183]. The study performed a parametric analysis to observe NK cell communication and destruction of tumour aggregates at different population ratios (e.g. time to destroy tumour growths with NK cells at a population mix of 1:10 versus 1:40) [183].

In developing cartilage, mesenchymal cells in the extending limb bud would deposit extracellular matrix, condense into a tight structure, and eventually differentiate into chondrocytes. During this process, multiple transcription factors, cell adhesion proteins, and ECM components are expressed and regulated to permit normal development and maturation of the tissue [77]. To better understand how mesenchymal cells interact with one another in forming condensations, Bazou *et al.* investigated the role of gap junctions and how the cytoskeletal structure changes in the development of pre-cartilage [184]. The group found that the cytoskeleton, specifically, f-actin co-localized with gap junction proteins over time and produced a mechanically stronger (i.e. less fragmented aggregate upon removal from their device). A different study by Edwards *et al.* observed Sox9 expression in levitating chick wing bud cells compared against condensation culture and monolayer [77]. The cells were stained for Sox9 following their respective treatments and it was reported that both the condensations and aggregates expressed Sox9 in the cell nucleus, while this expression was lost in monolayer. It is important to note that the Sox9 expression was rescued with treatment of cytochalasin D (CytD), but not through levitation [77].

With regards to bulk acoustic wave-based cell separation/enrichment, recent research has focused on multi-stage channel designs to more easily separate the target phenotype from the rest of the material [185, 186]. The rational to the more complex designs is a result of the force exerted onto the cell proportional to its size, thus increasing the complexity of processing a direct sample from a patient given that many cells are relatively similar in size.

To address this limitation, Augustsson *et al.* has recently shown the potential of iso-acoustic cell focusing in an inhomogeneous fluid [187]. The principle of iso-acoustic focusing is that there exists a medium condition for which the acoustic contrast between the cell and fluid, and therefore the primary radiation force, is zero [187]. Cell separation using this principle was induced by creating a concentration gradient of iodixanol in saline (10% at the channel boundaries, 30% at the channel centre). Due to the fluid density variance within the bulk of the fluid, the group observed effective separation of individual cell types based on their characteristic compressibility and density relative to the inhomogeneous fluid. This system was further characterized by computational modelling by Karlsen *et al.*, who expressed how the acoustic energy density changes within the bulk of a inhomogeneous fluid [188]. The study suggests that acoustic streaming is suppressed within the bulk of an inhomogeneous fluid and stabilization of the fluid density gradient is accomplished through the acoustic force density.

2.8.4 Ultrasound Enhanced Tissue Engineering

In the context of tissue engineering, applied scaffolding and scaffold-free approaches are summarized in Table 2.1 and Table 2.2, respectively. To compliment scaffold-based methodologies, bioprinting technologies, such as laser-based and ink-jet [8, 59] provide the ability to generate 3D structures more representative to the native tissue. While LIUS has been deeply researched in its potential to provide mechanical stimulation to promote tissue growth and repair, acoustic trapping has primarily been applied to pattern cells along the pressure node. There is some evidence, however, that USWFs may either alter the material structure or directly have an effect on the cells themselves, as evident in the vascular networks generated by Garvin *et al.* [20]. The Dual group has recently published on both theoretical and experimental studies on the

effect of acoustic radiation forces on the disk-shaped particles [189, 190], unfortunately, present literature lacks in-depth findings on the biological response of cells (i.e. changes to the cell or cell-cell interactions) exposed to these forces within an acoustic trap.

As mentioned before, studies on USWFs for tissue generation are few. Recently, our group has been the first to show the potential to develop cartilaginous tissue through cell levitation in perfusion culture for a period of 21 days [22]. A million cells were introduced into a glass capillary and trapped in a half-wave configuration using a PZT transducer adhered to the capillary wall. The cells organized into a planar sheet in 3D space following their introduction into the trap. A range of frequencies (frequency sweep) was driven into the devices to account for changes in the resonant frequency due to heating of the transducer [22]. At a sweep repetition rate of 50 Hz, lateral translation of the cell sheet was observed and coupled with the shear forces from fluid flow to provide mechanical stimulation to the aggregate during development. Histological analysis of the generated tissue exhibited minimal expression of type I and type X collagen, negative markers for hyaline cartilage, and compressive testing of the tissue was found to be comparable to native articular cartilage. This would suggest that the generated cartilage is analogous to hyaline cartilage both mechanically and in terms of the matrix composition [22]. Additionally, implantation of the fabricated tissue onto an *ex vivo* model showed ready fusion of the tissue to the native cartilage and no alterations to the construct structure was noted. While improvements to the tissue development and understanding of the forces applied on the cells is needed, this study exhibits the potential of using acoustic trapping for scaffold-free cartilage generation.

Whereas Li *et al.* discussed the potential of acoustofluidics for scaffold-free tissue engineering, Garvin *et al.* [19–21, 73], and more recently Bouyer *et al.* [24], utilized an acoustofluidic bioreactor transmitting a pressure wave through a hydrogel solution to orient cells prior to polymerization of the hydrogel. Garvin *et al.* present this concept as a means of developing vasculature using human umbilical vein endothelial cells (HUVECs) suspended in a collagen hydrogel, while Bouyer *et al.* followed up with this concept to develop a layered neural network from neuro-progenitor cells within a fibrin gel. The primary distinction between this and the work described by Bazou *et al.* is that the studies in the latter group continuously expose cells to a USWF, whereas Garvin *et al.* exploited the acoustic trap temporarily to pattern the cells into sheets as

the hydrogel polymerized. The benefit of this approach is that the cells can be rapidly assembled in 3D space, shortening the culture duration to generate a 3D architecture mimicking the native tissue [24]. It should be appreciated, however, that the acoustic forces may affect both the cells and the hydrogel architecture during the patterning phase.

To characterize the influence USWFs imposed on the cells within a scaffold, Garvin *et al.* and Comeau *et al.* tested various operating frequencies, acoustic pressures, and temporal average intensities [20, 21, 191]. Additionally, the efficacy of this approach was compared to a sham model, where the hydrogel was allowed to polymerize in the absence of US exposure [19–21, 73]. Alterations in the acoustic frequency varied cell sheet spacing and formation, but otherwise did not affect patterning or network formation. In contrast, it was shown that the temporal average intensity and acoustic pressure amplitude of the USWF influenced initial patterning of the cells within the hydrogel. Specifically, the intensity of the wave field more highly defined a minimum threshold to promote patterning and higher intensities generated thicker sheets at the pressure nodes [21]. The cell aggregate density influenced vascular network formation following polymerization of the hydrogel. Loosely aggregated sheets were found to form highly interconnecting vascular networks, whereas the more densely packed sheets formed capillary-like sprouts between sheets [21]. In the sham cultured group, HUVECs were observed to be randomly distributed in the gel and only formed tips and extensions ten days into culture [73]. It should be noted that the cross-sectional area of these extension, for both USWF and sham exposed samples, were predominantly characteristic of microvasculature. Interestingly, Garvin *et al.* noted that the vascular network was better influenced by the cell density in the sheets rather than the USWF parameters [20].

Ultrasound has offered significant usage as both a diagnostic and therapeutic tool. This review presents some of the applications of US for tissue engineering and regenerative medicine both *in vivo* and *in vitro*. With both low-intensity and acoustic trap approaches, ultrasound has provided alternatives to studying and generating tissue in the absence of scaffold materials or complicated processing steps. Furthermore, it has been shown that US has a variety of bioeffects ranging from exposure distance [139] and spatial patterning [18–21, 23, 73, 74, 77, 179, 180, 184] to membrane permeabilization [68]. In the case of LIUS, it has been shown that tissue

growth solely stimulated with US provides an equivalent, if not better effect, than growth and differentiation factors used for tissue generation [132, 143, 146]. This would suggest that US-induced differentiation of cells could be a more cost-effective alternative to media containing growth factors. Unfortunately, much of the existing LIUS literature provides conflicting information on tissue interaction with therapeutic ultrasound. The present acoustofluidics literature also suffers from a lack of biological data, though the physics and potential of USWFs is present and well characterized. As such, in the absence of a clear correlation between acoustic force interaction with cells and signalling pathways, caution remains key prior to application of many of these techniques to the patient and clinical setting. The next few years offer significant scope for translation and application in an ever increasing ageing population.

2.9 Current Cell Sources for Cartilage Engineering

For cartilage tissue engineering, the ideal cell source is one that can be easily isolated, expanded, and capable of synthesizing cartilage-specific matrix components [192, 193]. Several sources have been investigated in literature [193]; however, this review will focus on articular chondrocytes and stem cells.

2.9.1 Stem Cells

Stem cells are cells capable of prolonged or unlimited self-renewal under controlled conditions, and have the capacity to differentiate into a variety of specialised cell types [194]. The two classes of stem cells are pluripotent stem cells and somatic (adult) stem cells, both of which will be discussed in the context of cartilage generation.

2.9.1.1 Pluripotent Stem Cells

Pluripotent stem cells (PSCs) are stem cells capable of differentiating into tissue from any of the three germ layers and can self-replicate indefinitely [195, 196]. Cell populations capable of this plasticity are embryonic stem cells (ESCs) and induced pluripotent stem cells (iPSCs). ESCs are derived from the inner cell mass of a blastocyst, which impedes the use of these cells due to strict regulation and ethical

concerns [197]. It is well established that ESCs can form cartilage when the cells are transplanted in nude mice [196, 198], unfortunately *in vitro* protocols have limited efficiency where cell colonies are heterogeneous with a limited number of functional cells created [199]. Initial reports regarding *in vitro* ESC chondrogenesis utilized an embryoid body (EB) culture system [200], where free-floating cell aggregates differentiate at random into lineages of all three germ layers. Following this, either the whole body or single cells from the EBs are used for subsequent differentiation steps [196]. While it was shown that cells within EB displayed various stages of chondrogenesis, it is difficult to dissect the differentiation mechanisms using single cells, and control the size and number of EBs [196]. While further work with this cell population generated methods to induce chondrogenesis using different combinations of growth factors, differentiated cell states, and co-culture conditions, further optimization of these culture conditions is still required to maximize ECS differentiation into chondrocytes [196].

In part due to ethical concerns associated with the use of ESC, induced-pluripotent stem cells (iPSCs) have garnered interest due to their high differentiation capacity and the ability to generate them from adult cells reprogrammed to express ESC markers, such as OCT4 and NANOG [195–197]. These cells were generated using viral vectors; however, improved protocols has led to increased safety, efficiency, reduced tumourgenic potential via protein transduction facilitated by small-molecules [113, 197]. The differentiation capabilities of iPSCs are comparable to ESCs and because iPSCs can be generated from the patient's own cells, the risk of disease transmission, immunogenic rejection, and infection is greatly reduced [197]. Similar to ESCs, iPSC chondrogenesis has been reported using EB culture [195, 196, 201]. Other methodologies for generating chondrogenic cells from iPSCs involve co-culture of the cells with differentiated chondrocytes, which has shown promising results, albeit with low efficacy [195], as well as deriving mesenchymal stem-like cells from PSCs to bypass some of the limitations of MSC culture [195]. Additionally, biomaterial-based culture systems are also used to create skeletal tissue *in vitro*, unfortunately, much of this research is directed more towards disease modelling and not as well established as methods for cardiovascular and neuronal differentiation [202]. One last procedure to differentiating PSCs is referred to as directed differentiation where the stem cells are grown in feeder-free culture with conditioned medium to induce chondrogenesis. This

procedure was reported to effectively differentiate both ESCs and iPSCs into chondrocytes; however, cell death was noted in some cases and the overall procedure is complicated and requires numerous growth factors [195]. Ultimately, while iPSCs show significant potential for use in *in vitro* cartilage repair studies, their use in the clinic will still take several years before becoming a reality [197], however, significant progress has been made on the use multipotent and unipotent cells for cartilage repair, which is discussed below.

2.9.1.2 Adult Stem Cells

Adult stem cells are an undifferentiated multipotent cell population found within differentiated tissue. The cells are capable of self-renewal and can give rise to all mature cell types of its originating tissue. Mesenchymal stem cells are a subclass of adult stem cells with the potential to differentiate into cells found in connective tissue, such as fat, bone marrow, muscle, periosteum, and synovium [196]. The use of MSCs from bone marrow to adipose tissue for cartilage tissue engineering has been extensively researched [196, 197], but the term is non-specific and refers a progenitor of a wide range of connective tissues (mesenchyme) [194, 203, 204]. The term "skeletal stem cells" (SSCs) was therefore introduced to denote MSCs derived from the bone marrow stroma [205].

SSCs are an attractive prospect for tissue repair because the cells lack immunogenicity despite their limited growth potential *in vitro* [194]. Friedenstein *et al.* first reported tissue culture plastic-adherent cells isolated from the non-haematopoetic fraction of bone marrow aspirates as being clonogenic fibroblast-like precursor cells (colony forming unit-fibroblastic/CFU-F) [206]. In addition, this progenitor cell population is characterized by the ability of clonal cell populations to generate chondrocytes, osteoblasts, smooth muscle cells, among others [204, 207]. Muraglia *et al.* [208] suggests that these tissue culture plastic (TCP)-adherent cells are highly heterogeneous. It was reported that one third of 185 clones were capable of tripotency (the clonal populations exhibited adipo-, osteo-, and chondrogenesis), while the remaining clones only exhibited a differentiation potential into the osteo-chondral lineage. Given this, it would be incorrect to refer to these cells as SSCs solely on the basis of TCP-adherence [207]. While the identity of a single, characteristic biomarker

for skeletal stem cells is still unknown, a number of molecules have been categorically defined in their expression within SSCs (Table 2.3 and more comprehensively in [194]) as well as practical concerns regarding stem-ness potential and isolation fraction [209].

Biomarker	**Expressed**	**Not Expressed**	**Details**
STRO-1 antigen	X		Cell-surface trypsin-resistant antigen expressed by CFU-F, Antibody: STRO-1
Tissue nonspecific alkaline phosphatase (TNSALP)	X		Cell-surface glycoprotein associated with osteoblast lineage cells, Antibody: STRO-3
CD63	X		Cell-surface antigen; Synonyms: Melanoma-associated antigen ME491, Tetraspanin 30, Lysosomal-associated membrane protein 3, Antibody: HOP26
CD105	X		Cell-surface antigen; Synonym: Endoglin/SH2
CD73	X		Cell-surface antigen; Synonym: SH3/4
CD71	X		Cell-surface antigen; Synonym: Transferrin receptor protein 1 (TfR1)
ICAM-1	X		Cell-adhesion molecule; Intercellular cell-adhesion molecule-1
CD29	X		Cell-adhesion molecule; Synonym: β1 subunit of the integrin family
CD31		X	Cell-adhesion molecule; Synonym: Platelet/endothelial cell-adhesion molecule-1 (PECAM-1)
CD56		X	Cell-adhesion molecule; Synonym: Neural cell-adhesion molecule-1 (NCAM-1)
CD18		X	Cell-adhesion molecule; Synonyms: Leukocyte cell-adhesion molecule, integrin β2 (LCAMB), Lymphocyte function associated antigen-1 (LAD, LFA-1)

Table 2.3: List of cell surface and adhesion molecules known to either be expressed or not expressed in skeletal stem cells.

STRO-1 has historically referred to the antibody [194, 204] binding to a cell-surface marker, referred to as trypsin resistant antigen 1 [210]. This marker has been used to selected for a population of bone marrow mononuclear cells (BMMCs) that is enriched in SSCs [194, 204, 210, 211]. For the purposes of this thesis, STRO-1 will refer to the antigen and cells selected for STRO-1 expression will be referred to as STRO-1+ cells. STRO-1+ cells selected from BMMCs and CD146+/CD45- stromal cells from the

perivascular spaces in bone marrow [212] have been reported to generate bone and stroma. The use of STRO-1+ SSCs has been focused on regenerating bone [194, 204], but their use for cartilage repair is not extensively known. Few published studies have shown that it is possible to generate cartilaginous tissue using SSCs [194, 213]; however, the chondrogenic potential of the cells is variable and fibrocartilage formation has been noted in the culture [211, 214]. Further optimization of strategies is needed to limit fibrocartilage formation and uniform cartilage formation.

2.9.2 Chondrocytes

As cells natively found in articular cartilage, chondrocytes are the obvious cell type of choice for cartilage tissue engineering. Chondrocytes sense mechanical loads experienced by the tissue through integrins, syndecans, and ion channels [215]. Within the cartilage matrix, chondrocytes also exist in a low oxygen environment, ranging from 10% O_2 at the tissue surface to 1% in the deep zones. The environmental changes in relation to the depth are further seen in the matrix and gene expression by the chondrocytes, where superficial zone chondrocytes are noted to more highly express lubricin and deeper zone chondrocytes express Runx2 [28].

Isolation of chondrocytes from human tissue is accomplished via enzymatic digestion and can be easily cultured *in vitro* [216]. Unfortunately, despite the potential of the cells to produce the necessary matrix proteins to regenerate cartilage, the cells have a tendency to de-differentiate *in vitro*, thus losing their chondrocyte phenotype [216]. Cultivation of chondrocytes with certain growth factors, such as transforming growth factor beta 3 (TGF-β3), high cell densities, and in 3D cultures have been shown to preserve the phenotype *in vitro* [3, 216]. Additionally, hypoxic culture conditions was shown to maintain their phenotype as the cells up-regulate genes associated with chondrogenesis [28]. The cells also exhibit a low proliferation rate in monolayer, which further limits their application [217].

The further development of cartilaginous tissue would require an optimized cell source, whereby the tissue structure is the best representation of native, healthy tissue. The presented cell sources all have certain advantages and limitations and further optimization would be required to ensure robust and consistent cartilage generation. Adult stem cells provide the most potential due to their accessibility and plasticity to

differentiate into multiple cell types. One of the primary limitations with this cell source is identifying the specific sub-population with the highest chondrogenic potential. Further research is needed to validate the selection of highly chondrogenic stem cells, whether it be the tissue source (e.g. adipose tissue, bone marrow, etc) or sorting criteria. Some literature suggests co-culture of stem cells with chondrocytes to promote interaction of the stem cells with differentiated cells and more direction towards a chondrogenic lineage; unfortunately, there exists conflicting reports regarding the success of this approach in generating robust cartilage [218–221].

Chapter 3

Co-culture of Skeletal Stem Cells and Articular Chondrocytes For Robust Cartilage Development

3.1 Introduction

Due to the limited self-repair capacity of articular cartilage, surgical restorative techniques, such as autologous cell implantation (ACI), have been used to treat and repair articular cartilage lesions [33]. This technique, however, is associated with a number of limitations related to the long term sustainability of the tissue, namely donor site morbidity, insufficient or limited cell population from the harvested tissue and subsequent de-differentiation of the harvested chondrocytes during monolayer expansion. Maintenance of the chondrocytes and the chondrocyte phenotype *in vitro* has been investigated through cell culture with certain growth factors, such as transforming growth factor beta 3 (TGF-β3), as well as using high seeding densities in both 2D and in 3D culture [3, 216]. Additionally, hypoxic culture (2–5%) has been shown to maintain the phenotype as the chondrocytes up-regulated genes associated with chondrogenesis, such as aggrecan, and Col2a [28, 222]. Unfortunately, as the quality of the excised cartilage and, therefore, resulting tissue can be variable between patients, present literature has presented the potential of alternative cell sources and treatments for cartilage generation *in vitro*.

Stem cells present in the bone marrow have also garnered interest for cartilage repair due to their capacity for self renewal and differentiation into multiple lineages in response to appropriate signals [206]. Traditionally, these cells are selected for plastic adherence from bone marrow mononuclear cells (BMMNCs) [206, 207]. Bone marrow derived stem cells display tri-potency to differentiate into osteoblasts, adipocytes, and chondrocytes *in vitro* [209]. Bone marrow cultures established solely on the basis of plastic adherence have been shown to contain both multipotent skeletal stem cells (SSCs) and differentiated progenitor cells [223]. To enrich the BMMNC population for SSCs, cell surface markers expressed by the stem cell population have been proposed as a selection tool, reviewed recently by Lv *et al* [209]. Selection markers proposed for SSCs are categorized as either sole markers—specific markers for selecting SSCs—or stem-ness markers, which enrich for sub-populations of tripotent stem cells [209]. The identity of a sole, characteristic biomarker that specifically recognizes SSCs remains unknown, however, it has been reported that SSCs express CD105, CD73, and CD90, while lacking expression cell-surface markers indicative of haematopoietic cells, such as NCAM, CD31, CD40, and CD18 [194, 204, 209]. A more comprehensive list of markers both expressed and lacking in skeletal stem cells is summarized in Tare *et al.* [194].

A number of markers have been suggested for stem cell selection, including STRO-1, CD271, stage-specific embryonic antigen-4 (SSEA-4), and CD146 [209]. STRO-1, or trypsin resistant antigen 1 [210, 224], is expressed by a sub-population of BMMNCs enriched in SSCs [194, 204, 207]. The use of STRO-1+ SSCs has been focused on regenerating bone [194, 204], but their use for cartilage repair is not extensively known. Few published studies have shown that it is possible to generate cartilaginous tissue using SSCs [194, 213]; however, the chondrogenic potential of the cells is variable and fibrocartilage formation has been noted in the culture [211, 214]. Previously, our group compared the chondrogenic potential of human articular chondrocytes to STRO-1+ skeletal stem cells in 21 day 3D pellet cultures and membrane scaffolds from Alvatex [225]. In both culture conditions, STRO-1+ cells displayed a tendency to undergo hypertrophy and were unable to generate robust hyaline-like cartilage.

To circumvent the hypertrophic tendencies of MSCs/SSCs, literature has shown the potential of co-culture to enhance cell-cell interactions and potentially improve functional tissue formation [226, 227]. For cartilage engineering, co-culture of stem cells with chondrocytes has been suggested to improve functional cartilage

development [219, 220]. Previous reports have demonstrated that the development of constructs from a co-culture of MSCs and articular chondrocytes reduces the expression of hypertrophic markers and result in better mechanical properties compared to structures generated from a MSC only population [220]. Fischer *et al* suggest that the human articular chondrocytes (HACs) release factors into the environment, which direct MSC differentiation into chondrocytes and the formation of stable tissue [228]. These findings, however, have been reported using cells seeded onto biodegradable scaffolds, varying co-culture ratios, or dissimilar sources of stem cells to chondrocytes [218–221].

In this chapter, I examine the cartilage constructs assembled between STRO-1 selected SSCs and HACs in pellet culture, a scaffold-free cartilage model system used to study chondrogenesis with minimal external influences. To better quantify the interactions between the chondrocytes and stem cells, both cell populations were harvested from the same osteoarthritic patients to better understand the chondrogenic potential of equal and biased co-cultures in the culture system. The findings from this chapter will be used to identify an effective chondrogenic cell population for use within the acoustofluidic bioreactor, wherein the cells will be subjected to various mechanical stimulation regimes to determine the biomechanical relevance of the acoustically derived stimulation on cell differentiation.

3.2 Materials and Methods

All chemicals were purchased from Sigma-Aldrich UK and Invitrogen UK, unless stated otherwise. Human femoral head samples and bone marrow samples were obtained from 3 haematologically normal OA patients (female, ages: 59-85) following routine total hip replacement. Only tissue that would have been discarded was used in this study with approval of the Southampton and South West Hampshire Research Ethics Committee (194/99/1 & 210/01).

3.2.1 Isolation of STRO-1+ Skeletal Stem Cells

The SSC-enriched STRO-1+ cell population was isolated by magnetically activated cell separation (MACS) as described previously [229].

Cells were extracted from bone marrow aspirates through agitation in α-MEM. Following this, the cell suspension was washed three times to remove fat deposits by centrifuging the cell suspension for five minutes at 300*g. The supernatant was discarded and the pellet was re-suspended in α-MEM and filtered through a 70 µm sieve to remove bone fragments. The resulting cell suspension was then layered carefully over Lymphoprep (Axis-Shield Diagnostic, Dundee, UK, 1114547) and centrifuged to remove red blood cells by graded sedimentation for 45 minutes at 800*g. To prevent disruption of the interface and cells (buffy coat) between the Lymphoprep and α-MEM, the centrifuge was set to the lowest deceleration setting. Bone marrow mononuclear cells (BMMNCs) collected from the buffy coat at the interface were treated with MACS blocking buffer—1% FBS, 0.2% bovine serum albumin (BSA), 2% AB serum human in α-MEM—for thirty minutes at 4°C. The cells were then washed in MACS buffer (2 mM EDTA and 5% BSA in PBS) three times for five minutes at 300*g prior to incubation with the mouse monoclonal STRO-1 antibody (undiluted supernatant harvested from the STRO-1 hybridoma in-house) for one hour at 4°C. The cells were then washed in MACS buffer three times for five minutes at 300*g prior to incubation with Rat anti-mouse IgM antibody conjugated to microbeads (1:5 dilution, Milltenyi Biotec 130-047-301) for one hour at 4°C. The cells were then washed in MACS buffer three times for five minutes at 300*g and then introduced into a MACS LS column (Milltenyi Biotec 130-042-401) to fractionate the STRO-1+ cells from the STRO-1- population. The column was washed three times with MACS buffer to purify the STRO-1+ fraction before removal from the magnetic field and seeding of purified suspension into cell culture flask (300,000 cells/cm^2, seeding density).

STRO-1+ cells were cultured to confluence in monolayer cultures in basal medium (α-MEM supplemented with 10% (v/v) fetal bovine serum, FBS, 100 unit/ml penicillin and 100 µg/ml streptomycin) in humidified atmosphere at 37°C, 5% CO_2 and 21% O_2.

3.2.2 Isolation of Human Articular Chondrocytes

HACs were isolated by sequential enzymatic digestion of deep-layer articular cartilage pieces dissected from the non-load-bearing region of the femoral heads [230]. Pieces of deep-layer cartilage were dissected from the heads and digested in 500 µg/mL trypsin-EDTA for 30 minutes at 37°C and 5% CO_2. Following the incubation, the

tissue fragments are washed in PBS then incubated in 1 mg/mL hyaluronidase for 15 minutes at 37°C and 5% CO_2,. The fragments were washed in PBS to remove excess hyaluronidase and then incubated in 10 mg/mL collagenase B (Roche Diagnostics 11088807001) overnight at 37°C on a rotating mixer at 1200 rpm. The resulting solution was filtered through a 70 µm sieve to remove undigested tissue, before diluting the suspension in α-MEM. The cells were centrifuged for ten minutes at 400*g, after which the pellet was re-suspended in complete medium and the cells were seeded onto a cell culture flask (150,000 cells/cm^2).

Isolated chondrocytes were cultured to confluence in monolayer cultures in α-MEM supplemented with 10% (v/v) FBS, 100 unit/mL penicillin, 100 unit/mL streptomycin, and 100 µM ascorbate 2-phosphate (A2P). Cultures were maintained in humidified atmosphere at 37°C, 5% CO_2, and 21% O_2.

3.2.3 ATDC5 Cell Culture

Immortalized murine chondrocytes (ATDC5, Lonza) were used to validate cell viability and tissue formation within the bioreactor. These cells were maintained in Dulbecco's modified eagle medium (DMEM, Lonza) with 5% FBS, 1x insulin-transferrin-selenium (ITS, 100x stock solution, 13146), and 100 unit/ml penicillin and 100 unit/ml streptomycin in humidified atmosphere at 37°C, 5% CO_2 and 21% O_2.

3.2.4 Pellet Culture

Pellet cultures were performed in accordance with a previously published protocol [204].

Monolayer cultured HACs and STRO-1+ SSCs were harvested at confluence and suspended in serum-free chondrogenic media at a final concentration of 300,000 cells/mL. 1 mL of the cell suspension was added to a 25 mL polycarbonate universal tube and centrifuged for 5 minutes at 400*g. The resulting cell pellet was cultured in normoxic conditions (37°C, 5% CO_2 and 21% O_2) wit media changed every 2 days over a 21-day culture period. For co-culture experiments, HACs and STRO-1+ SSCs were combined in ratios of 1:2 HAC/STRO-1+, 2:1 HAC/STRO-1+, and 1:1 HAC/STRO-1+ to generate a pellet of 300,000 cells for each condition. At the end of

the culture period, pellets were fixed overnight in 4% para-formaldehyde (PFA, P6148) at 4°C.

Chondrogenic media consisted of α-MEM supplemented with transforming growth factor-beta (10 ng/mL, TGF-β3, Peprotech 100-36E), 1x ITS (10µg/ml insulin, 5.5µg/ml transferrin and 5ng/ml selenium premix), dexamethasone (10 nM, D4902), and L-ascorbate-2-phosphate (100µM, A2P, A8960).

3.2.5 Cell Labelling with Membrane Probes

Cell distribution in co-culture pellets was visualized using green (PKH67) and red (PKH26) fluorescent membrane probes. Membrane probes were part of a kit (MINI67, MINI26) including a diluting solution (diluent C). Standardization of dye/probe concentrations and labelling of the cells was accomplished using the manufacturer's instructions. Following trypsinization, cells were washed with serum-free medium. The cell density was then determined and a maximum concentration of $1x10^7$ cells/mL was re-suspended in 250 µL of diluent C. The stock dye solution was prepared by adding 1 µL of the PKH67 dye to 249 µL of diluent C to give a final concentration of 4 µM. A stock PKH26 dye solution was prepared by adding 1 µL to 249 µL of diluent C to give a final concentration of 4 µM. This solution was added to the cell suspension (final, working concentration of dye in suspension is 2 µM) and incubated at room temperature for 5 minutes. The reaction was stopped using 500 µL of FBS and the labelled cells were washed once in 10% FBS in α-MEM prior to use in co-culture.

Additional concentrations were used to assess cell uptake of the fluorescent probes (Table 3.2).

Dye Volume (µL)	**Diluent C Volume (µL)**	**Working Concentration (µM)**	**Final Concentration (µM)**
0.5	249.5	2	1
1	249	4	2
2	248	8	4
4	246	16	8
8	242	32	16
10	240	40	20
12	238	48	24

Table 3.2: Table of tested membrane probe concentrations. Manufacturer's suggested working concentration was 4 µM diluted to 2 µM when labelling cells. Efficacy of additional working concentrations were explored by multiples of 2.

3.2.6 Staining Preparation and Procedures

For immunofluorescence chemistry and histological staining, all steps were carried out at room temperature, unless stated otherwise.

3.2.6.1 Immunofluorescent staining of STRO-1 selected SSCs

Isolated STRO-1+ cells were cultured onto sterile cover-slips for 13 days prior chemical fixation in 4% PFA for 20 minutes. The cells were washed in PBS twice to remove excess PFA and incubated in permeabilization buffer (0.1% Triton-X and 1% BSA in PBS) for 5 minutes. The permeabilization buffer through incubating in a wash buffer (0.5% Tween-20 in PBS) for minutes, repeated three times. The cells were then introduced to a blocking buffer (1% BSA in PBS) for five minutes prior to incubation with mouse monoclonal STRO-1 antibody (undiluted supernatant harvested from the STRO-1 hybridoma in-house) for one hour. The unbound antibodies were removed with the wash buffer and cells were then incubated with the secondary antibody (1:50 dilution, AlexaFluor488 anti-mouse) for one hour with agitation. The excess, unbound antibodies were washed from the cover-slip and the cells were counter-stained with

DAPI nuclear stain (1:200 dilution) for 5 minutes before mounting onto a glass slide for imaging.

3.2.6.2 Cryo-Embedding and Sectioning

Tissue samples labelled with membrane probe underwent cryo-embedding as to preserve fluorescence activity. Fixed samples were washed in PBS before overnight incubation in 30% sucrose in PBS at 4°C. The samples were then washed in OCT embedding matrix (CellPath KMA-0100-00A) to remove excess sucrose, following which they were immersed in cryo-moulds containing OCT. The moulds were placed in a solution of isopropanol and dry ice to freeze. The frozen moulds were stored at -80°C until ready to section. Sequential sections were cut 10 µm thick on the cryotome—maintained at -20°C—and mounted on glass slides for confocal imaging.

For histological and immunohistochemical staining, cryo-sections were thawed to room temperature and washed in PBS to remove OCT.

3.2.6.3 Paraffin Embedding and Sectioning

Fixed samples were washed in PBS before processing through graded ethanol (50%–100%), followed by clearing with Histoclear (National Diagnostics HS-200). The tissue samples were then embedded in paraffin wax (Fisher 8002-74-2). Sequential sections were cut 7 µm thick on the microtome and mounted on glass slides.

For histological and immunohistochemical staining, paraffin sections were de-waxed and re-hydrated through Histoclear wash, followed by graded ethanol (100%–50%).

3.2.6.4 Alcian Blue/Sirius Red (A/S) Staining

Alcian Blue stained the proteoglycan-rich cartilage matrix, while Sirius Red stained the collagen-rich matrix.

Sections were de-waxed and re-hydrated as described previously, then stained for the nuclei with Weigert's Haematoxylin [231] for ten minutes. Excess haematoxylin was removed through a ten minute wash in distilled water, followed by three dips in

acid/alcohol (0.5% (v/v) concentrated HCl in 50% (v/v) methanol). The sections were then washed in distilled water for five minutes before immersion in Alcian Blue 8GX (5 mg/ml in 1% (v/v) glacial acetic acid) for ten minutes. The excess staining solution was washed off in distilled water for one minute and the slides were introduced into molybdophosphotidic acid (3 mg/mL in distilled water) for twenty minutes. Following this, the slides were washed and left in Sirius Red F3B (10 mg/ml in saturated picric acid) for one hour. The slides were washed in water for one minute, then dehydrated through graded ethanol (50%–100%) and Histoclear. Glass cover-slips were mounted with DPX and allowed to dry for at least two hours.

3.2.6.5 Immunohistochemistry Staining

After de-paraffinization and re-hydration, sections were quenched of endogenous peroxidase activity with 3% (v/v) H_2O_2 for five minutes at room temperature and blocking with 10 mg/ml BSA in PBS for five minutes at 4°C. Sections were incubated with relevant primary antiserum at 4°C overnight. This was followed by three five minute washes in wash buffer (0.5% Tween 20 in PBS). Slides were then incubated for one hour with the appropriate biotinylated secondary antibody (dilution 1:100), washed three times for five minutes and then incubated for thirty minutes with ExtrAvidin-Peroxidase (dilution 1:50). Visualization of the immune complex involved the avidin-biotin method linked to peroxidase and AEC (3-amino-9-ethylcarbazole), resulting in a reddish brown reaction product following ten minute exposure with 30% peroxide. Negative controls (omission of the primary antisera) were included in all immunohistochemical procedures. No staining was observed in all negative control sections. All sections were counter-stained with Alcian Blue 8GX. Glass cover-slips were mounted with hydromount and allowed to dry for at least two hours.

The anti-SOX-9 antibody (rabbit polyclonal, IgG, Millipore, Watford, UK) was used at a dilution of 1:150 in 10 mg/ml BSA in PBS following the antigen retrieval procedure, which involved treating sections in 0.01M citrate buffer (pH 6.0) for thirty minutes at 75°C before the application of the standard Immunohistochemistry procedure.

For immunostaining using anti-collagen Type I, II and X antibodies as well as osteopontin (OPN), sections were treated with Hyaluronidase (0.8 mg/ml) at 37°C for 20 minutes in order to unmask the collagen fibres and render them accessible for

immunostaining. The LF68 anti-collagen Type I antibody (COLI rabbit IgG, gift from Dr Larry Fisher), anti-collagen Type II antibody (COLII rabbit IgG, Calbiochem, Watford, UK), anti-collagen Type X antibody (COLX rabbit IgG, Calbiochem, Watford, UK), and anti-OPN antibody were used at a dilution of 1:1000, 1:500, 1:100, and 1:100 respectively.

3.2.6.6 Alkaline Phosphatase Histochemical Staining

Sections were fixed using 90% ethanol and immersed in activation buffer (Tris Maleate buffer, pH 7.4) overnight at room temperature. The slides were washed prior to interaction with Naphthol AS-B1 phosphate and the diazonium salt (Fast red), which is precipitated at the site of the enzyme activity. The slides were mounted as described above.

3.2.7 Microscopy

Fluorescence images were obtained using a Zeiss Axiovert 200 inverted fluorescence microscope (Zeiss, UK) with FITC filter (excitation/emission wavelengths: 485 nm/515 nm, Carl Zeiss), Rhodamine filter (excitation/emission wavelengths: 546 nm/560 nm, Carl Zeiss), and CCD camera with Axiovision software. PKH-labelled co-culture sections were imaged using a Leica TCS-SP5 laser scanning confocal microscope (Leica, Germany), operated through Leica LAS-AF software. Histological sections were imaged using Olympus BX 51 dotSlide virtual slide microscope system (Olympus Microscopy).

3.2.8 Image Analysis

Histology images were analysed for collagen and GAG staining area by colour-segmentation using k-means cluster analysis (section A.1). The source image (Figure 3.1A) was converted from RGB to L*a*b colour space. The colour information for the tissue section was then isolated from the image by focusing on the information in the a*b colour space. K-means clustering was then used to statistically analyse the mean pixel intensities and partition the pixel locations and values into three clusters (k = 3) (Figure 3.1B). This process was replicated three times to minimize cluster overlap.

The algorithm segmented the pixels values such that two clusters contained the pixel colour values on opposite ends of the A*B colour spectrum (Figure 3.1Bi, ii). Practically in a case of an IHC image, the algorithm would categorize the counter-staining (i.e. Alcian Blue) into one cluster and the target staining (i.e. AEC staining). The third cluster contained the intermediary values within the spectrum (Figure 3.1Biii). Correspondingly, for A/S staining, the algorithm would group the pixel values according to the Alcian Blue staining, Sirius Red, and intermediate values Figure 3.2. The stained area was isolated from cluster 1 and cluster 3 (Figure 3.1Ci) the background and countering staining was truncated to fully isolate the stained area within the section from the entire image (Figure 3.1Cii). Morphological filtering was applied to ensure segmentation of the whole section (Figure 3.1D).

The computed staining area was then normalized to the total section area to give an area fraction. To compare the relative size of the co-culture conditions, the pellet size was normalized to the HAC control pellet for a given patient.

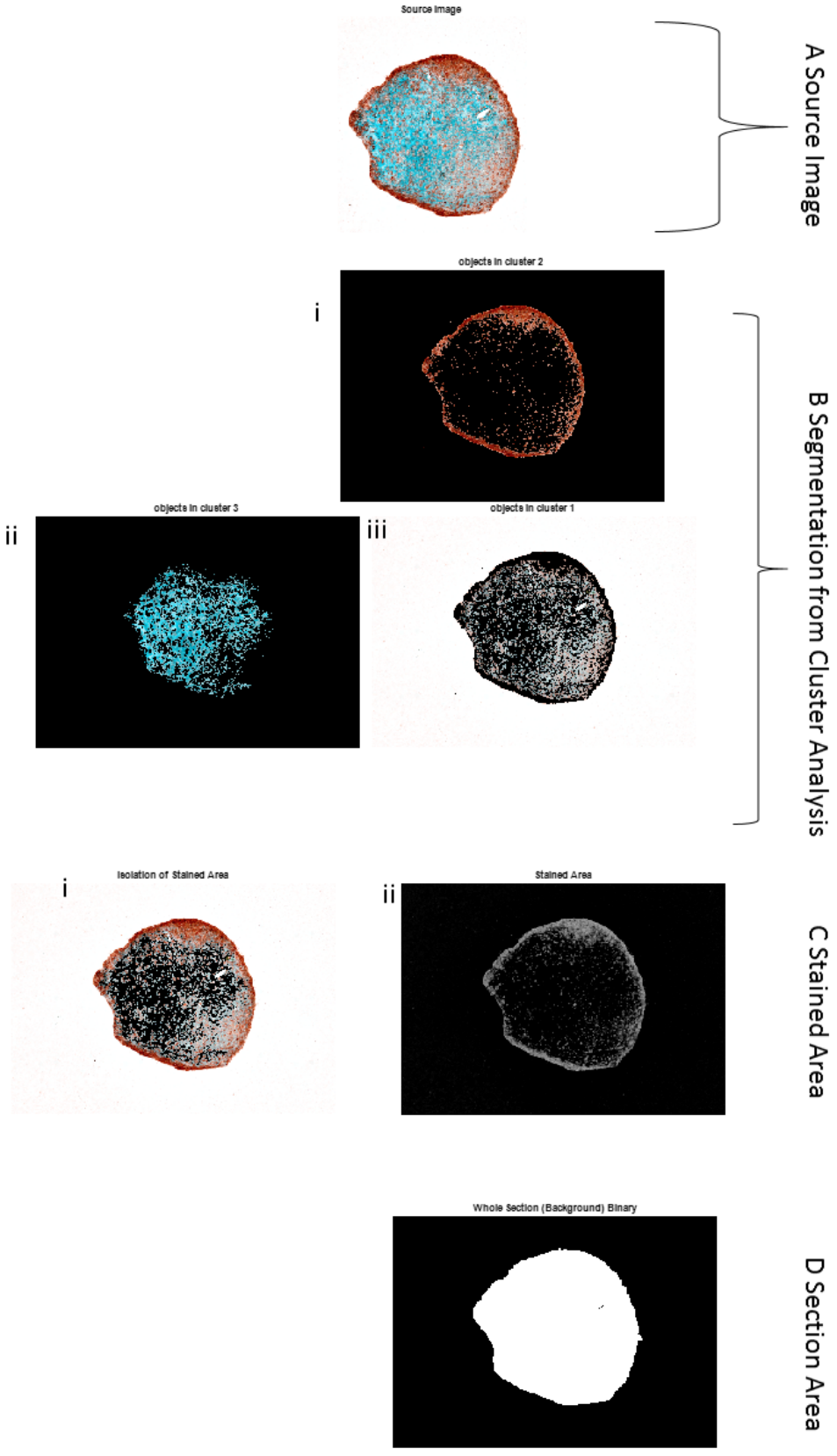

Figure 3.1: Diagram illustrating image analysis algorithm. (A) Source image segmented into three clusters. (B) The data within the clusters was split such that (i) one cluster contained the pixels highly expressing the target staining colour, (ii) another cluster contained the counter staining, and (iii) the last cluster consisted of the remaining pixels. (C) The first and last clusters were used to (i) isolate the stained area within the section. Following this, the background and other irrelevant blobs were truncated from the image to show (ii) the staining area in grayscale. (D) Following acquisition of the target area, the whole section was labelled via global thresholding and a fill holes algorithm was applied to the image to generate a more complete section silhouette.

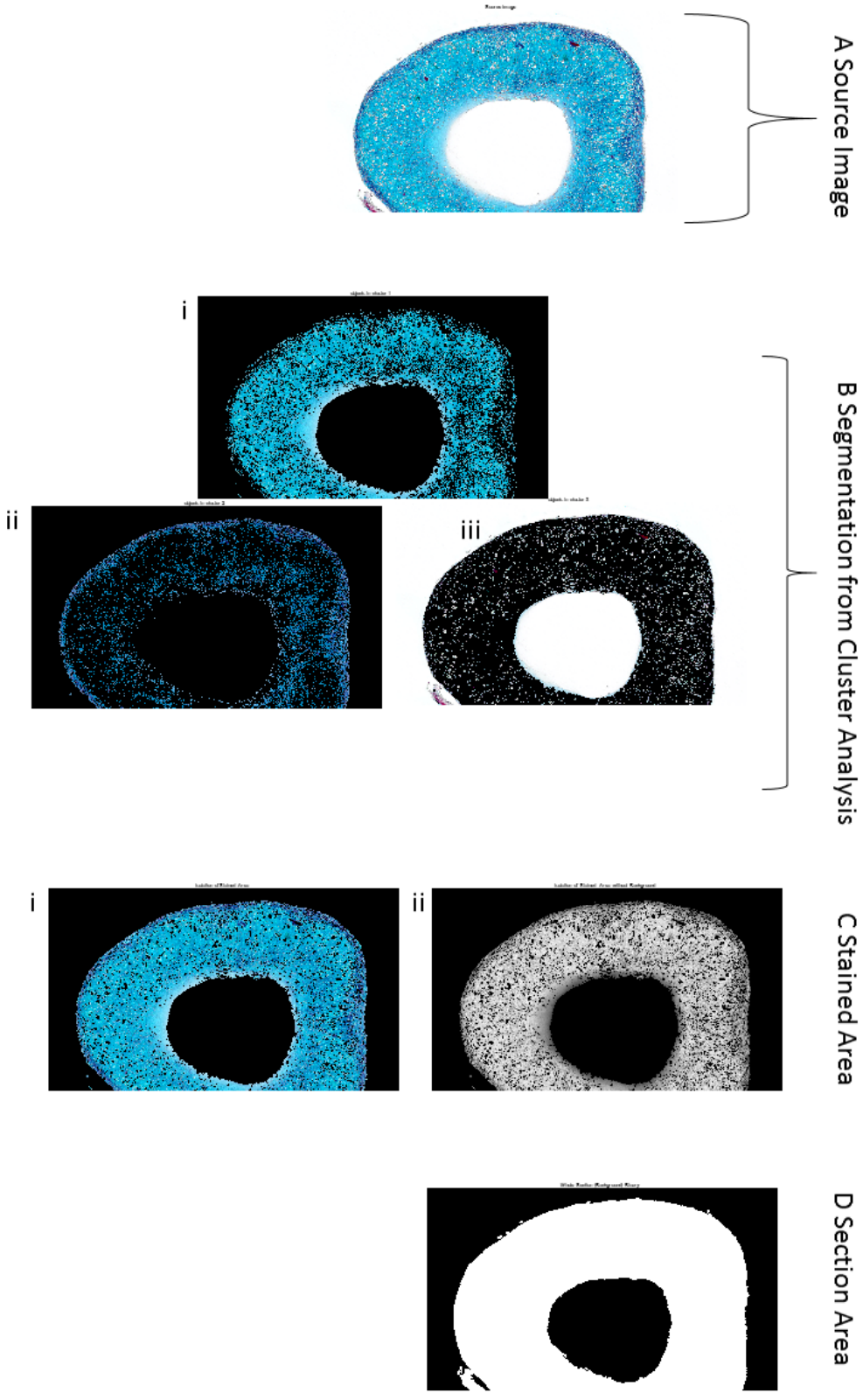

Figure 3.2: Diagram to illustrate similar working principle for isolating GAG staining from A/S stained images as Figure 3.1

3.3 Results

3.3.1 Characterization of HACs and STRO-1+ SSCs

HACs were isolated from femoral heads following total hip arthroplasty (THA) surgeries. Tissue sections from the deep layers of cartilage lining the head were treated with Trypsin/EDTA for 30 minutes, followed by hyaluronidase for 15 minutes and collagenase B overnight with agitation. Remaining tissue fragments were discarded and the cells were plated, where they assumed a fibroblastic morphology (Figure 3.3).

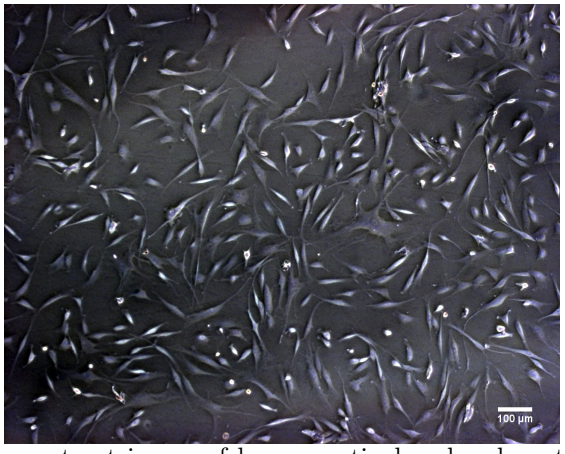

Figure 3.3: Phase contract image of human articular chondrocytes in monolayer at passage 0. Scale bar at 100 µm

SSCs were isolated from bone marrow aspirates by selecting mononuclear cells conjugated to STRO-1 antibodies through MACS. 13 days following isolation, cells were fixed and stained for expression of STRO-1 (Figure 3.4).

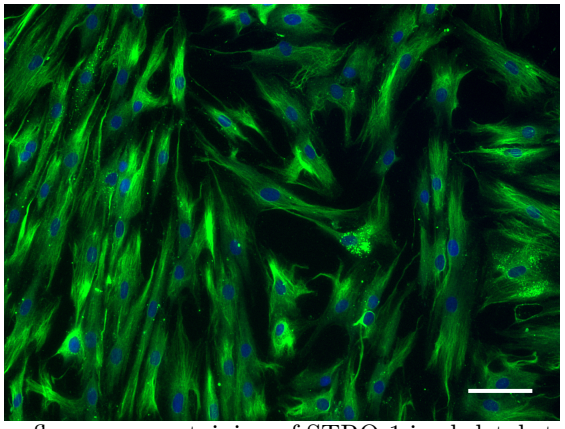

Figure 3.4: Immunofluorescence staining of STRO-1 in skeletal stem cells grown in in monolayer at p0. Scale bar = 100 µm.

3.3.2 Membrane Labelling Characterization and Optimization

To visualize the cell population distribution within the co-culture pellets, the HACs and SSCs would be labelled with a fluorescent membrane probe. Prior to use with co-culture pellets, PKH membrane probes were characterized for staining intensity in monolayer culture of ATDC5 cells. The manufacturer's suggested concentration of 2 µM was used as the base concentration and compared against higher and lower concentrations (Table 3.2). PKH26 staining intensity was overall found to be weaker below 20 µM (Figure 3.5). In contrast, PKH67 fluorescence intensity was noticeable at the suggested concentration of 2 µM, but more visible at 8 µM, where the probe provided more uniform staining of the cells (Figure 3.6).

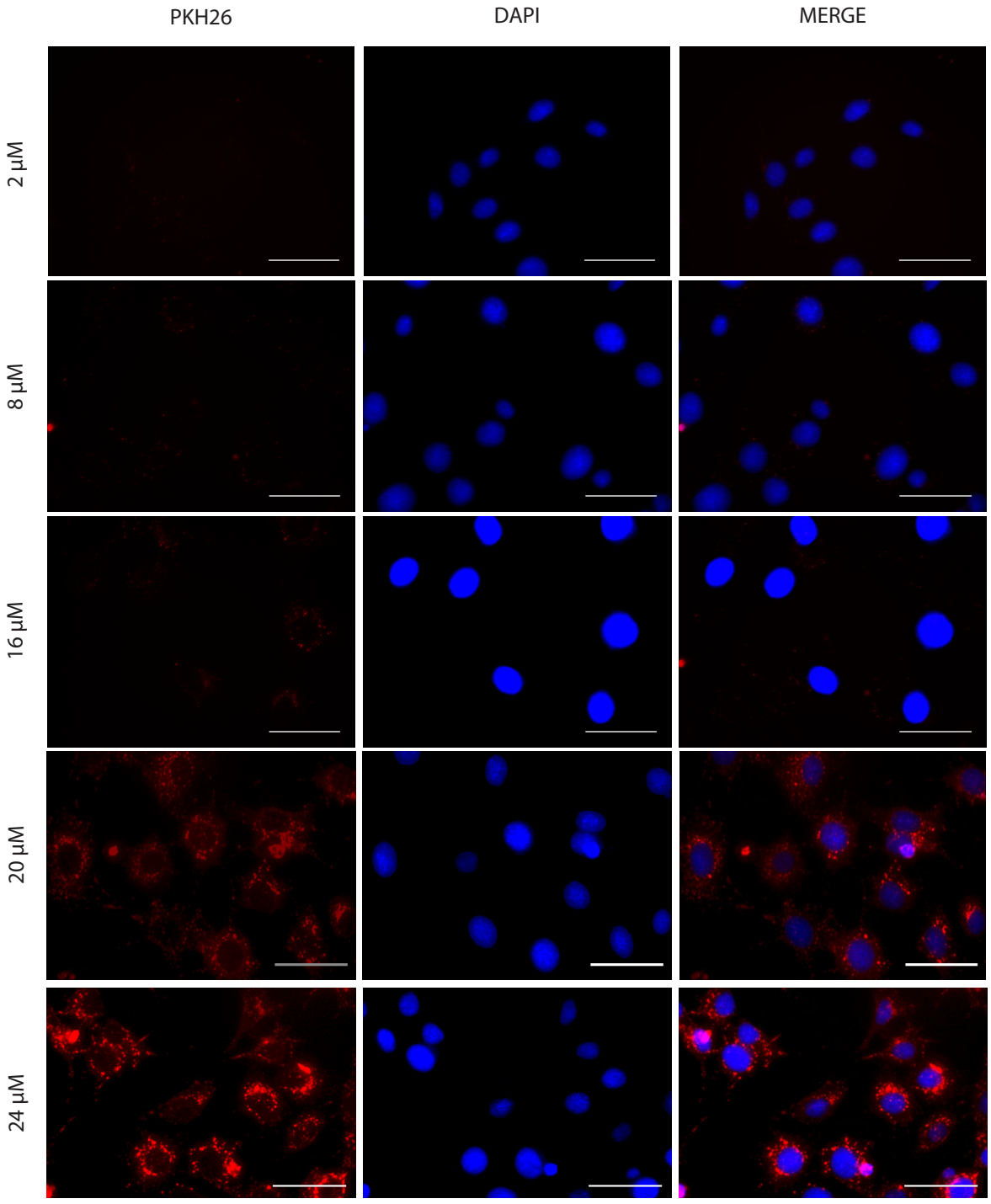

Figure 3.5: Characterization of fluorescent membrane probe intensity at varying concentrations. ATDC5 cells were labelled before re-plating on tissue culture plastic. Following this, the cells were incubated overnight, fixed, and imaged the following day using an epifluorescence microscope. Manufacturer's suggested concentration for both PKH26 (red) was 2 µM, which was set as the standard for the camera exposure. Scale bars = 50 µm.

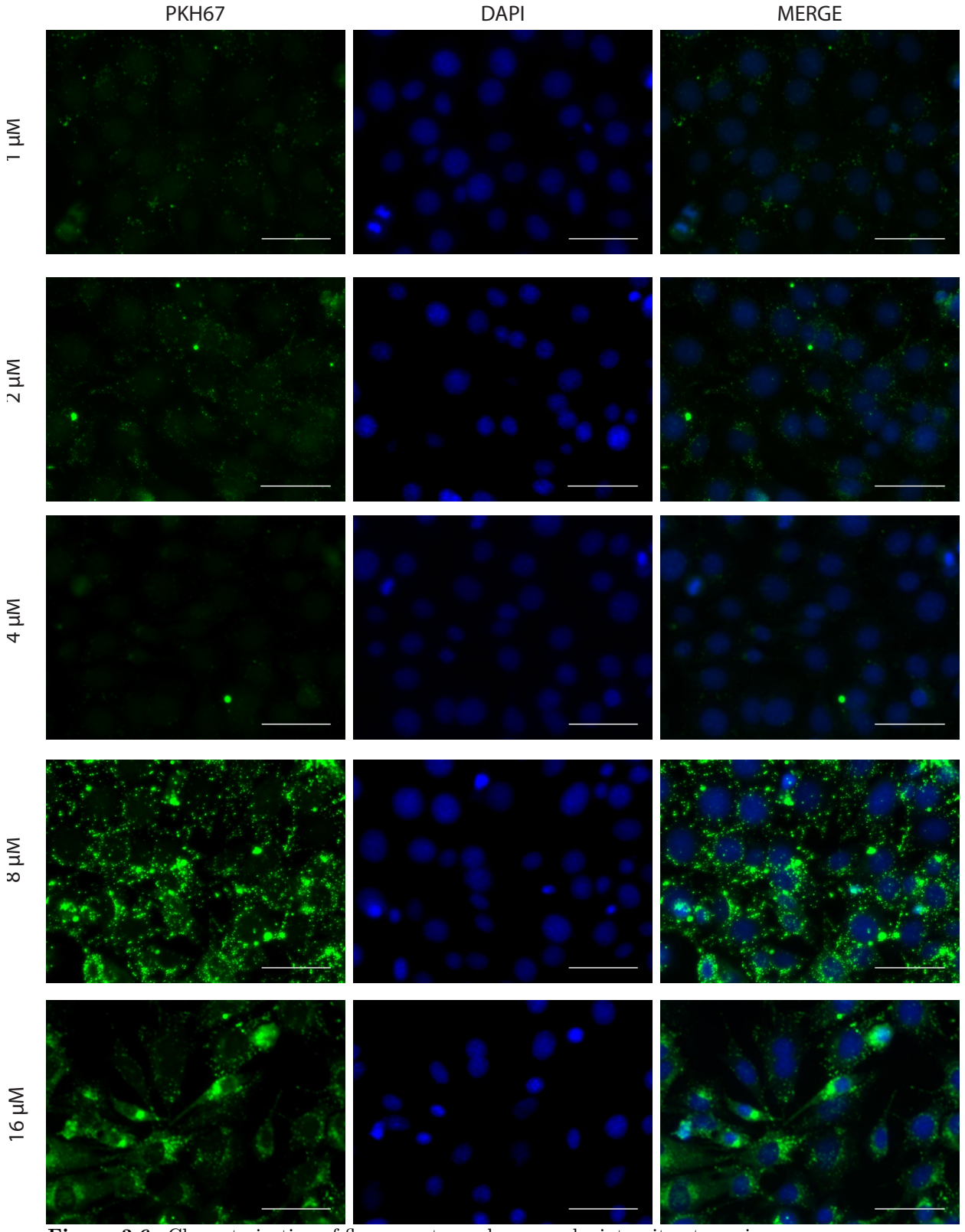

Figure 3.6: Characterization of fluorescent membrane probe intensity at varying concentrations. ATDC5 cells were labelled before re-plating on tissue culture plastic. Following this, the cells were incubated overnight, fixed, and imaged the following day using an epifluorescence microscope. Manufacturer's suggested concentration for PKH67 (green) was 2 µM, which was set as the standard for the camera exposure. Scale bars = 50 µm.

Following this, cells were then labelled with either PKH26 (24 µM) or PKH67 (8 µM) to quantify cell-cell interactions with the two labels. Appreciable staining of PKH26 was noted and significant co-localization was noted (Figure 3.7). Given that these images were captured on an epifluorescence microscope with a wide-pass FITC filter, subsequent fluorescent imaging of the cell distribution would be captured using confocal microscopy to ensure separation of the PKH26 and PKH67 signals in individual cells during pellet culture.

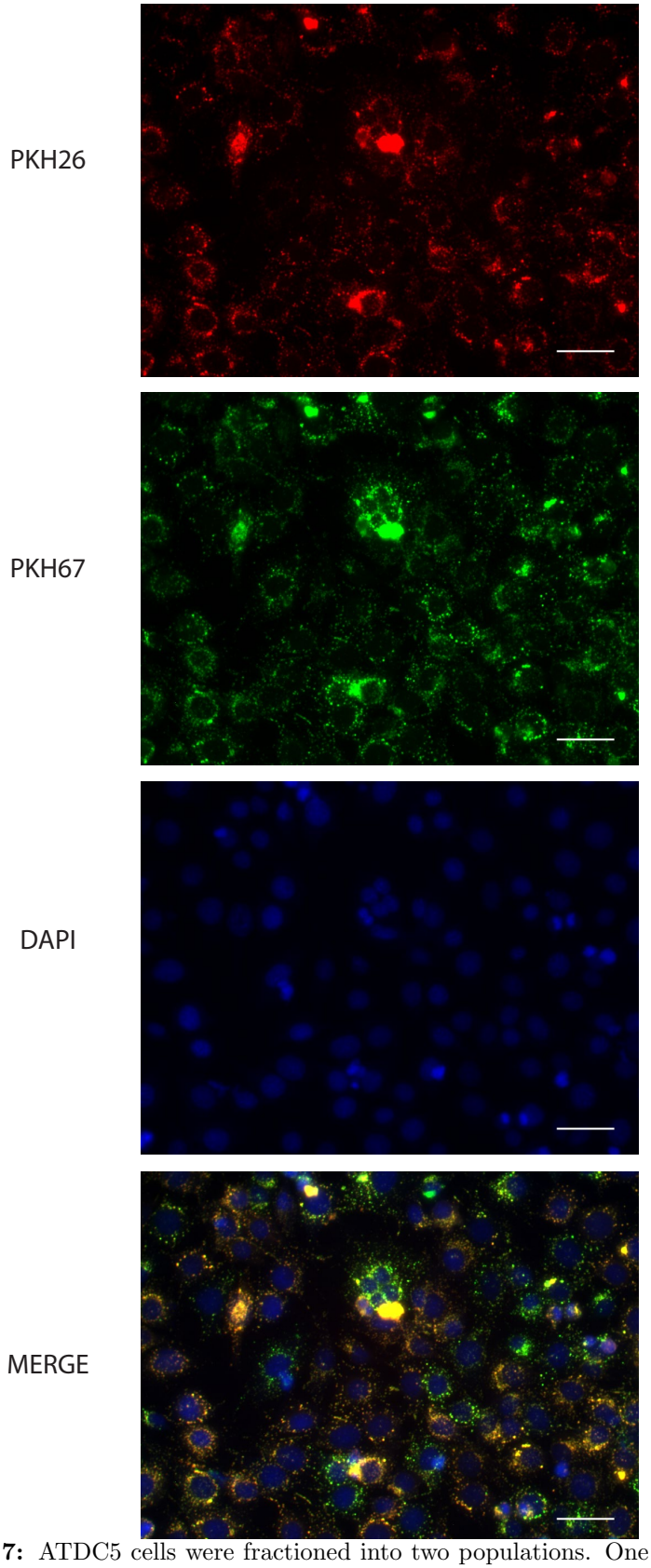

Figure 3.7: ATDC5 cells were fractioned into two populations. One population was labelled with 24 µM PKH26 and the other population was labelled with 8 µM PKH67. The populations were then mixed and plated on tissue culture plastic overnight. Subsequent imaging revealed co-localization of the two membrane probes. Scale bars = 50 µm.

3.3.3 Cell Distribution in Co-culture

To examine cell distribution in co-culture, STRO-1+ SSCs and HACs were membrane-tagged with PKH67 and PKH26, respectively, prior to co-culture set-up for 21 days. Cryo-embedded pellets were cut and imaged using a confocal microscope (Figure 3.8). Matrix staining of PKH67 was observed as well as a small degree of colour overlap between the two probes, suggesting co-localization of the HAC and SSC populations. Overall, the two cells populations were randomly distributed across the co-culture conditions. It should be noted that the matrix staining was prevalent in the SSC pellet, suggesting incorporation of the membrane probe into the matrix.

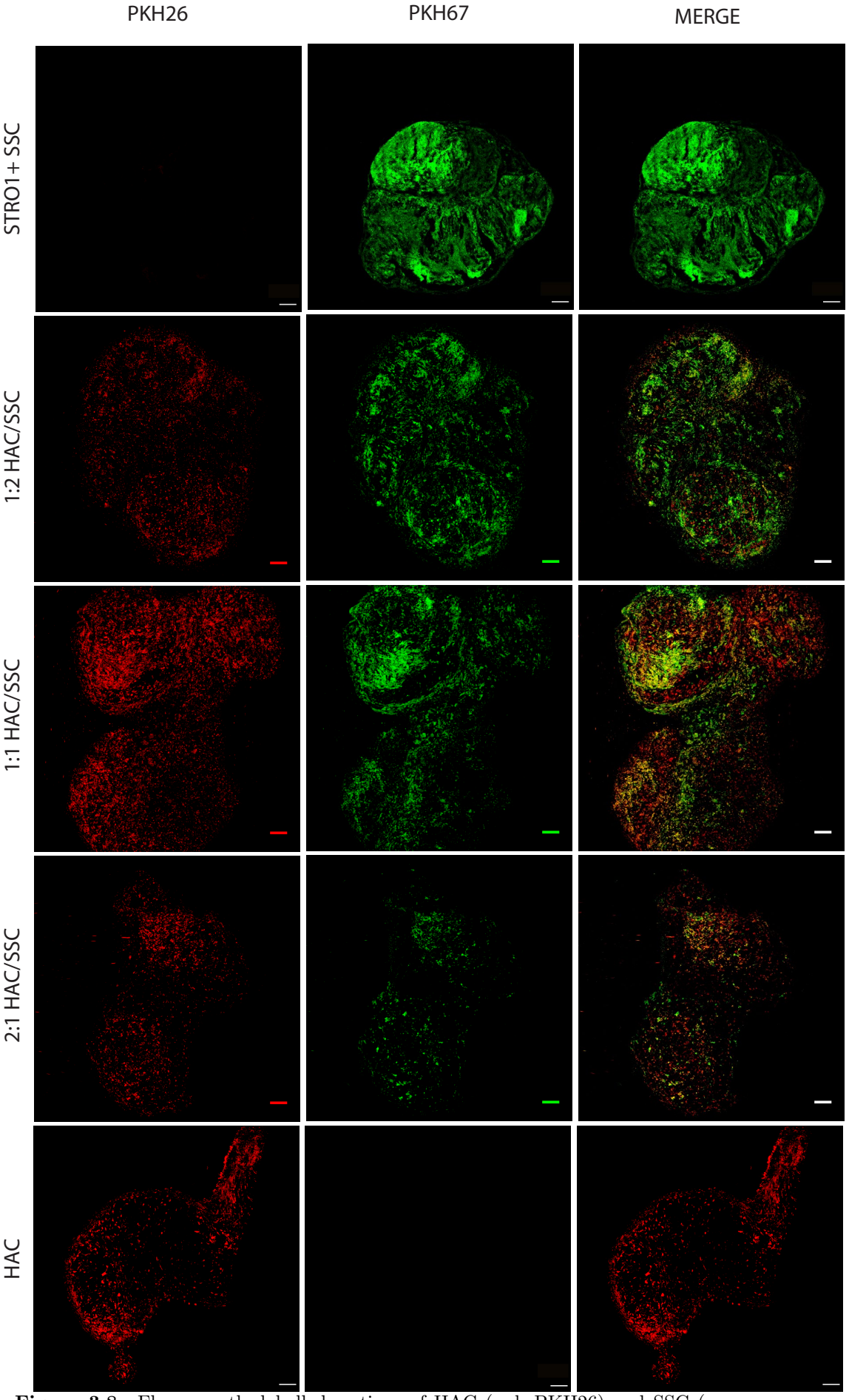

Figure 3.8: Fluorescently labelled sections of HAC (red, PKH26) and SSC (green, PKH67) co-cultures and controls. Scale bars = 100 µm.

3.3.4 Histological Analysis of Co-cultures

HACs and STRO-1+ SSCs from 3 patient samples (Figure 3.9, Figure 3.10, Figure 3.11) were used to generate co-cultures in 3D pellet cultures under normoxic conditions (21% O_2). The tissue quality of the control and experimental groups for each patient was qualitatively assessed via histology and immunohistochemistry. As the desired tissue is hyaline-like cartilage, the tested co-culture compositions were evaluated for their matrix composition of proteoglycans (Alcian blue staining) and collagen type II. The relative staining fraction for these markers were then compared against collagen type-I (negative marker for fibrocartilage) and collagen type-X (negative marker for hypertrophic cartilage). To aid the evaluation of the histological staining, Figure 3.9–Figure 3.11 include a coloured inset at the corner of each image to differentiate desired staining (green), moderate staining (yellow), and poor quality/undesired staining (red) for a particular marker.

3.3.4.1 F85 Co-culture Pellets

With respect to the F85 SSC control and co-culture pellets, the HAC control was observed to have the largest cross-sectional area. As the HAC population within the co-culture reduced, a significant reduction in the pellet cross-sectional area was noted, with the SSC biased (1/2 HAC/SSC) condition depicting an observable change in the the SSC control having the smallest size. As the SSC population within the co-culture increased, the tissue structure was also noted to be less developed, where cells were located in lacunae, and appeared more as an agglomerate of cells within a matrix structure.

Correspondingly, the HAC control pellet was noted to express the most GAG staining within the tissue matrix, with the HAC biased condition having a uniform, but less intense GAG staining. The equal mix (1/1 HAC/SSC) and SSC biased pellets expressed progressively less uniform proteoglycan staining, with GAG staining within the matrix being non-existent in the SSC control pellet. SOX9 expression was localized to chondrocytes in the HAC control and co-culture pellets, while staining was noted in cell clusters in the SSC pellet. COLI staining was noted in the matrix of all pellet conditions. Prominent staining was also observed within chondrocytes in the SSC

biased pellet. Expression of COLII was noted in both the chondrocytes and matrix, with staining throughout the structure for all culture conditions. COLX staining was found to be minimal for the HAC control, HAC biased, and equal co-culture conditions, but prominent expression was noted in the cells and matrix within the SSC biased and SSC pellet.

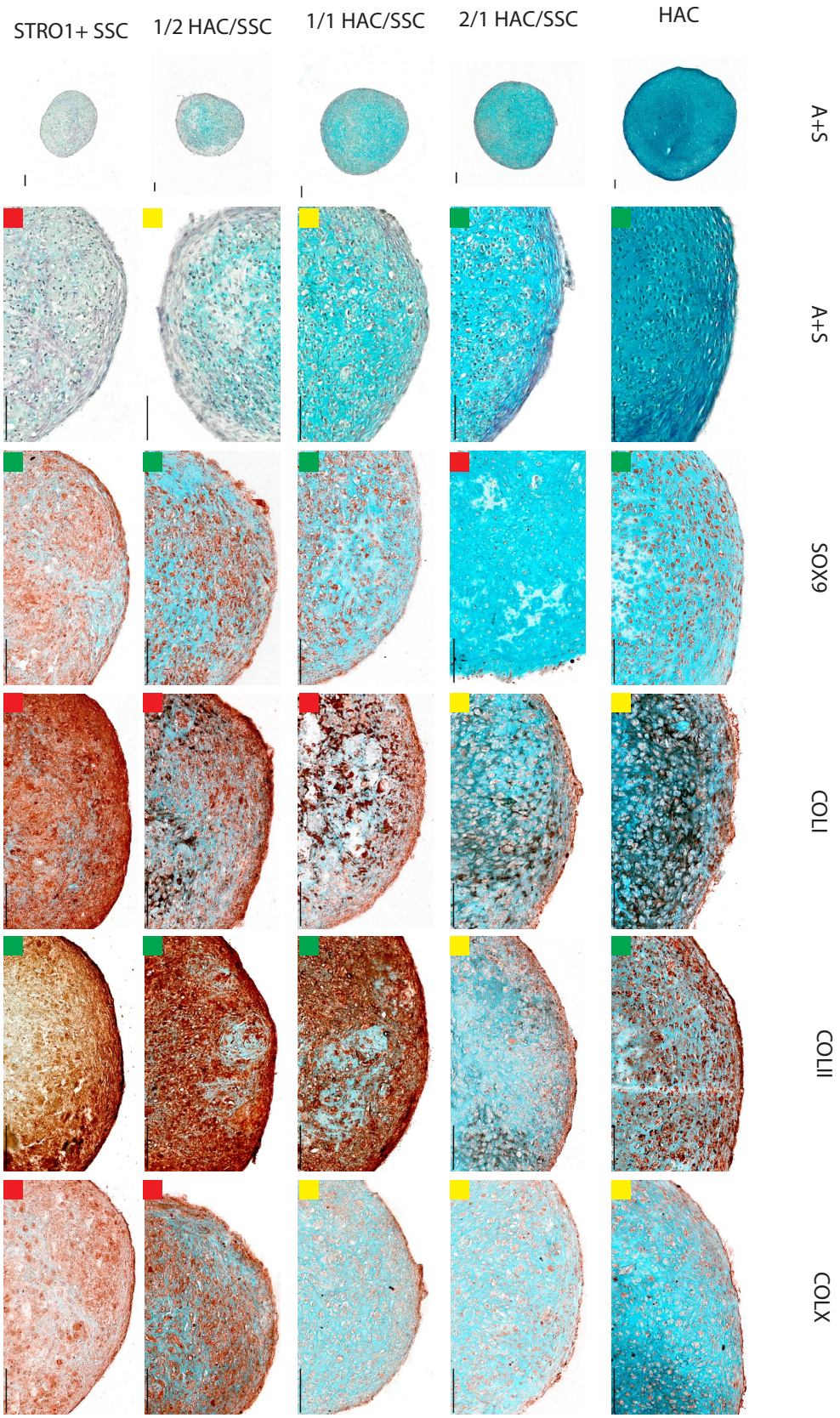

Figure 3.9: Staining results for cells harvested from F85 patient. SSCs were cultured with HACs in pellet culture in equal (1:1) and bias ratios (2:1 and 1:2 HAC/STRO-1+) for 21 days. Each high magnification image contains a colorimetric insert to ease identification of the staining (green - desired; yellow - moderate; red - undesired). While SOX9 and COLII expression was prevalent in all of the co-culture and control conditions, a marked decrease in the pellet size and proteoglycan content in the matrix was observed as the SSC fraction increased in the co-culture population and the respective control. Increased matrix deposition of COLI and COLX was also noted as the SSC fraction dominated the co-culture, suggesting a lack of hyaline-like cartilage development. Scale bars = 100 μm.

3.3.4.2 F59 Co-culture Pellets

The F59 pellets displayed a similar size and proteoglycan staining trend as the F85 constructs. The HAC control pellet expressed the most uniform matrix staining for GAGs, which was observed to decrease as SSCs formed a larger fraction of the co-culture. The HAC control and HAC biased pellets were close in cross-sectional area, with a marked reduction in construct size with the the equal mix. The SSC biased and SSC pellets were both found to lack GAG staining in the matrix and the constructs were the smallest in size for the patient set.

Similarly to patient F85, SOX9 expression was prevalent either in individual cells, or cell clusters, as is the case for the HAC biased condition. It should also be noted that SOX9 staining in the SSC biased pellet was observed to be weaker than that for other conditions. COLI staining was negligible for HAC control and HAC biased pellets. COLI expression was noted in the chondrocytes within the equal mix pellet and throughout the matrix for the SSC biased and SSC pellet. Expression of COLII was noted both in the chondrocytes and matrix, with staining throughout all pellet culture conditions. Matrix staining for COLX was found to be minimal for the HAC control, HAC biased, and SSC biased, but was found throughout the matrix for the SSC pellet. Prominent expression was noted in the cells within the equal mix, but weak cellular staining was observed in biased mixtures.

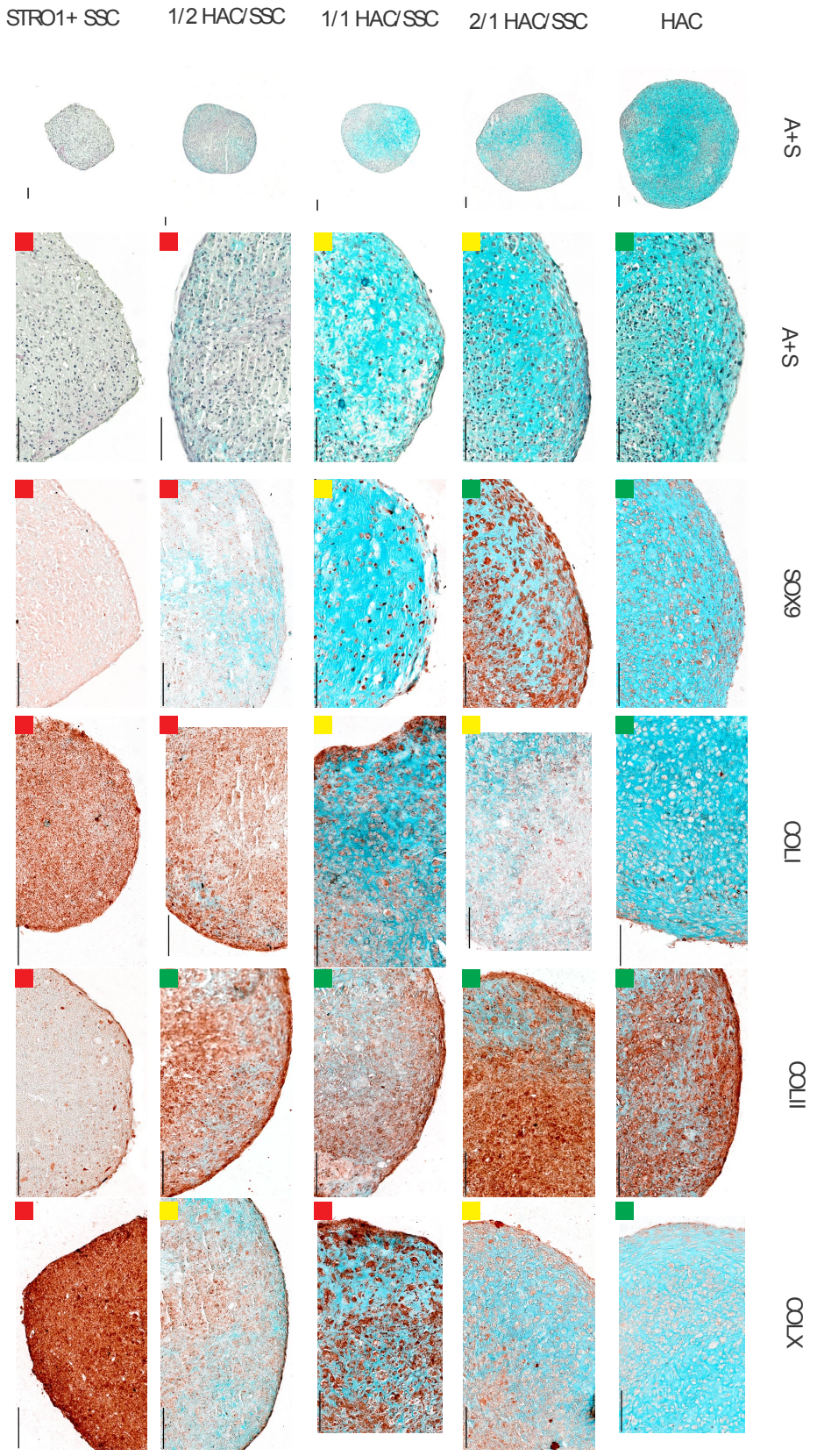

Figure 3.10: Staining results for cells harvested from F59 patient. SSCs were cultured with HACs in pellet culture in equal (1:1) and bias ratios (2:1 and 1:2 HAC/STRO-1+) for 21 days. Each high magnification image contains a colorimetric insert to ease identification of the staining (green - desired; yellow - moderate; red - undesired). Pellet size and GAG content was observed to reduce with a lower HAC fraction. Proteoglycan deposition in the matrix was nonexistent for the SSC biased and SCC control pellets, with the corresponding SOX9 staining appearing light or non-specific. Heavy COLII expression was noted for the HAC control and co-culture conditions, but noted along the periphery of the SSC control pellet. Increased matrix deposition of COLI and COLX was also noted as the SSC fraction dominated the co-culture, though more intense staining in the equal mix and SSC control. Scale bars = 100 µm.

3.3.4.3 F76 Co-culture Pellets

Unlike the previous patient sets, the F76 constructs were fragmented and exhibited abnormal structure for the HAC control and co-culture conditions, thus making size comparisons difficult. However, the SSC pellet was noted to be appreciably smaller than all other conditions. Rich GAG staining was noted in HAC control and co-culture conditions, suggesting hyaline-like cartilage formation. This deviates from the trend expressed in the F59 and F85 patient pellets. Sirius red staining was also observed within the core of the SSC pellet with GAG staining around the periphery of the pellet. SOX9 expression was noted in all culture conditions, however, to a weaker extent than the previous patients. COLI staining was minimal for HAC control and co-culture pellets and localized to the periphery of the pellets. COLI expression was noted in the chondrocytes within the equal mix pellet and throughout the matrix for the SSC biased and SSC pellet and correlates well with the Sirius Red staining along the periphery. Expression of COLII was noted in both the chondrocytes and matrix, with staining throughout all pellet culture conditions with the SSC pellet displaying the most prominent staining. COLX staining was found to be minimal for the HAC control and HAC biased pellets, but prominent expression was noted in the cells within the equal mix and SSC biased pellets and through the matrix for the SSC pellet.

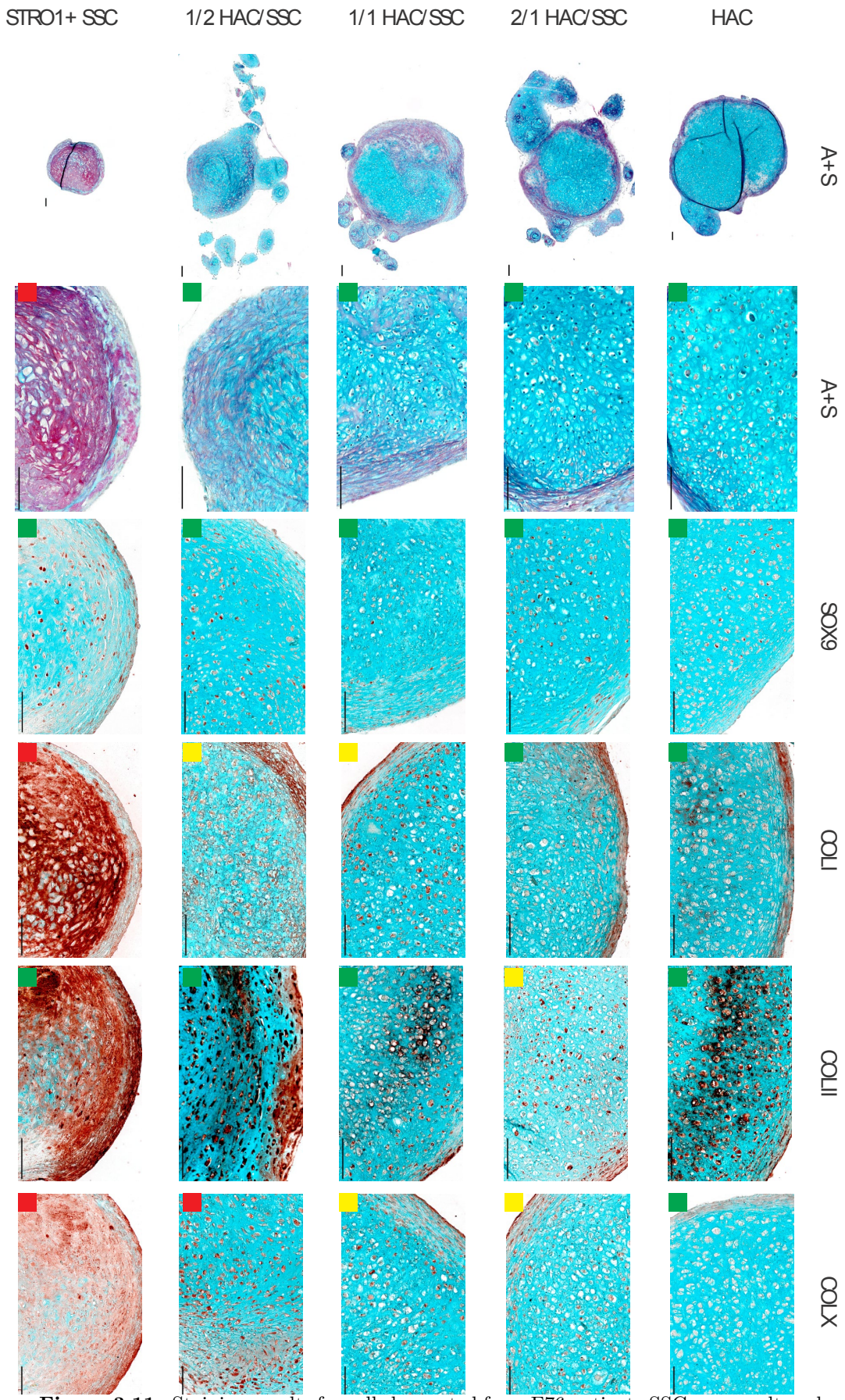

Figure 3.11: Staining results for cells harvested from F76 patient. SSCs were cultured with HACs in pellet culture in equal (1:1) and bias ratios (2:1 and 1:2 HAC/STRO-1+) for 21 days. Each high magnification image contains a colorimetric insert to ease identification of the staining (green - desired; yellow - moderate; red - undesired). Pellets were observed to be more fragmented, though the SSC control was noted to be most spheroidal and smallest in size. GAG content was noted in all culture conditions, but mixed heavily with Sirius Red staining for the SSC control, indicating high fibular

3.3.5 Image Analysis of Co-culture Pellets

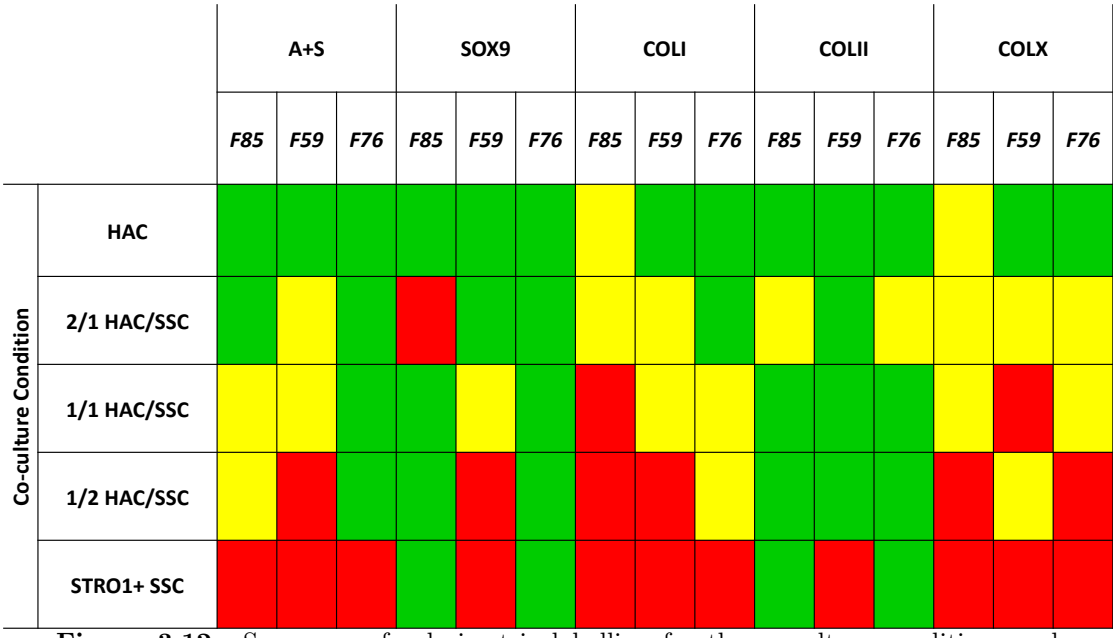

Figure 3.12: Summary of colorimetric labelling for the co-culture conditions and respective staining for the three assessed patients.

Figure 3.12 presents a summary of the labelled inserts for a given co-culture pellet and staining. While COLII and SOX9 was expressed in every patient, for each co-culture condition, the relative expression of COLI and COLX staining to the COLII staining suggests that the HAC bias and pure conditions consistently generated more hyaline-like cartilage compared to the equal mix, SSC bias and SSC only control conditions. Considering the subjective nature of histological assessment, however, the staining data was further processed through a cluster analysis image segmentation algorithm to provide a semi-quantitative measure of the matrix composition, specifically to provide a comparison of the pellet size, proteoglycan content, and collagen content in each of the co-culture conditions.

3.3.5.1 Validation of Image Analysis Algorithm

The image analysis method used was validated through manual analysis of the binary images created from the source RGB images.

Due to the variation in staining intensity present between the different co-culture conditions, three images of high, intermediate, and sparse staining were used to

validate the algorithm robustness for quantifying the immunohistochemical staining (Figure 3.13) and proteoglycan content (Figure 3.14). From the test set, it was observed that the algorithm was able to identify the high intensity staining boundaries and differentiate those areas to the counter staining, as indicated by the binary images in Figure 3.13C and Figure 3.14C, where the counter staining was omitted from the isolated target staining and binary image. Total area calculation was accomplished through binarization of the background channel, where the pixel intensities were given to be the more neutral. In the case of the A/S images, the blue channel was used as the channel expressed no significant colour variation (Figure 3.14; Background Channel). It was noted, however, that some artefacts were present in both the target and background binary (Figure 3.13C-D), which is likely a result of dust particulates and other matter present during imaging. Given this, the image segmentation algorithm was found to be effective in isolating the positive staining from the pellet (blue proteoglycan staining and red IHC staining for collagen), but complete isolation of the background is necessary to reduce the segmentation error. The next section, therefore, describes the staining segmentation following separation of the background from the foreground.

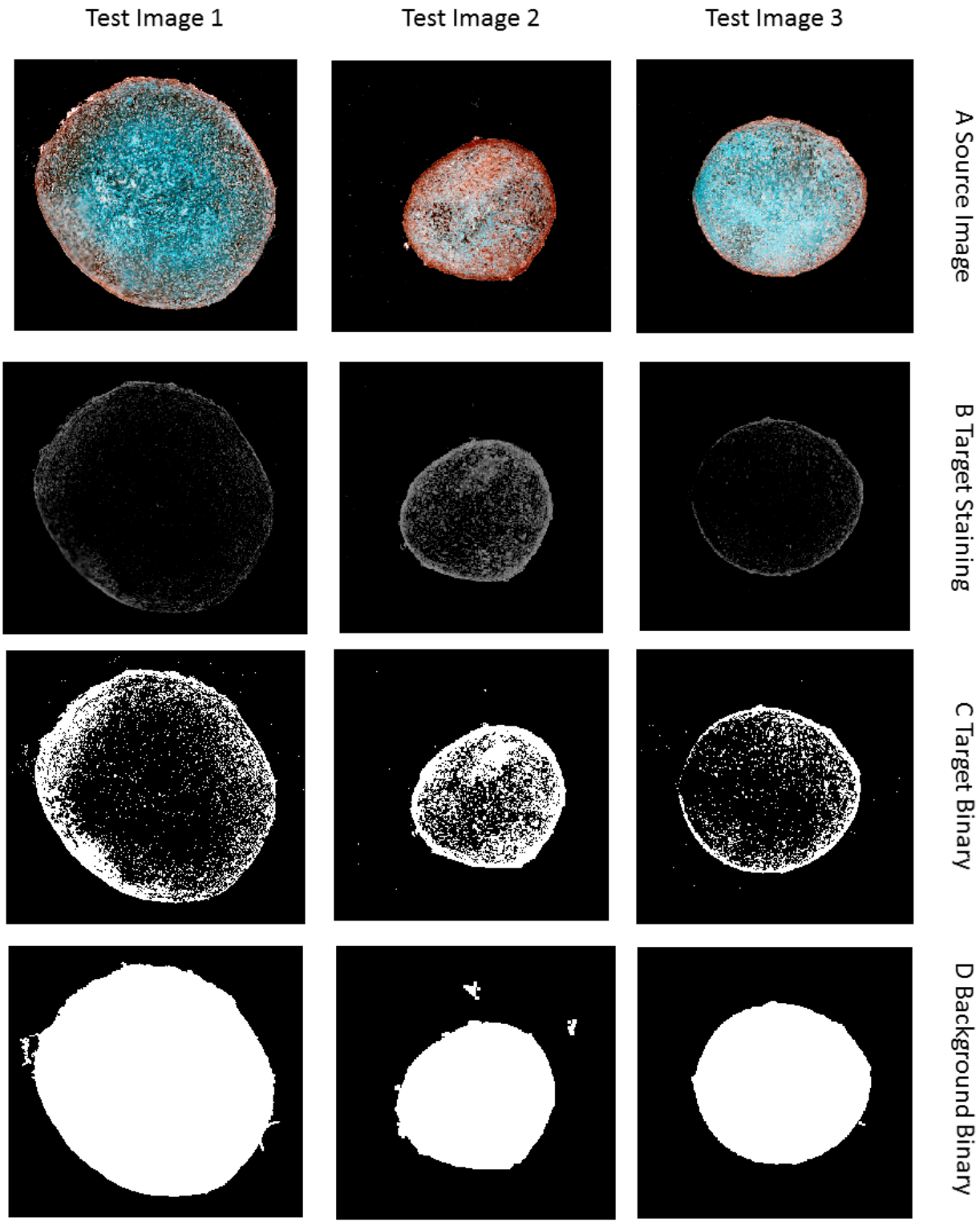

Figure 3.13: Validation of image analysis script for effective segmentation of collagen staining. Three test images were used to validate the algorithm's ability to identify collagen within the matrix and cells.

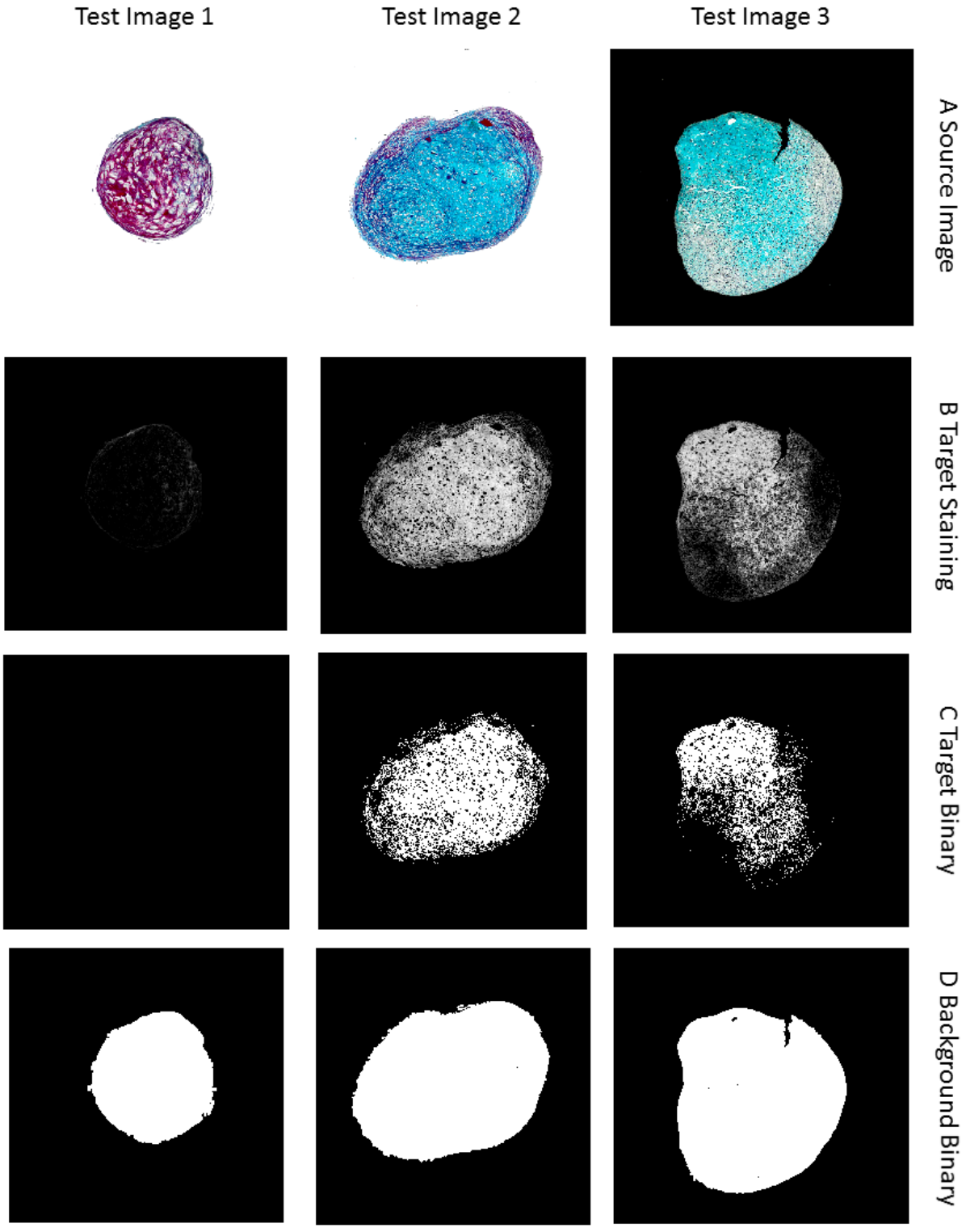

Figure 3.14: Validation of image analysis script for effective segmentation of proteoglycan staining. Three test images were used to validate the algorithm's ability to identify GAG rich zones within the section and isolate the collagen and fibrocartilage-like staining areas.

3.3.5.2 Co-Culture Pellet Composition and Size by Image Segmentation

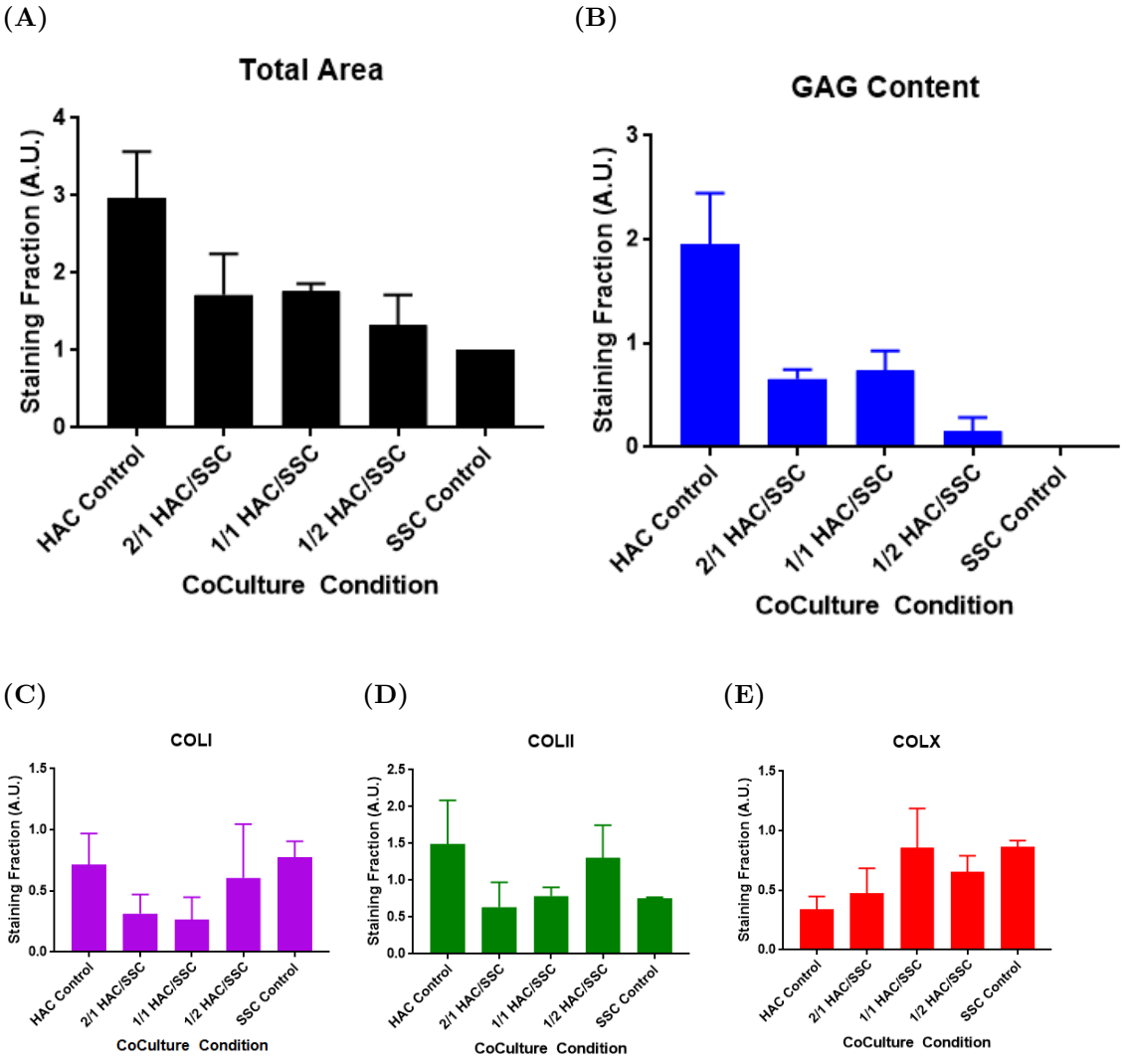

Figure 3.15: (A) Computed total area of whole co-culture sections. Area values were normalized to HAC control area for each patient to minimize size variation between patients. Co-culture pellets did not show a significant change in size relative to HAC although SSC biased pellets were consistently smaller. (B) Comparison of GAG staining area for co-culture pellets. Staining area was normalized to the total section area to determine the compositional fraction for each culture condition. (C) Comparison of collagen type I staining area for co-culture pellets. Staining area was normalized to the total section area to determine the compositional fraction for each culture condition. (D) Comparison of collagen type II staining area for co-culture pellets. Staining area was normalized to the total section area to determine the compositional fraction for each culture condition. (E) Comparison of collagen type X staining area for co-culture pellets. Staining area was normalized to the total section area to determine the compositional fraction for each culture condition. (n = 3, $\bar{x} + SEM$)

The total area computations from the script were normalized against the HAC control to better represent the size difference between the culture conditions (Figure 3.15A).

Given the inherent variability in primary cells, accompanied by the obvious size different between the co-culture conditions, it is difficult to provide a comparative, statistical analysis of the matrix composition for the different co-culture conditions. Despite this, the patient sets examined via image analysis indicate a trend for all measured staining conditions, which supports the histological observations reported for the individual patient sets.

A significant size variation was noted with the pellet constructs, where HAC pellets were computed to be on average five times larger in area than the SSC pellets. The HAC-biased and equal mix co-culture pellets were similar in size, while the SSC biased pellets were noted to be smaller, on average. The co-culture constructs were also quantitatively assessed for proteoglycan and collagen positive staining fraction. GAG staining (Figure 3.15B) was detrimentally reduced as the SSCs formed a larger fraction of the population. Correspondingly, COLX (Figure 3.15E) and COLI (Figure 3.15C) staining formed a larger fraction of the matrix as the SSC population in the co-culture increased. COLII staining (Figure 3.15D) did not indicate an obvious pattern, however, it was noted that the HAC control and SSC biased constructs induced the highest positive staining for COLII.

3.4 Discussion

Chondrocytes have been viewed as the obvious cell source for cartilage repair as they are native to articular cartilage. Unfortunately, the cells have a tendency to de-differentiate *in vitro*, thus losing their chondrocyte phenotype [216]. Additionally, the cells also exhibit a low proliferation rate in monolayer, which further limits their application [217]. Mesenchymal stem cells have been viewed as an alternative source of cells for cartilage development. As MSCs can be harvested from a variety of sources, such as adipose tissue and the bone marrow stroma, the articular cartilage can be left intact, reducing potential for additional trauma to the area. Previously, our group has assessed the chondrogenic potential of HACs and STRO-1+ SSCs from the same patient [225]. This was accomplished both through scaffold-free pellet culture as well as cell-seeded membrane scaffolds using Alvatex. It was found that HACs possessed excellent chondrogenic potential in both pellet culture and scaffolds. In contrast, the STRO-1+ SSCs expresses a phenotypic drift towards hypertrophy in both culture situations.

While the chondrogenic potential of STRO-1+ SSCs is limited, it has been reported that co-culture of MSCs with chondrocytes may promote chondrogenesis and assist cartilage development [228, 232, 233]. Unfortunately, literature presents conflicting results as to whether co-culture of stem cells and chondrocytes is beneficial, as a result of cells potentially influenced by biomaterials, dissimilar sources of stem cells and chondrocytes, and heavily biased co-culture ratios [218–221].

This study attempted to address the variability found in co-culture studies by using scaffold-free pellet culture, a technique used for simple generation of cartilage models [204, 225]. Furthermore, primary HACs and STRO-1+ SSCs from the same patients were co-cultured in ratios of 1:1, 1:2, and 2:1 within 3D pellet culture for 21 days under normoxic conditions. The resulting tissue was analysed by histology and image segmentation to determine the interactions between STRO-1+ SSCs and HACs and provide insight to engineering robust cartilage within the acoustofluidic bioreactor.

The pellets were cultured for 21 days prior to histological staining. Co-culture, HAC control, and STRO-1+ SSC pellets for each patient manage to form cartilaginous tissue based on the A/S staining. Fluorescent labelling of the two cell populations

prior to culture also revealed that cells did not reorient themselves within culture and maintained a random distribution. Generally, a higher ratio of stem cells resulted in minimal GAG formation and high expression of COLI and COLX, which would suggest that the STRO-1+ SSCs differentiated to generate hypertrophic or fibrocartilage, rather than hyaline-like cartilage. The addition of HACs to the co-culture population demonstrated a reduction in COLX and COLI staining, as well as increasing GAG expression within the matrix. Overall, histological analysis suggest that the HAC bias co-culture condition best limited COLX production whilst showing comparable cartilage development to the HAC control. The image segmentation results further supports this claim.

As the primary aim of this study was to determine an optimal cell source for use in the bioreactor, further work within this thesis will utilize HACs within the bioreactor as the HAC control constructs consistently expressed the most robust staining and the largest construct size. This said, future work to enhance HAC/SSC co-culture can focus on the role of the culture environment for the cells. While the mechanisms behind co-culture induced chondrogenic development are not well known [227], Giovannini *et al.* [232] suggest that co-culture conditions, patient age, and other factors may affect cartilage quality *in vitro*. Their study showed that MSCs did not express chondrogenic markers in micromass culture without the addition of chondrogenic factors, such as TGF-β and dexamethasone. In the presence of TGF-β and dexamethasone, MSC pellets expressed cartilage-specific matrix, but also exhibited high expression of collagen type X and alkaline phosphatase [232]. Additionally, gene expression analysis of aggrecan also exhibited that the MSCs did not contribute to proteoglycan deposition in the co-culture pellets.

Furthermore, it is known that articular cartilage has low oxygen tension [28, 197] and that chondrocytes cultured in hypoxic conditions maintain their phenotype more effectively than in normoxia [28]. changes to the culture environment would result in secretion of chemical factors by the cells, which may further aid in cell-cell interactions and effective production of cartilage. Current literature has shown that mechanical stimulation of chondrocytes results in the secretion of parathyroid hormone-related protein (PTHrP), a chemical factor has been found to aid chondrogenesis and reduce hypertrophy [228, 234, 235]. Fischer *et al.* has also shown that controlled interaction between cells and PTHrP can more precisely affect their chondrogenic potential [236].

The subsequent chapters will therefore investigate the role that the chemical environment plays in addition to the potential mechanical stimulation from the acoustic environment, bioreactor culture will be supplemented with PTHrP.

Chapter 4

Design and Characterization of a High-Throughput Acoustofluidic Bioreactor Platform

4.1 Introduction

Tissue engineering aims to repair, replace, maintain, or enhance native, host tissue [4, 5]. These goals are typically accomplished through the use of *in vitro* culture of cells, supported by the application of appropriate growth factors, scaffolds, and bioreactor system to generate a tissue structure for the eventual implantation into patients. To date, several groups have shown promising results in developing various tissue structures, such as bone [6, 7, 237–241] and cartilage [6, 9, 22, 225, 242]. In the case of cartilage engineering, it is possible to generate the tissue from a variety of modalities—from deposition printers [10, 243, 244] to micro-scale bioreactors [11] and stackable cell sheets [12, 13].

Previously, our group has presented the application of acoustofluidics for tissue engineering cartilage [22]. In this study, it was suggested that robust tissue development occurred as a result of the acoustic field maintaining the cells as a levitated structure and peristaltic perfusion aided the system to allow for nutrient exchange and fluid shear-based stimulation to the cells. The research further suggested that cycling through a range of frequencies resulted in oscillatory motion on the cells,

though this was not explored in detail. Furthermore, certain design flaws with this acoustofluidic system limited its practicality and reliability in generating hyaline-like cartilage constructs. Specifically, the microcapillary tube design would accommodate one construct to be generated at a time. Given the nature of the patient-derived cells, significant variability in tissue structure may be prevalent and more time would be required to generate a requisite number of samples to analyse. Additionally, bubble generation within the media reservoir was an occurring problem, which led to perfusion and trapping of bubbles during culture. The surface tension between air/media interface within the fluid layer would result in removal of the developing tissue from the trap and result in a failed culture. To this end, a new bioreactor design would be necessary to ensure high throughput and successful tissue development, as well as allowing characterization of the acoustic force interaction with the cells and developing tissue.

The primary aims for the new bioreactor design are to improve both the throughput and efficiency of the platform in generating cartilage constructs. Higher throughput would be achieved by running multiple resonators in parallel, while efficiency is linked to the cell trapping and viability within the pressure node. To this end, this chapter presents designs that moved away from closed, capillary tubes in favour of a more open resonator design to limit bubble perfusion and interaction within the fluid layer of the resonator. The open designs presented in this chapter show resonators immersed in the culture media, limiting the effect of fluid shear from peristalic media exchange. This design choice is intended as it would allow for more control over physico-chemical factors, including the acoustic environment to provide, not only biomechanical stimulation to the cells, but also allow nutrient flow via acoustic streaming, which will be discussed in the next chapter. In this chapter, I present my initial findings for the design and characterization of a next generation acoustofluidic bioreactor, including how the efficiency of the resonators and heat transfer from the transducer to the culture environment changes with continuous use.

4.2 Materials and Methods

4.2.1 Cutting Piezoelectric Transducers to Shape

Piezoelectric transducers (Ferroperm PZ26, Kvistgaard, Denmark; 50 X 25 X 1 mm; PZT) were cut to 10 mm x 12 mm x 1 mm using a 0.4 mm diamond wheel saw (M1D15, Struers ApS, Denmark) on a macrotome driven at 4000 RPM and a feed rate of 0.040 mm/s. The edges of the transducers were ground using 1000 grit sandpaper to remove defects from the cutting process. The electrode on one face was also sectioned and bridged with the underlying electrode using silver conductive paint (Electrolube SCP03G). The bridging allowed for wiring of the PZT on a single face to minimize the thickness of the coupling/adhesive layer and simplify assembly of the resonator.

The finished transducers were then coupled to the carrier layer in accordance to one of the two design layouts discussed in this chapter.

4.2.2 Design 1: Wellplate-based Bioreactor Manifold Fabrication

A computer aided design model of the assembled manifold is given in Figure 4.1. The manifold design consisted of a reflector layer (75 mm x 50 mm x 1 mm glass slide, Corning), compartments for the devices (device well) and for excess medium to collect (overflow well). The manifold assembly consisted of three substructures: the bottom plate, main plate, and lid plate. The bottom plate functions to incorporate the reflector as a built-in component of the assembly. The main plate structure separated the overflow well from the device well to ensure constant fluid levels in the device wells. The lid plate incorporated fluidic fittings to allow medium exchange. The final manifold assembly was machined in-house from polycarbonate (Aquarius Plastics) sheets. To prevent leakage through the manifold sheets, poly(dimethyl siloxane) (PDMS, Dow Chemical Sylgard 182 1:10 curing agent:monomer) functioned as a gasket by curing between each sheet at 80°C for 1 hour.

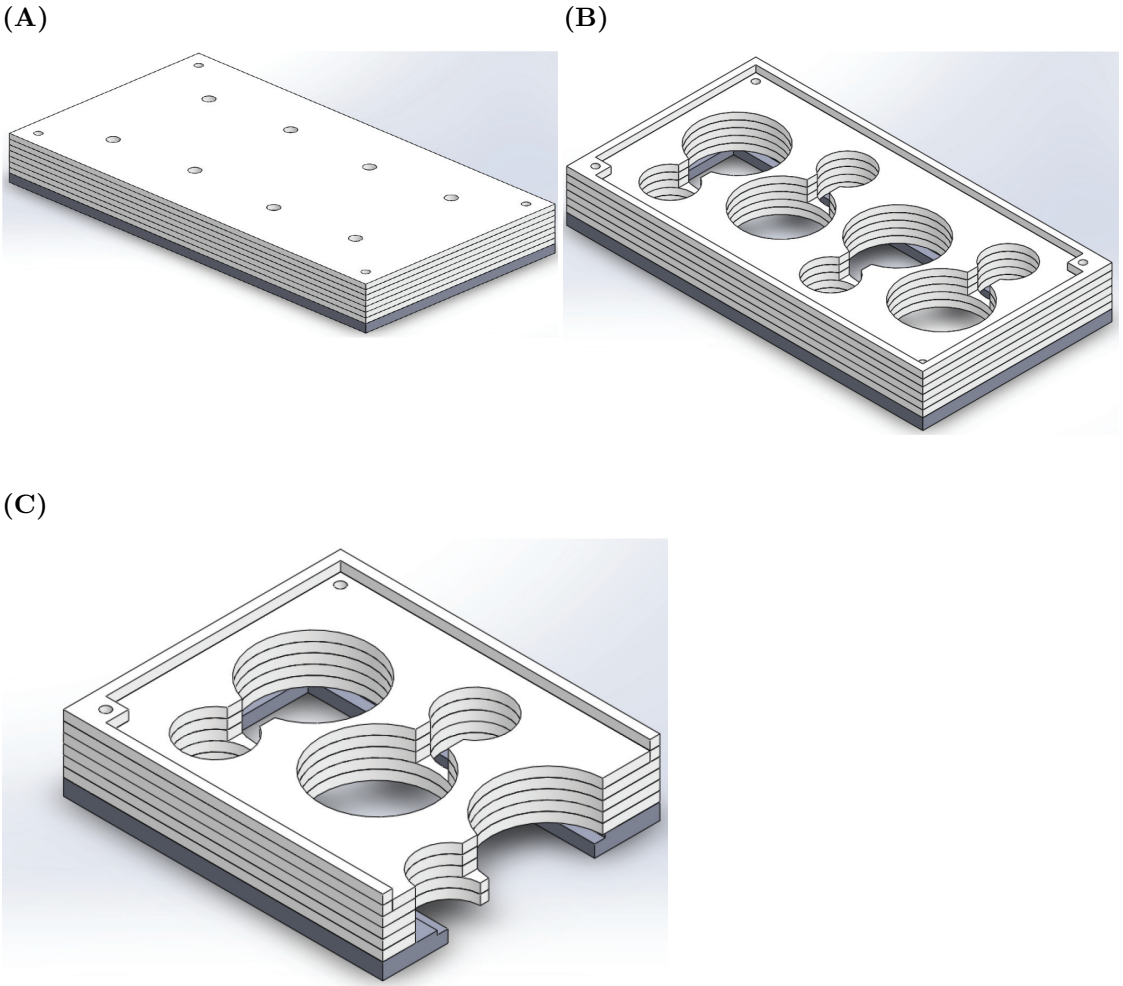

Figure 4.1: Computer-aided design models in Solidworks of the manifold assembly (A) with and (B) without the lid. (C) A cross-sectional view of one of the wells illustrates the separation between the well housing the device and the overflow well for the excess media.

The layered resonators used in this bioreactor system were custom-built devices. The base piece and rings were machined from 3 mm thick sheets of ceramic (Macor). Base pieces were machined so that the fluid layer for the assembled device would be 200 μm (thin device, Figure 4.2A). The base piece of each device functioned as the carrier layer where a PZT transducer (PZ26, Figure 4.2Ai) and two magnets were adhered to it using an epoxy (Epotek 301 4:1, RS) cured at 80°C for 1 hour. A mirror (Edmund Optics 31418) was also fixed to the underside of the base to enhance image contrast (Figure 4.2Aii).

Ribbon cables were then soldered onto the transducer to transmit the driving voltage and frequency from a function generator. A glass microscope slide (50x75x1 mm,

Corning) functioned as the reflector later and an M12 metal washer was used to magnetically clamp the device onto the reflector.

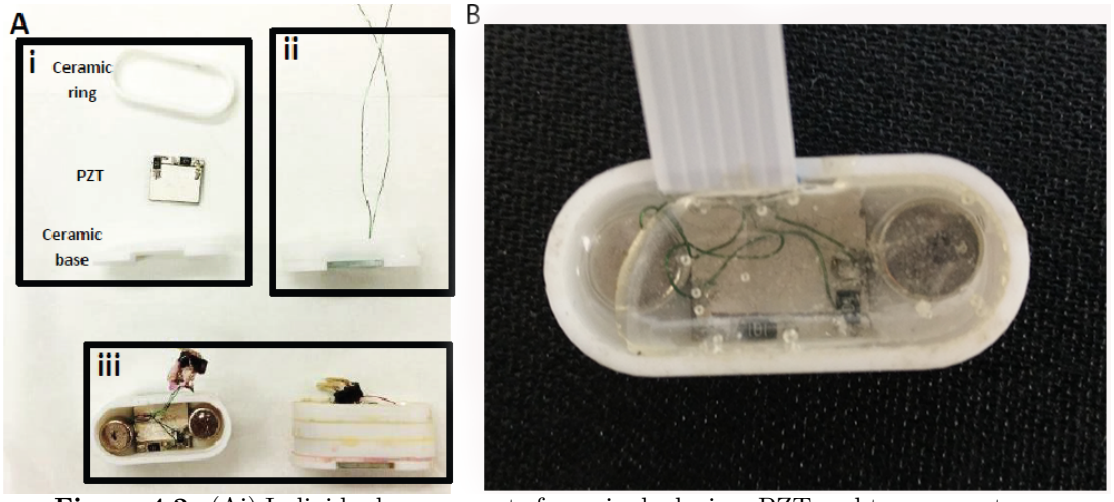

Figure 4.2: (Ai) Individual components for a single device. PZT and two magnets are adhered to ceramic base with a thin epoxy layer. Ceramic rings were glued onto the base and stacked to increase height of device. (ii) Side view of partially finished device with wires soldered to PZT. (iii) Top and side view of completed device. (B) Top view of assembled device with PDMS sealing.

To enhance the robustness of the devices, PDMS was cured inside the cavity of each device in order to better protect the transducer from corrosion (Figure 4.2B). Epoxy was then cured on top of the silicone to further seal the device.

4.2.3 Design 2: Inverted Bioreactor Assembly

(A)

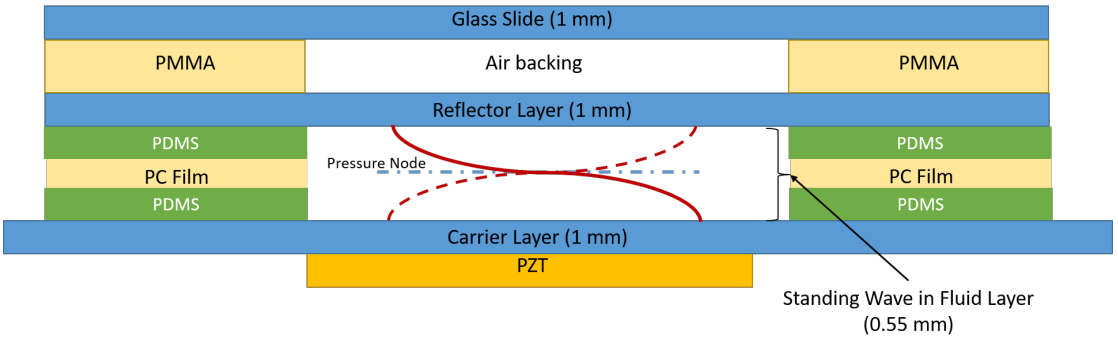

(B) **(C)**

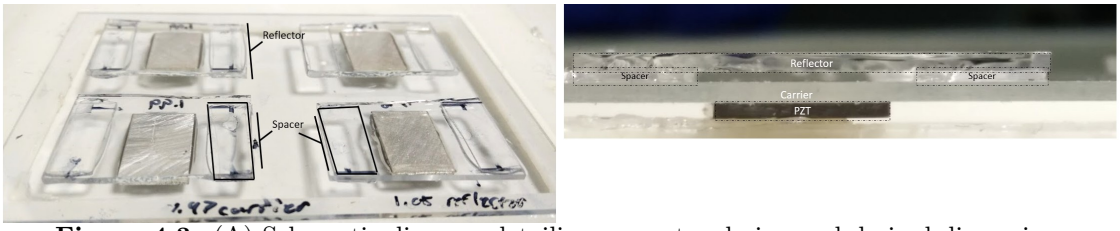

Figure 4.3: (A) Schematic diagram detailing resonator design and desired dimension of each layer. (B) Side view of assembled resonator, labelled to indicate position of PZT, spacers, carrier and reflector layer. (C) Angled top view of assembled plate to detail arrangement of multiple resonators on a single double-width glass slide.

A schematic of the resonator design is depicted in Figure 4.3A. To assemble the resonators, double-width glass slides (Corning, 75 x 50 x 1 mm) and standard microscope slides (Corning, 75 x 25 x 1 mm) were acid cleaned in a 6M HCl solution for 3 hours. Double-width slides were washed in distilled water before adhesion with piezoelectric transducers (Ferroperm PZ26, Kvistgaard, Denmark; 10 X 12 X 1 mm) with epoxy (Epoxy 353, Epotek, Billerica, MA, USA) at 80°C for 1 hour. Four transducers were adhered to each slide, which functioned as the carrier layer (Figure 4.3B). Microscope slides were cut to 13 x 25 x 1 mm to function as the reflector layer for the resonators. Polycarbonate film (500 micron Lexan, Cadillac Plastics) functioned as a spacer between the carrier and reflector and sealed using PDMS. Figure 4.3C depicts the assembled resonator.

Polypropylene (5 millimetre, Aquarius Plastics) was cut to shape using a laser cutter and 1 mm grooves were introduced into the top and bottom sheets using a micro-mill to fit the bioreactor plate and create a sealed environment to maintain a sterile culture environment. For the purposes of long-term tissue culture, a custom cut poly(methyl methacrylate) (PMMA) spacer functioned as a spacer to maintain an air backing

behind the reflector layer. This was used to minimize fluid interaction behind the reflector layer and maintain the acoustic properties of the ultrasonic wave field.

4.2.4 Signal Generator

To reduce the footprint of the electrical driving assembly for the resonators, an Arduino microcontroller was programmed to linearly step through a frequency range for a given sweep repetition rate. The microcontroller transmitted the driving frequencies to a DDS board (Figure 4.4A, B), which generated a sine function for the frequency range program. The output voltage from the DDS board was amplified through a LT1210 amplifier (Linear Technology LT1210) with a variable inverting feedback loop Figure 4.4C), in order to adjust the final driving voltage into the resonators.

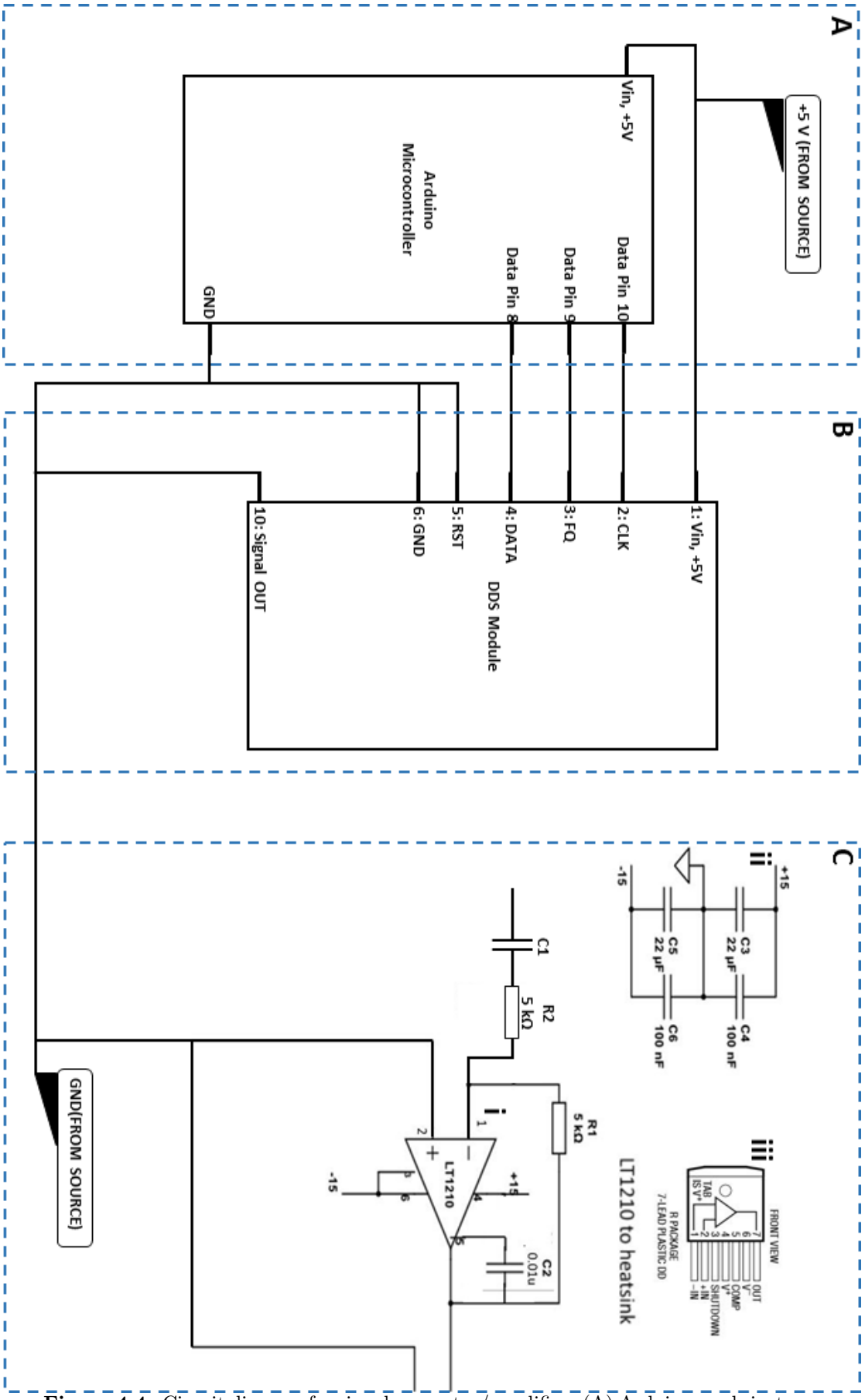

Figure 4.4: Circuit diagram for signal generator/amplifier. (A) Arduino sends instructions to the (B) DDS module to generate the driving frequency function. The output from the DDS board is then amplified through (C) a variable inverting operational amplifier prior to transmission to resonators. (Ci) The numbering pattern around the amplifier symbol correspond to (Cii) the pin connections on the physical unit. (Ciii) Given the higher voltage requirements of the amplifier, relative to the rest of the circuit, the unit was integrated into a buffer circuit as suggested by the manufacturer.

4.2.5 Resonant Frequency Characterization

A 1-D transfer impedance model in MATLAB [245] was used to guide design and predict the acoustic pressure node configuration and resonant frequency of the system . The physical and material parameters of the assorted layers were entered into the script user interface (Table 4.1), from which the acoustic energy density within the system was simulated across a range of frequencies to estimate the cavity resonance frequency. At this characteristic resonance, an acoustic pressure wave was simulated through each layer to identify the position of the nodes and antinodes to better estimate the potential and practicality of the proposed resonator design.

Parameter name	**Value/Expression**	**Units**
Fluid Layer Thickness	550, 300	µm
Carrier/Reflector Layer Thickness	1000, 1100	µm
Piezoelectric Transducer Thickness	1000	µm
Adhesive Layer Thickness	1	µm
Density of Carrier and Reflector Layer Material	2500	$\frac{kg}{m^3}$
Density of Fluid Layer Material	1000	$\frac{kg}{m^3}$
Density of Adhesive Layer	1080	$\frac{kg}{m^3}$
Speed of Sound Through Adhesive Layer	2640	$\frac{m}{s}$
Speed of Sound Through Carrier and Reflector Layer	5872	$\frac{m}{s}$
Speed of Sound Through Fluid Layer	1540	$\frac{m}{s}$
Driving Voltage	10	Vpp
Q-factor of layers	100	—

Table 4.1: Table of parameters for 1D transfer impedance model.

Following this, each resonator was connected to a conductance analyser (Cyphergraph) to measure the resonant frequency of the device in air and water. The resonant frequencies of each device was recorded before and after PDMS seal as well as after 3 weeks of culture to determine wear on devices.

4.2.6 Finite Element Modelling

A 2D finite element model based in COMSOL multiphysics was used to produce the acoustic kinetic energy distribution. The model included piezoelectric coupling and pressure acoustics within the fluid layer, with sufficient mesh density that the fluid layer mesh was 16 elements thick (Table 4.3). The acoustic radiation force was calculated using the Gorkov equation [246] across a range of frequencies, enabling the resonant frequency to be identified.

Parameter name	Value/Expression	Units
Fluid Layer Thickness	Design 1: 200; Design 2: 550	µm
Carrier/Reflector/PZT dimensions (width x thickness)	10 x 1	mm
Speed of Sound in Fluid Layer	1540	m/s

Table 4.3: Table of parameters for 2D resonator model.

4.2.7 Acoustic Pressure Amplitude Characterization

Given the linear relationship between the acoustic pressure amplitude and driving voltage, a voltage drop study was accomplished to determine the minimum pressure to keep a particle in levitation within the trap. 10 µm latex beads were levitated within a half wave node configuration with a continuously applied starting voltage of 12 Vpp. The beads were visualized near the centre of each device to limit inconsistencies between measurements and ensure maximum interaction with the acoustic beam. The voltage was reduced every 10 minutes until the beads dropped out of the trap. The minimum voltage required to keeps the beads levitated is given to be the drop voltage (V_{drop}). The acoustic contrast factor (Equation 4.1b) and energy density (Equation 4.1c) was determined by the physical characteristics of the fluid and microbeads. From this, the pressure amplitude at the drop voltage was evaluated

(Equation 4.1d) and set as a proportion to determine the acoustic pressure amplitude at any given voltage (Equation 4.1e).

$$F_g = a^3 * g * (\rho_{bead} - \rho_{water}) \tag{4.1a}$$

$$\Phi = \frac{\rho_{bead} + \frac{2}{3} * (\rho_{bead} - \rho_{water})}{2 * \rho_{bead} + \rho_{water}} - \frac{\beta_{bead}}{3 * \beta_{water}} \tag{4.1b}$$

$$\epsilon_{drop} = \frac{F_g}{4 * \pi * k * a^3 * \Phi} \tag{4.1c}$$

$$P_{drop} = \sqrt{4 * \rho_{bead} * c_o^2 * \epsilon_{drop}} \tag{4.1d}$$

$$P_{desired} = P_{drop} * \frac{V_{desired}}{V_{drop}} \tag{4.1e}$$

4.2.8 Heat Transfer

To quantify heat transfer from the transducer to the fluid layer and surrounding fluid, resonators were evaluated for fluid heating using a thermocouple, where the system was placed at ambient temperature and within a cell culture incubator (35–37°C). The bulk fluid temperature was allowed to stabilize overnight within the cell culture incubator prior to acquiring the temperature measurements. Temperature measurements were taken every 24 hours following activation of the transducer. A range of voltages were driven into the devices to quantify heat transfer and were further compared in used and freshly made devices.

4.3 Results

4.3.1 Design 1: Multiwell Bioreactor

The bioreactor was split into two subcomponents: the wellplate (manifold) and the acoustic devices. To combat the issue of bubbles within the system, the bioreactor was redesigned to be more open, such that resonators were immersed in media within the well (Figure 4.5A). Each well contained a glass slide, which functioned as a reflector layer, and a steel washer was used to magnetically clamp the device onto the reflector (Figure 4.5B). 3 mL of medium was added to each well to adequately submerge the active area of the device and to allow cell levitation and nutrient transfer.

(A)

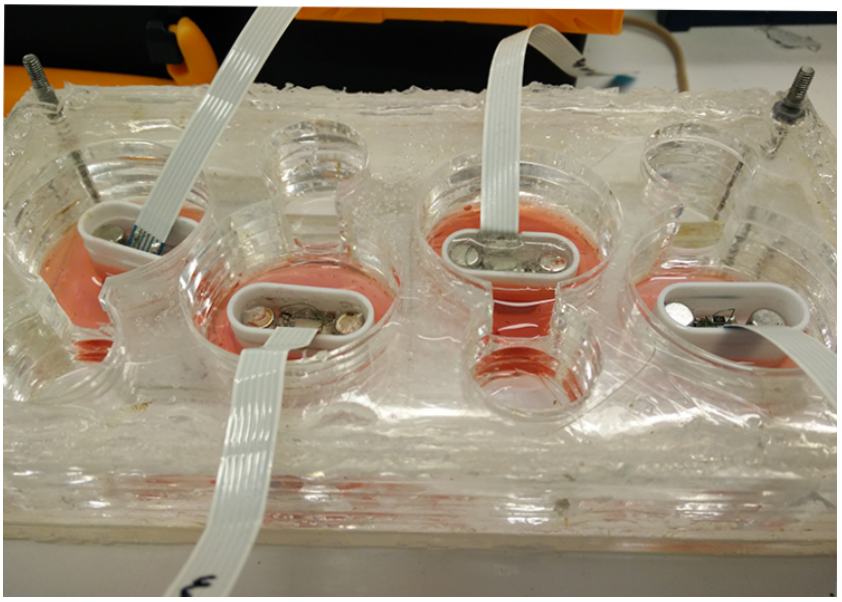

(B)

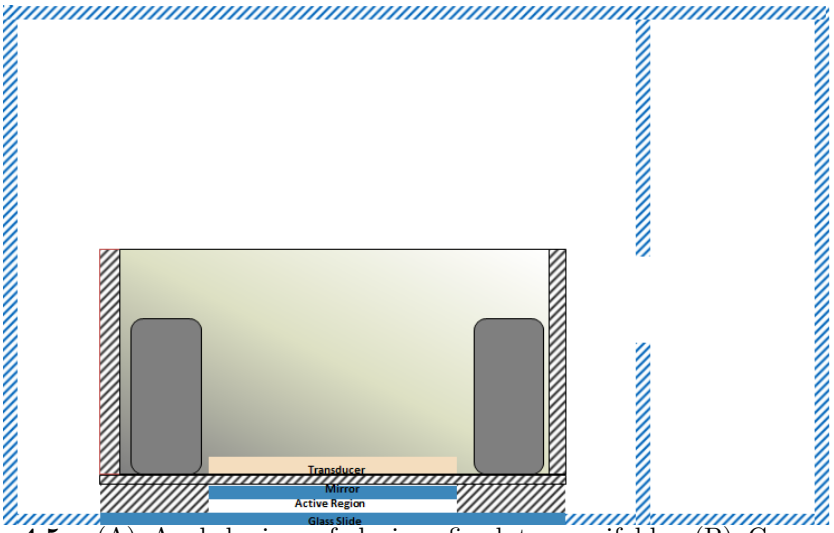

Figure 4.5: (A) Angled view of devices fixed to manifold. (B) Cross-sectional schematic of well device within the manifold. With perfusion, medium will overflow from the device well to the overflow well, where it will be perfused back to the medium reservoir.

The manifold was designed to be modular to easily accommodate alterations to the acoustic devices while reducing the total number of components needed to design an acoustic system. To ensure repeated use of the manifold, composing materials were selected to be autoclavable. To this end, the present system consists of polycarbonate, stainless steel bolts, and nylon luer fittings. PDMS was cured between laminate sheets to function as a gasket and prevent leakage of medium.

4.3.1.1 Wellplate Resonator Design and Characterization

For the multi-well system, layered resonators were designed to be a removable component of the bioreactor platform. Assembled devices had a fluid layer thickness of 300 µm, carrier layer of 1.6 mm and reflector thickness of 1.0 mm.

4.3.1.1.1 Modelling

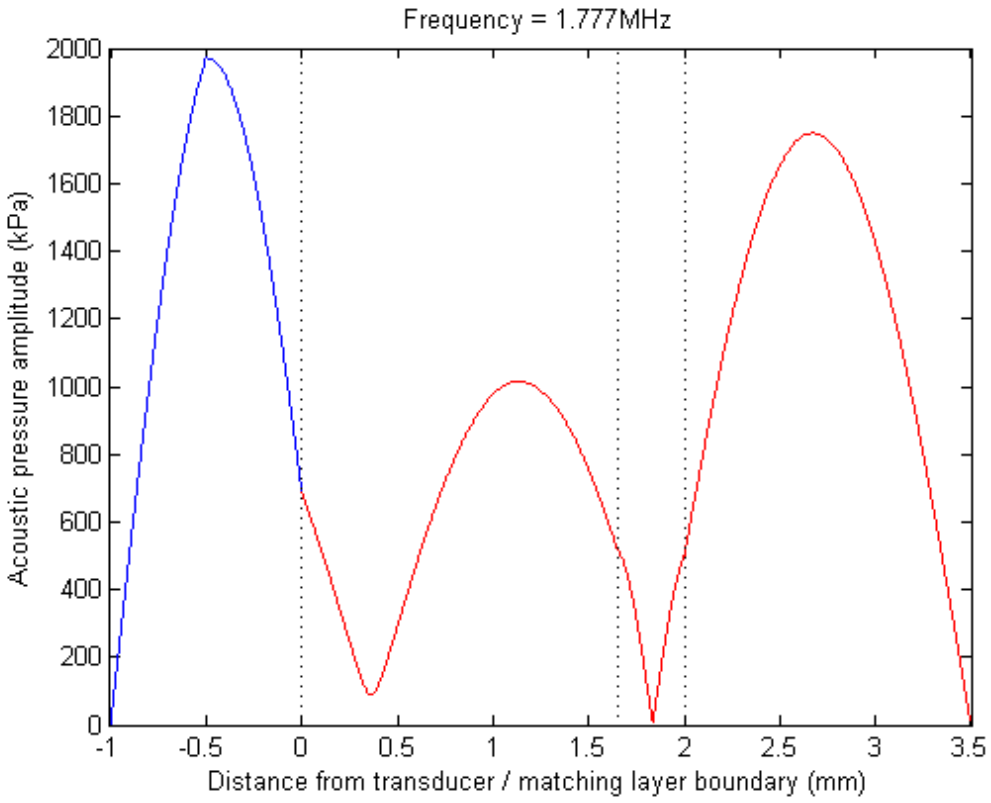

Figure 4.6: Predicted node position for thin device at resonant frequency.

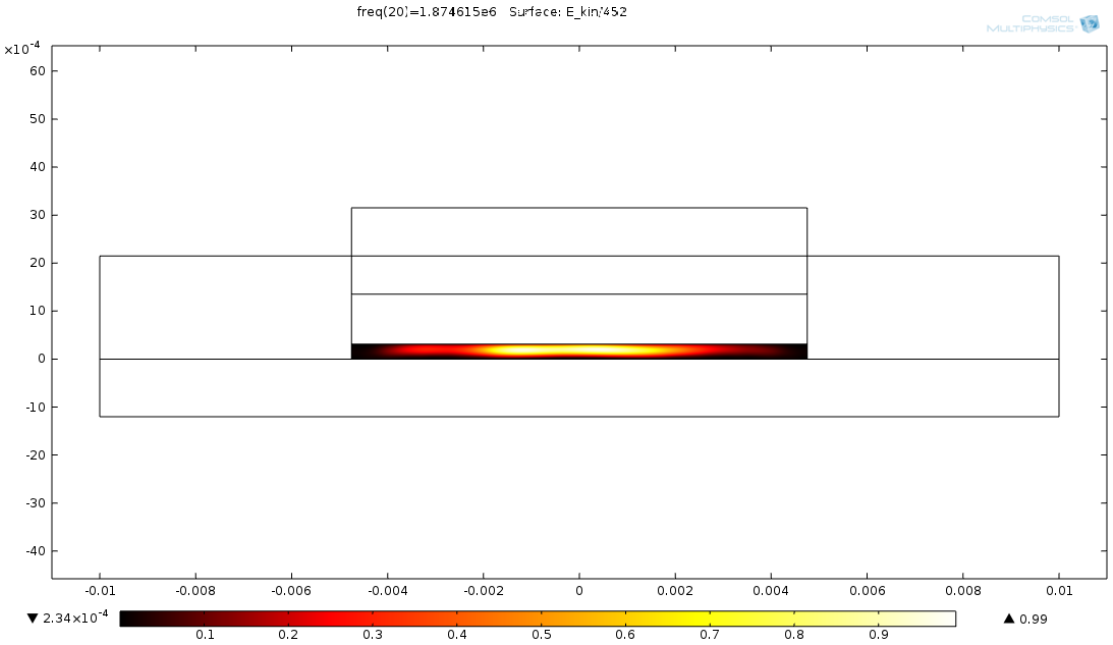

Figure 4.7: FEA model of computed acoustic kinetic energy distribution within thin device at the acoustic resonance.

A transfer impedance model was used to estimate the pressure node position and resonant frequency at which the device could be driven (Figure 4.6). Modelling of the assembled device resulted in an acoustic trap at the half-wavelength when the driving frequency was 1.777 MHz. The peak acoustic pressure generated at this frequency was approximately 600 kPa within the fluid layer. A finite element model was also used to visualize the position and kinetic energy distribution at the pressure node (Figure 4.7). From this, the energy distribution at the single node suggests particle trapping will be highest around the centre of the fluid cavity and weaker towards the boundaries of the fluid layer.

4.3.1.1.2 Cavity Resonance Characterization

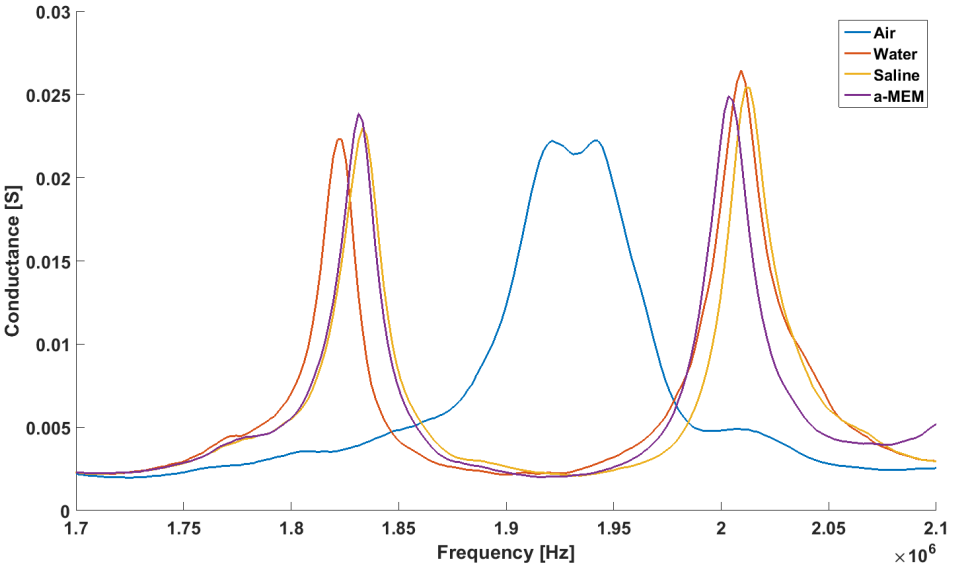

Figure 4.8: Electrical Conductance vs Frequency for resonator with different fluid layers—air (blue curve), water (orange curve), PBS (yellow curve), and α-MEM (purple curve). Resonant frequencies are given to be when the electrical conductance is at a maxima and the air curve is used to differentiate between the transducer peak resonance and cavity resonance, which is the first conductance maxima, in the case of this resonator system.

Conventionally, the cavity resonance for acoustic resonators is computed in water; however, as saline and culture media are both more osmotically compatible with cells, the resonators were characterized first in air, followed by deionized water, phosphate-buffered saline (PBS), and cell culture medium (α-MEM) to quantify potentialy differences in the cavity resonance (Figure 4.8).

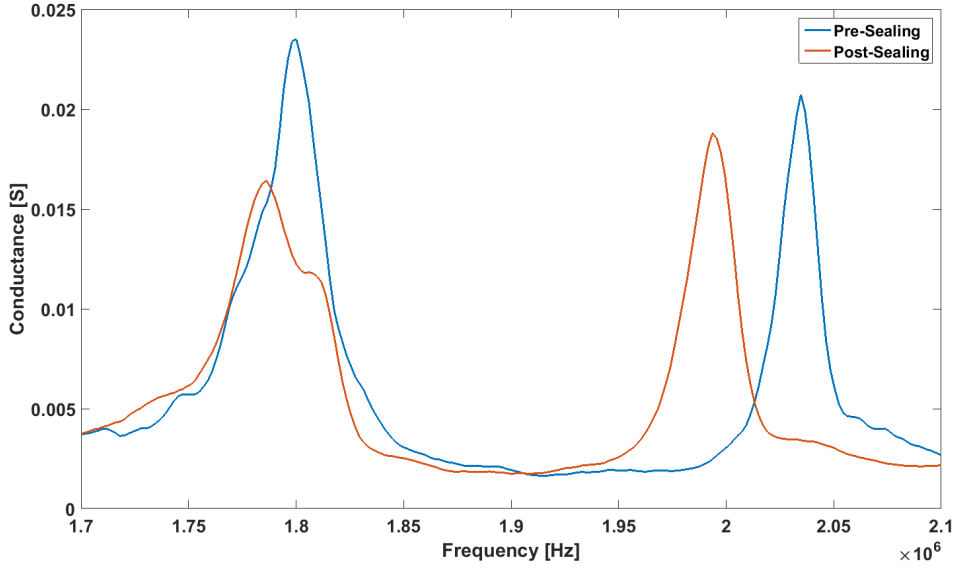

Figure 4.9: Electrical Conductance vs Frequency for resonator in water before sealing the PZT with PDMS (blue) and after sealing with PDMS (orange). Prior to sealing, the resonator was found to have a maximum at 1.84 MHz, with the graph curvature suggesting that the device is also fairly efficient. Following PDMS sealing of the PZT, however, the maxima were noticeably wider, indicating some damping by the PDMS.

In the case of the water curve, the cavity resonance was found at 1.82 MHz, which is comparable to the output from the transfer impedance model. A subtle variation in the resonant frequency was also noted when the devices were immersed in deionized water versus saline or culture medium. This is likely due to solute concentration differences between the different fluids. It should also be appreciated that the saline and culture medium curves are acoustically identical. This may suggest that the salts typically added to saline would more greatly affect the resonant frequency over other solutes normally found in culture medium. In addition to this, the conductance curve for resonators sealed with PDMS was also assessed and compared against the unsealed devices. The resonant frequency post-sealing matched with the devices pre-sealing; however, the corresponding electrical conductance following sealing increased and the curve presented itself as wider, leading to an overall lower Q-factor. The lowered Q-factor would suggest reduced efficiency as a result of dampening by the PDMS backing on the transducer (Figure 4.9).

4.3.1.1.3 Acoustic Pressure Amplitude Characterization

Device Type	**Drop Voltage$_1$ (Vpp)**	**Drop Voltage$_2$ (Vpp)**	**Drop Voltage$_3$ (Vpp)**	**Average Voltage (Vpp)**
unsealed	2.2	2.14	2	2.11
sealed	1.4	1.7	1.3	1.46

Table 4.4: Drop voltage comparisons of devices prior to and following PDMS sealing. Generally, it was observed that the post-sealing drop voltage was lower than that pre-sealing; suggesting more efficient trapping.

Given the conductance variation found when sealing the devices, a voltage drop was performed to quantify the change in acoustic pressure output from the devices pre- and post-sealing. Using a single node configuration, the average drop voltage of the acoustic devices was given as 2.11 Vpp (Table 4.4). From this, a profile for the acoustic pressure amplitude for a given driving voltage was generated to quantify the potential operational range of the devices. This was repeated following PDMS sealing of the devices, where a drop voltage of 1.46 Vpp was found (Figure 4.10).

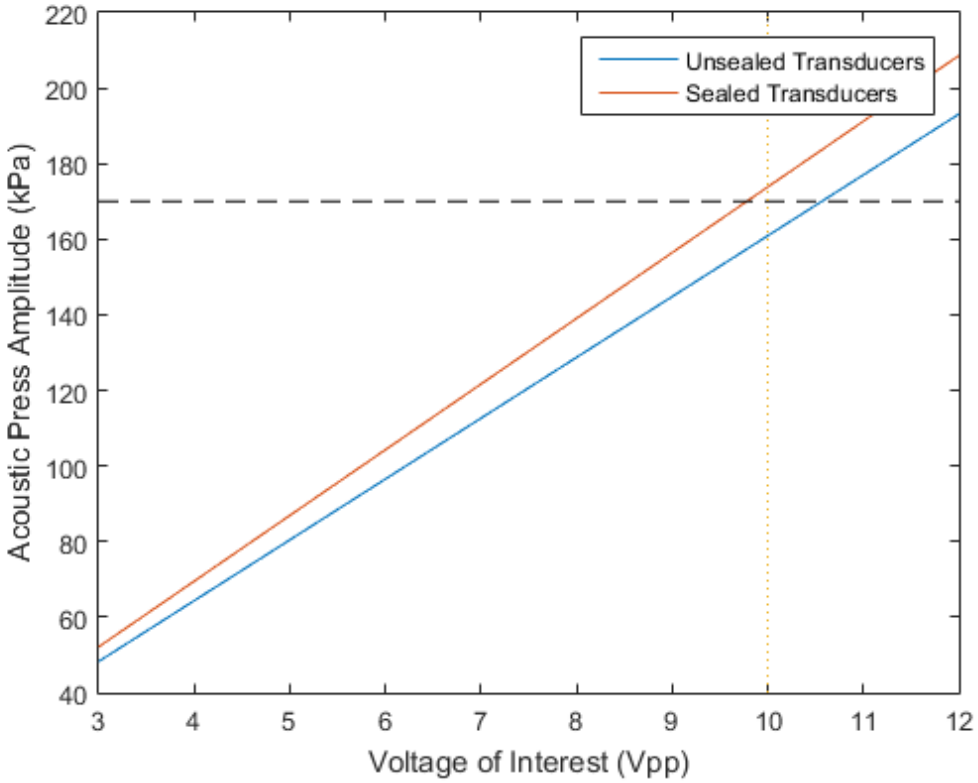

Figure 4.10: Given the drop voltages, acoustic pressure amplitude was computed and plotted against select driving voltages. The driving voltage of the previous system at 10 Vpp (dotted line) generated an acoustic pressure amplitude of 170 kPa (dashed line).

4.3.1.2 Heat Transfer

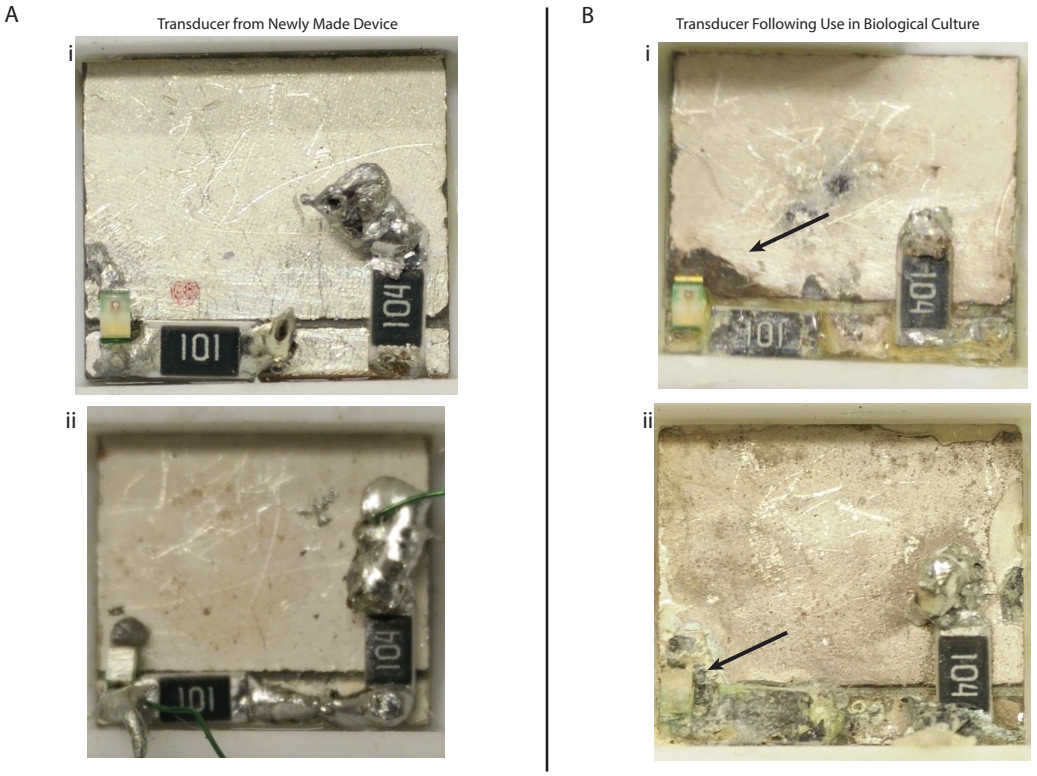

Figure 4.11: Comparison of several wellplate resonators to illustrate the transducer condition difference between (A) unused resonators and (B) following 21 days of biological culture. The used transducer also shows evidence of oxidation on the transducer (arrows), which is absent from the new device.

Wellplate device re-usability was first assessed by comparing the bulk well temperature change to ambient temperature with both freshly made and used devices (Figure 4.11. It was observed that the fresh devices did not change the well temperature significantly, relative to the ambient temperature of either the room or incubator. In contrast, it was noted that used resonators exhibiting oxidation of the electrode transferred more heat to the surrounding fluid (Table 4.5). This difference in heat transfer from the transducer of the device to the surrounding fluid is likely a result of the the PZT decoupling from the carrier layer following three weeks of continuous use and, potentially, interacting with the culture media through leaks in the device walls, leading to oxidation of the transducer electrode.

Ambient Temperature (C)	Well Temperature	Driving Voltage (Vpp)	Device Notes
23.3	23.7	8	new, unsealed transducer
23.3	24.7	8	old, unsealed transducer
36	37.2	8	old, unsealed transducer
36	36.5	8	new, unsealed transducer

Table 4.5: Measured heat transfer by devices into PBS-filled well compared against ambient temperature of room and incubator.

In order to better protect the transducers during culture, PZTs were protected with a layer of PDMS (PDMS sealed devices). In the case of both sealed and unsealed devices at ambient and controlled temperatures, the temperature differences were within 0.2°C of one another. The magnitude of this variation would suggest a near similar heat transfer between the fluid layer and the bulk of the fluid within the well.

Ambient Temperature (C)	Well Temperature	Fluid Layer Temperature	Driving Voltage (Vpp)	Device Notes
18	19.4	19.6	8	new, unsealed transducer
18	18.5	18.8	8	new, PDMS sealed transducer
35	35.7	35.8	8	new, unsealed transducer
35	35	35.2	8	new, PDMS sealed transducer

Table 4.6: Measured heat transfer by devices from the transducer to the fluid layer at ambient and 37°C.

Unfortunately, longer term investigation of heat transfer from the transducer to the well with the sealed devices shown a significant increase in the fluid temperature over four days, after which the fluid evaporated (Figure 4.12). Given this finding, the wellplate bioreactor design would not be a usable option for long-term tissue culture as cell viability would be compromised less than one week into a three week culture period.

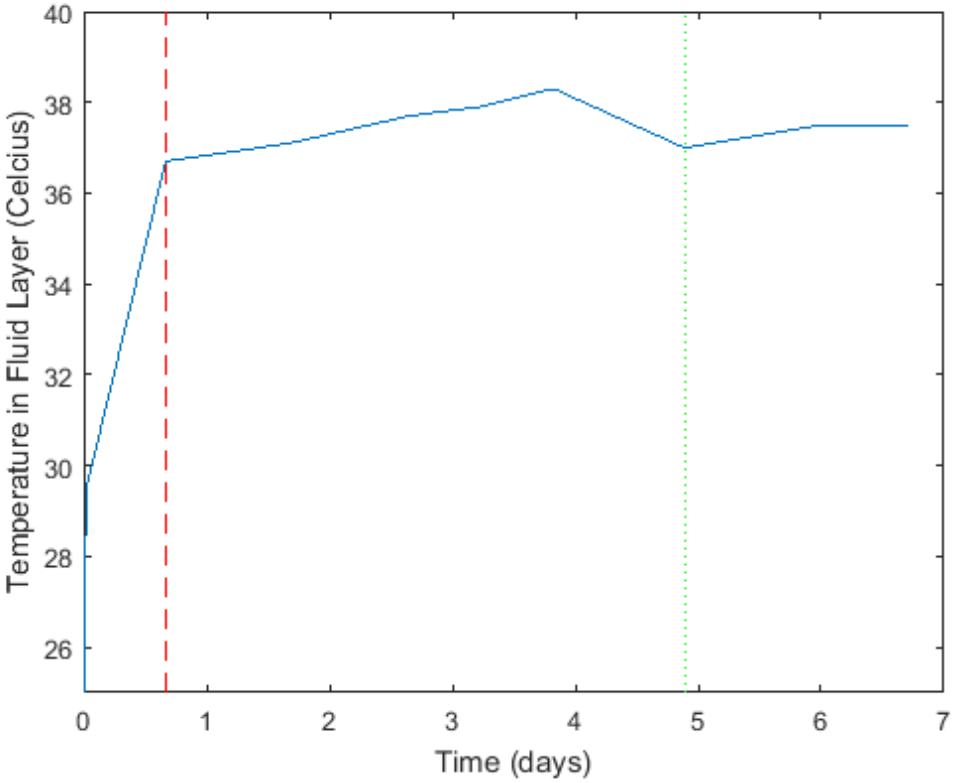

Figure 4.12: Long-term temperature validation for a PDMS sealed wellplate resonator. A thermocouple was placed in the fluid layer to measure the local temperature change over time. The fluid temperature was allowed to stabilise overnight to ensure consistent readings following activation of the transducer (red, dashed line). Temperature readings were found to have increased over the course of four days, after which fluid levels dropped and the thermocouple began reading the air temperature within the cavity (green, dotted line).

4.3.2 Design 2: Inverted Bioreactor

As the increased heating and subsequent fluid evaporation would be detrimental to cell culture, resonators were redesigned such that the PZT was located outside of the culture chamber, in order to allow better air cooling around the transducer and promote cell viability.

4.3.2.1 Modelling

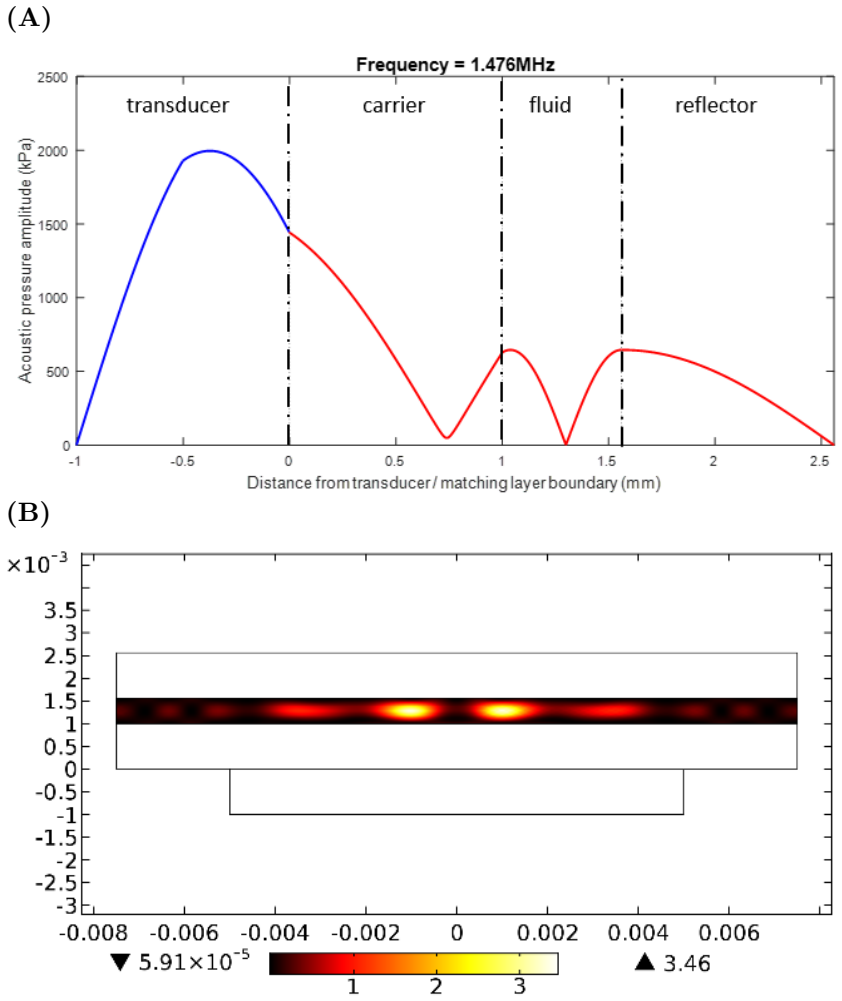

Figure 4.13: (A) A transfer impedance model was used to confirm cavity resonance and presence of pressure node about the centre of the fluid cavity for the desired resonator configuration. (B) The transfer impedance model was further validated with a FE model to determine the kinetic energy distribution within the fluid cavity, as to better understand the energy distribution within the pressure node and where the cells are likely to be levitating.

To validate that the resonator design would generate a pressure node at the half-wavelength of the fluid layer, a transfer impedance model was used to plot the acoustic pressure profile through the transducer, carrier, fluid, and reflector layers of the resonator (Figure 4.13A), fluid layer was given as 0.55 mm and all remaining layers were assumed to be 1.0 mm). Following validation of node position in the fluid layer, a FEM was used to determine the characteristics of the standing wave field (Figure 4.13B). The model simulates the acoustic kinetic energy distribution within the fluid cavity, at the resonance frequency of the resonator. The bright yellow to

white areas within the fluid layer indicates the area where cells may be expected within the acoustic trap. Given that two specific regions exist at the centre of the fluid layer, it can be assumed that the modelled resonator produces lateral nodes, meaning that multiple aggregates are likely to form within the cavity.

4.3.2.2 Resonator Assembly and Characterization

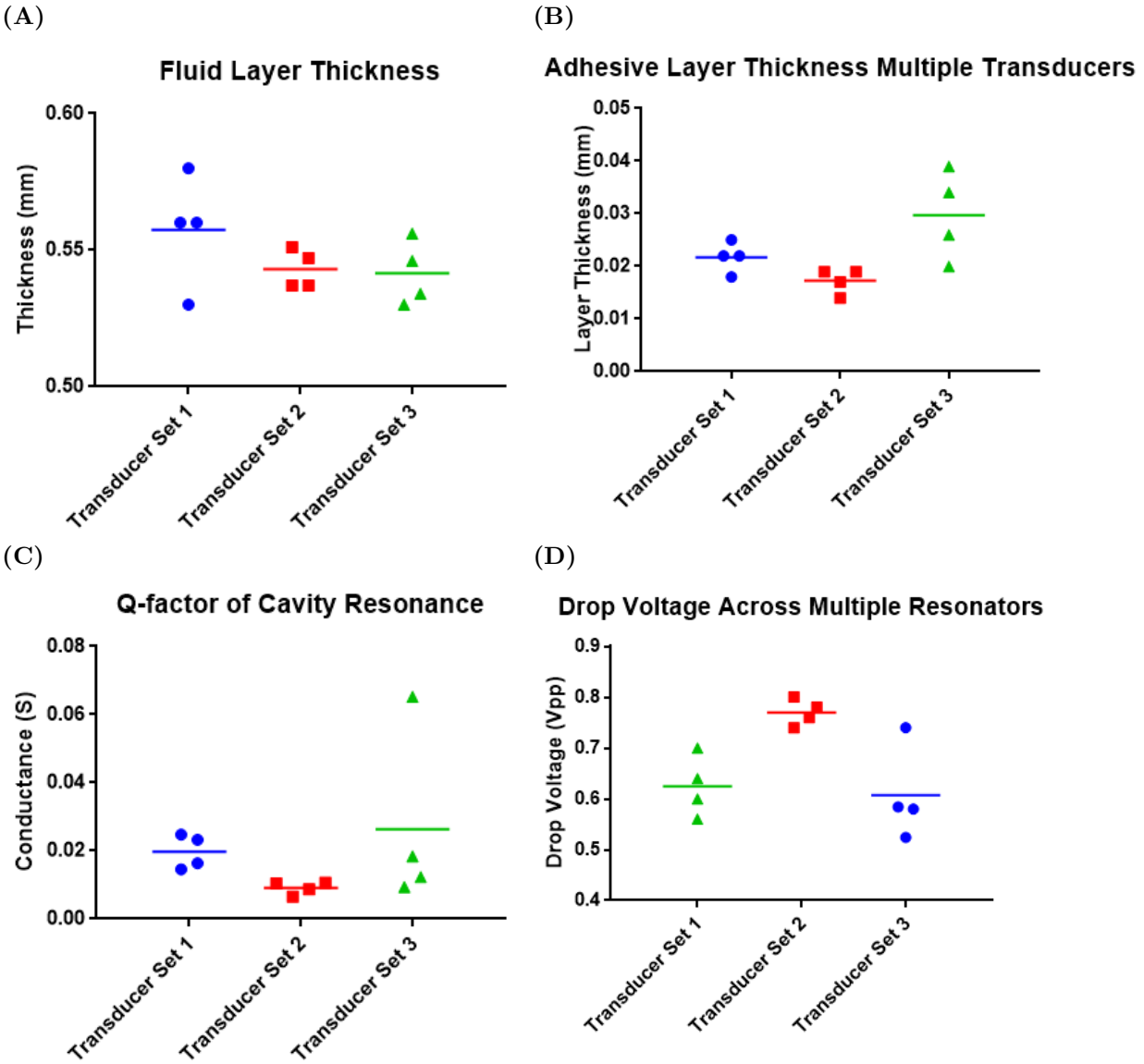

Figure 4.14: Several plates were measured for consistency by means of measuring (A) the fluid layer thickness and (B) coupling layer thickness. Variations in the physical dimensions of the resonators may explain the variability in (C) q-factor of the cavity resonance peak and (D) the acoustic trap strength. Performance of the acoustic trap is determined through the drop voltage-the minimum voltage to maintain a 10 micrometre particle in levitation.

To ensure reproducibility of the assembly protocol, the resonator dimensions were measured. The mean fluid layer thickness was measured to be 0.55±0.009 mm across twelve resonators (Figure 4.14A), which is close to the designed fluid layer thickness of 0.55 mm and within tolerable variation. Considering the original thickness of the PC film being 0.5 mm, the PDMS layer thickness on either side of the film would be 0.025 mm. The coupling layer thickness between the PZT and carrier layer was measured (Figure 4.14B), where the mean thickness was found to vary between resonators on both the same and different plates. This was further seen when determining the cavity resonance of the resonators, where it was observed that the q factor of the resonators were found to vary (Figure 4.14C), suggesting discrepancies in the manual assembly process. The drop voltage was also evaluated as a means of determining any discrepancy in the acoustic pressure output between devices (Figure 4.14D). While it was noted that the mean drop voltage was similar between bioreactor plates, a wide variance exists for the tested resonators. This would suggest that some variability in fabrication process affected the measured drop voltage readings.

4.3.2.3 Improved Long-term Cooling

Heat transfer from the PZT to the fluid layer was validated within the inverted bioreactor by immersing the resonators within saline. The system was placed within a cell culture incubator, where the temperature was maintained at 37°C. A thermocouple was introduced into the fluid cavity to detected the fluid layer temperature. The well temperature was allowed to stabilise overnight prior to generation of the acoustic trap. Over the course of four days, the temperature was recorded to be stable at 37°C ± 0.05°C (Figure 4.15). From this, it can be inferred that the bioreactor design allowed for more appreciable cooling of the transducer into the environment of the incubator, thereby limiting heat transfer to the fluid layer, potentially disrupting cell culture and tissue development.

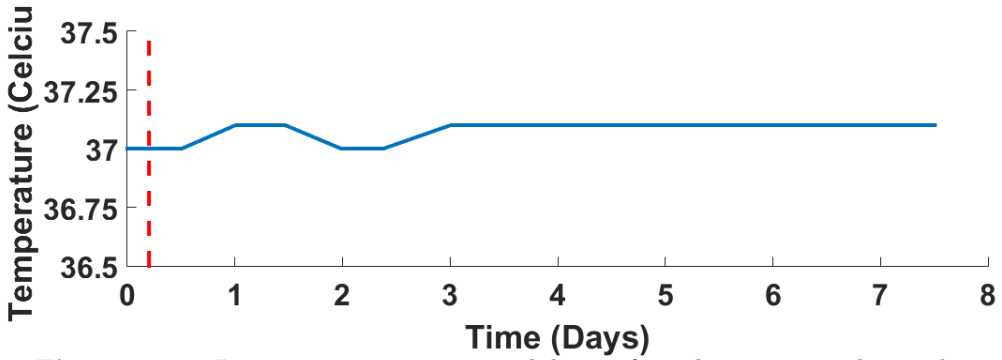

Figure 4.15: Long-term temperature validation for a known worn device driven at its original (pre-run) frequency. A thermocoupler was placed in the fluid layer as to measure the temperature change experienced by cells over time. The fluid temperature was allowed to stabilise overnight as to ensure consistent readings following activation of the transducer (red, dashed line).

4.4 Discussion

Previously, we have shown the potential of an acoustofluidic bioreactor for the scaffold-free development of cartilaginous tissue [22]. Inconsistencies with the hardware occasionally led to inadequate tissue development. The purpose of this chapter was to improve on the initial bioreactor system by creating an open plate system to limit bubble-related culture failure and investigate the role of the acoustic environment during tissue culture.

The shift to a well-plate based system also allowed for the development of multiple constructs simultaneously, whereas the previous bioreactor design allowed for the generation of a single construct at a time. The layered resonators were constructed as an interchangeable part to limit device-related inconsistencies and maximise the overall modularity of the system. The mirror back-plate allowed for enhanced contrast of cells and aggregates for both fluorescent imaging and phase-contrast, whereas previous bioreactor iterations required cells to be fluorescent labelled for visualization against the Macor/ceramic transducer. Unfortunately, certain design elements for this well-plate system made it unsuitable for biological culture. Notably, continuous use of the wellplate resonators within the well resulted in a number of issues, resulting in increased heat transfer from the transducer to the well and active region of the device. As this heating would adversely affect cell viability within the bioreactor, the resonator design was changed to limit heat transfer from the transducer to the fluid layer.

The second design described in this chapter was observed to better dissipate the heat from the PZT and limit adverse heating of the active region within the trap. While this system does require more extensive hand assembly, characterization of the resonators for drop voltage and layer thicknesses found little variation between devices. As such, further biological culture and interactions between the acoustic forces and the cells would be accomplished using the inverted bioreactor design.

Chapter 5

Frequency Modulated Acoustic Stimulation for Cartilage Engineering

5.1 Introduction

Given the avascular nature of articular cartilage and low mitotic activity of the resident chondrocytes, the tissue exhibits a limited capacity for self-repair, which will eventually compromise the structural mechanics of the tissue and lead to degradation of the lining and osteoarthritis. There are currently no effective pharmacological agents to promote comprehensive healing of the articular cartilage and while surgical treatments, such as autologous chondrocyte implantation (ACI) and microfacture, provide temporary relief to patients, they are unable to restore the functionality of the damaged tissue over the long term [2, 31]. To this end, tissue engineering has been employed to generate functionally relevant, hyaline-like cartilage grafts.

Literature has highlighted the importance of the physiochemical environment in promoting robust cartilage generation [14, 15]. Mechanical stimulation using hydrostatic loads and cell stretching, among other forces, have been applied to activate mechanotransduction pathways and promote chondrogenesis in cells [16, 17]. Dynamic stimulation (e.g. cyclic shear or dynamic compression) of the cells has been shown to result in the generation of more robust cartilage, compared to stimulation of cells with

static forces [16]. Furthermore, mechanical stimulation of chondrocytes results in the secretion of parathyroid hormone-related protein (PTHrP), a chemical factor that has been found to aid chondrogenesis and reduce hypertrophy [228, 234, 235]. Thus, there is clear evidence that biomechanical stimulation of chondrocytes promotes chondrogenesis.

In recent years, cell-environment responses and phenotypic changes have been investigated in the field of bioacoustofluidics using ultrasonic standing wave fields. Ultrasonic standing wave fields, or acoustic traps, have been applied using either bulk acoustic waves (BAWs), or surface acoustic waves (SAWs) to induce patterning, alignment, and clustering of cells [18–21] within a micro-channel. Recent literature has described a number of configurations of both SAW and BAW-based traps for cell manipulation [21, 22], and preliminary findings have shown the ability to engineer functional hepatocyte and neuronal aggregates using scaffold-based and scaffold-free methodologies [23, 24].

BAW propagation traditionally occurs within a layered resonator [159], where a piezoelectric transducer is coupled to a chamber. The transducer creates a standing wave field within the fluid space of the chamber, where there exists an energy gradient in which the cells are subjected to acoustic radiation forces. As cells are introduced into the wave field, primary radiation forces direct the cells to a region of low acoustic potential energy, or pressure node. Intercellular attraction within the pressure node is determined by the secondary radiation, or Bjerknes, forces [76], which allow for the formation of an initial aggregate of levitating cells. To accompany acoustic radiation forces, acoustically induced flows by streaming may form within the fluid and improve nutrient exchange with the levitating aggregate.

In the approach introduced in this thesis, I use an acoustic trap to aggregate cells and by modifying the ultrasonic field we have generated time varying radiation forces and drag forces on the cell aggregates. A number of groups have suggested that similar acoustically generated forces can affect cells and matrix proteins within the field [18, 22, 189, 247]. repeated displacement of the cells introduces mechanical stimulation in the form of fluid shear stress and this has the potential to alter the development of cartilage tissue within a scaffold-free environment. To date, however, investigation of scaffold-free tissue culture via bioacoustofluidics has been limited and

little is known concerning how the acoustic environment can be exploited to maximise the potential of this approach.

The previous chapter detailed the design of the next generation acoustofluidic bioreactor that has the advantages of immunity from bubble build-up, easy cell injection, parallelized throughput, and the potential for scaling to larger construct sizes. In this chapter, I identify sources of mechanical stimulation created in the bioreactor, and demonstrate that the acoustic environment can be electronically modulated to produce cartilage of more optimal properties. It has been reported that mechanical stimulation of chondrocytes results in the secretion of parathyroid hormone-related protein (PTHrP), a chemical factor that has been found to aid chondrogenesis and reduce hypertrophy [228, 234, 235]. The combination of mechanical stimulation with this factor is investigated here and found to further promote robust cartilage development when used in combination with acoustically derived stimulation to promote robust cartilage development.

5.2 Materials and Methods

5.2.1 Acoustic Streaming Characterization

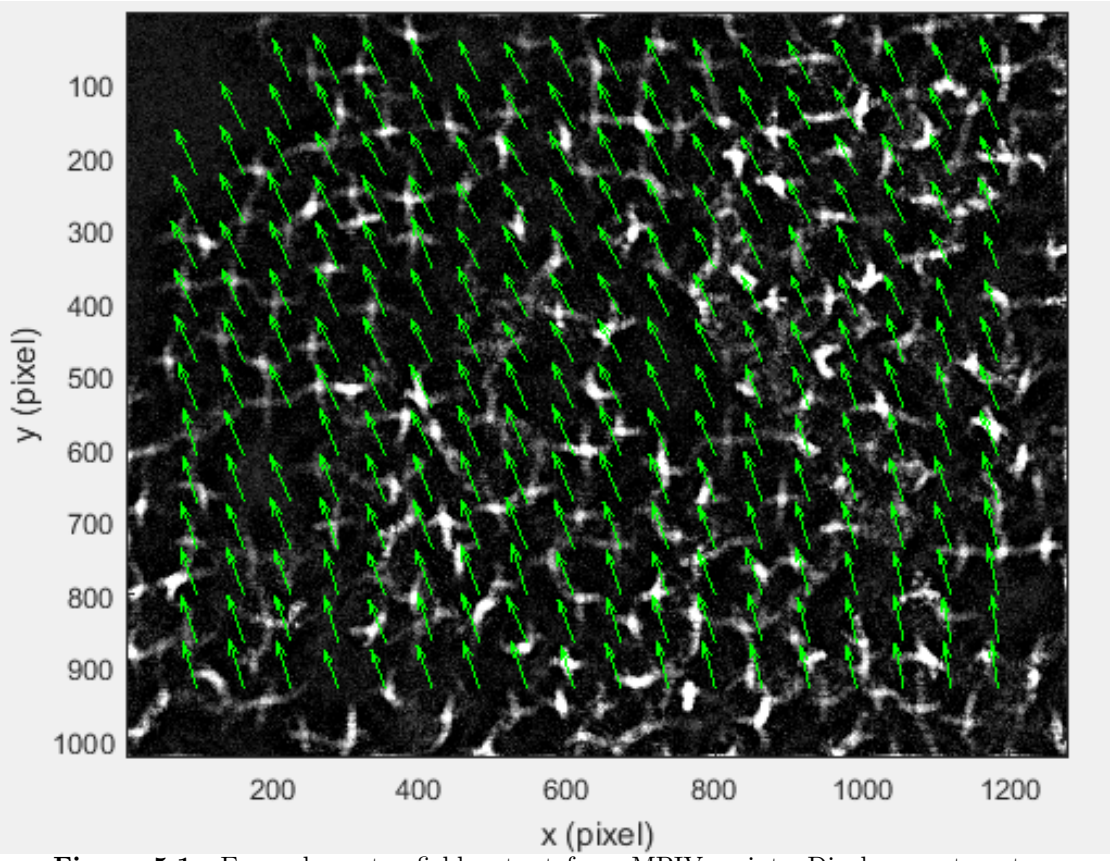

Figure 5.1: Example vector field output from MPIV script. Displacement vectors (arrows) are generated between segmented blobs found between two consecutive images.

The acoustic streaming velocity within the acoustic trap was characterized using 1 µm fluorescent polystyrene beads. Bead movement is influenced by acoustic drag forces and was captured via time-lapse imaging using a 10x objective and 400 msec frame interval. Image data was analysed via a particle image velocimetry (PIV) toolbox in MATLAB (MPIV) to quantify bead displacement and mean particle velocity between sequential frames. MPIV was accomplished as described in Zmijan *et al.* [164].

To improve the algorithm's ability to accurately trace particle paths between sequential frames, the images were first eroded using a 16 pixel^2 disk element (Figure 5.1). Following particle identification, tracing between frames was accomplished using an interrogation window 6% of the frame size and assuming a maximum displacement of the cells of 2.5% along the x and y axes. Following particle

analysis through the time-lapse video, the median of the dataset was then take to be the average particle velocity for a parameter set.

5.2.2 Characterization of Acoustic Environment

To understand the effect and, specifically, the stresses applied onto the cells during culture, a number of frequency sweep parameters were tested: ranges of 100 kHz and 200 kHz about the centre frequency at sweep repetition rates of 1, 2, 5, 10, 20 and 50 Hz. Imaging of ATDC5 levitated in this environment was performed at a rate such that 16 frames were acquired for each frequency sweep, to ensure sufficient sampling (i.e. the frame rate for the 1 Hz sweep was 16 fps and 800 fps for 50 Hz). Sampling continued until 10 such cycles had been captured. The resulting time-lapse data was analysed via image cross-correlation to determine the displacement of the cells between sequential frames at different sweep repetition rates. The displacement data was then introduced into an analytical model to determine the fluid shear stress applied onto the cells. This model was further validated with an FEM to better support the analytical results.

Given the repeatable displacement path of the cells as they are stimulated, and that one full motion can be seen in a single period, the shear stress amplitude on the cells was reported as the peak-to-peak stress. This was computed across resonators within the same plate as well as across multiple sweep repetition rates at a sweep range of 100 kHz and 200 kHz.

5.2.2.1 Analytical Model for Approximating Fluid Shear Stress

For the analytical model, the resulting displacement data was curve fitted through a two term Fourier regression and the second order coefficients were used to calculate the resulting shear force on the cells (Equation 5.1A). Oscillations occurring at the pressure node were computed using Stoke's boundary layer model for a rigid plane (Equation 5.1B) moving with a velocity amplitude defined by V_o, where the pressure node was assumed to be at a non-slip boundary ($z = 0$) (Equation 5.1C). This motion

was assumed to result in fluid shear stress applied onto the cells (Equation 5.1D–E).

$$\tau = \mu \frac{\partial v}{\partial z} \tag{5.1a}$$

$$v(z,t) = V_o e^{-kz} \cos(\omega t - kz) \tag{5.1b}$$

$$\frac{\partial v}{\partial z} = -V_o k e^{-kz} \cos(\omega t - kz) + V_o k e^{-kz} \sin(\omega t - kz) \tag{5.1c}$$

$$\frac{\partial v}{\partial z} = V_o k e^{-kz} [\sin(\omega t - kz) - \cos(\omega t - kz)] \tag{5.1d}$$

$$\tau = \mu V_o \sqrt{\frac{\omega}{2\nu}} [\sin(\omega t) - \cos(\omega t)] \tag{5.1e}$$

$$\tau = -\mu V_o \sqrt{\frac{\omega}{\nu}} [\sin(\frac{\pi}{4} - \omega t))] \tag{5.1f}$$

Where μ and ν are given as the dynamic viscosity and kinematic viscosity of water at 37 °C, respectively, ω is the angular frequency, and k is the wavenumber, where $k = \sqrt{\frac{\omega}{2\nu}}$ [248]. A MATLAB script was written to process the average displacement data and is provided in section A.2. The mathematical model was further validated through a simple fluid shear model in COMSOL with the experimentally derived velocity data to calculate the fluid shear amplitude.

5.2.2.2 Finite Element Model for Approximating Fluid Shear Stress

To determine the shear stress applied onto the cells, a 3D laminar flow based model was used to simulate the oscillating movement of the cells and compute the magnitude of fluid shear stress on the cells. The model simulated half of the fluid layer of the resonator, such that the upper boundary of the model represented the carrier layer and the bottom boundary functioned as a moving wall to simulate the oscillating movement of the cells. The experimentally derived displacement data was applied as a velocity boundary condition (after smoothing with a piecewise cubic function) to the moving wall to better simulate the aggregate movement within the fluid layer at different acoustic parameters.

5.2.3 Bioreactor Culture of Human Articular Chondrocytes

Monolayer cultured HACs were harvested at confluence and suspended in serum-free chondrogenic medium consisting of α-MEM supplemented with transforming growth factor-beta (10ng/mL, TGF-β3, Peprotech 100-36E), 1x ITS, dexamethasone (3.92 ng/mL, D4902), and L-ascorbate-2-phosphate (28.95 ng/mL, A2P, A8960) at a concentration of 1x10^6 cells/50 μL. The cell suspension was then introduced into a resonator using a flexible gel-loading pipette tip and cultured for 21 days under hypoxic conditions (37^{o}C, 5% CO_2 and 5% O_2). At day 10, 10 ng/mL Parathyroid hormone-related protein (PTHrP) and proline were introduced to the chondrogenic media and maintained until the end of the culture point. 3D pellet culture, as described below, was used as a control condition to compare against the bioreactor culture. Following end of culture, the reflector layer was removed and the generated constructs were extracted from the device and chemically fixed overnight with 90% ethanol. Sample preparation for histology and staining was accomplished as previously described subsection 3.2.6.

5.2.4 Organotypic Defect Model and Mechanical Testing

In order to assess the mechanical properties of the engineered tissue, the constructs assessed by nanoindentation. To ensure the test output was reflective of the tissue construct without any substrate influence [249], the constructs were implanted into native cartilage and cultured for six weeks prior to nano-indentation. To create an appropriate mounting location, cartilage explants were harvested from the non-loaded regions of osteoarthritic femoral heads and a defect was manually introduced into the explant using a 3 mm ball-drill bit. The engineered cartilage was positioned into the defect and the model was cultured on a transwell insert for six weeks at 37^{o}C and 5% CO_2. Following the culture period, samples were mounted into a liquid cell for mechanical testing.

Following the culture period, nanoindentation testing was performed using a NanoTest Vantage System (Micro Materials, Wrexham, UK), using a 400 µm diameter, diamond cono-spherical tip (E_i = 1141 GPa, ν_i = 0.07) in the liquid cell attachment to ensure the samples were submerged in PBS and stayed fully hydrated. The indentation points

were manually selected on both the native cartilage and the engineered tissue. Given the viscoelastic nature of cartilage, the indentation measurements were run in load control to a maximum load of 0.05 mN at a rate of 0.005 mN/second with a dwell at peak load of 60 second to ensure a linear loading/unloading response from the tissue, thereby permitting the tissue to be assessed as an elastic material. The average indentation depth from both the native and engineering cartilage was measured to be 2.5 µm±0.39 µm, which is less than 5% of both tissue types, meaning that the indentation points may be assumed to reflect the material properties of the indented tissue and not the underlying substrate [249].

The data acquired from three indentation points was used to determine the mean reduced modulus (E_r) for either the native or engineered cartilage and repeated for three patient samples. In order to obtain the Young's modulus (E_s) from the reduced modulus output by the nano-indenter, the Poisson's ratio (ν_s) of both the native and engineered cartilage was assumed to be 0.34 [250–252]. The Young's modulus was then calculated by rearranging the terms from the general indenter equation (Equation 5.2) [253].

$$E_s = \frac{(E_i E_r)(1 - {\nu_s}^2)}{E_i - E_r(1 - \nu_i^2)} \tag{5.2}$$

5.2.5 Microscopy

Fluorescence timelapse images were acquired using an Olympus upright fluorescence microscope with FITC filter (excitation/emission wavelengths: 485 nm/515 nm, Olympus), Rhodamine filter (excitation/emission wavelengths: 546 nm/560 nm, Olympus), and Orca-Flash4.0 (Hammamatsu) with HCImage software.

5.3 Results

5.3.1 The Acousto-mechanical culture environment

It was previously observed that by making small (up to 50 Hz) variations to the electrical driving frequency around the acoustic resonance, the acoustic forces change

to displace the aggregation positions of the cells laterally [22]. Thus, by periodically varying this frequency (using a linear frequency sweep) the aggregates are caused to vibrate backwards and forwards, inducing fluidic shear and deformational stress on the cell aggregates. For the purposes of this thesis, I use the term sweep repetition rate to denote how often the sequence of applied frequencies is cycled through, exploring a range of 1–50 Hz. Simply speaking, this corresponds to the observable frequency of lateral vibration of the aggregates. It is important to note that the cells will be exposed to both the lateral, cyclic oscillations from the frequency sweep and surrounded by constant fluid flux as a result of acoustic streaming within the wave field. It should also be appreciated that the mechanical stresses will have higher order frequency components due to the complex relationship between acoustic frequency and lateral position. The magnitude of the cyclic shear stresses vary with both the sweep repetition rate and the amplitude of the driving waveform as discussed below. In the initial phase of cell culture (typically around 14 days), aggregates would be in full levitation, and the primary source of stimulation on the cells at this time would from the lateral oscillations. Later on, the aggregates would grow to a point where they contact the device walls and cease to move so freely. During this phase the acoustic forces are more likely to induce deformation-related stresses, however I only quantify the fluid-shear derived forces in this chapter.

5.3.1.1 Perfusion and Acoustic Streaming flows

(A)

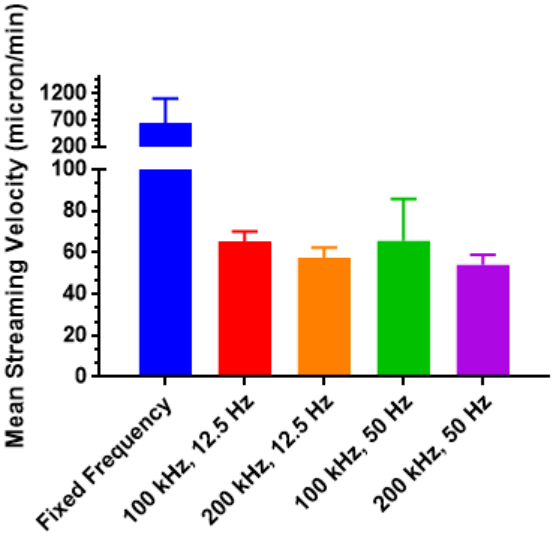

(B)

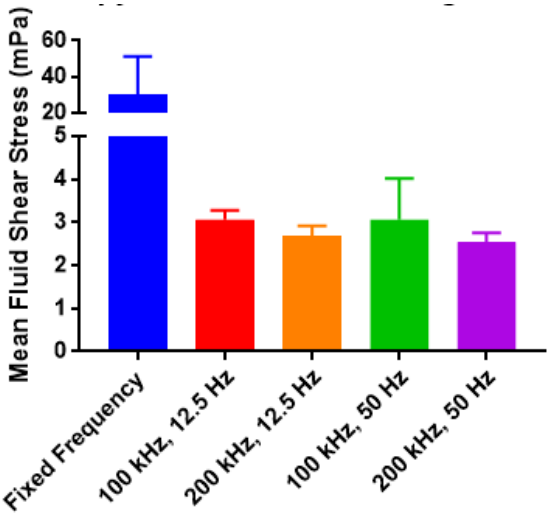

Figure 5.2: Acoustic streaming forces would influence (A) fluid flow within the resonator and, correspondingly, some of the (B) fluid shear stress applied onto the cells. The streaming velocities within the acoustic trap at different driving parameters. Velocities were computed at the cavity resonance (fixed frequency) compared against a 100 kHz and 200 kHz frequency sweep at a sweep repetition rate of 50 Hz and 12.5 Hz. While a variation was observed in the velocity magnitudes between a driving the system at a fixed frequency, 100 kHz, and 200 kHz, the sweep repetition rate did not greatly influence the fluid flow as a result of streaming. Correspondingly, the fluid shear stress from acoustic streaming stays relatively constant between different sweep repetition rates. Note that in addition to the calculated shear stresses from the acoustic streaming, there will additionally be shear stresses resulting from the movement of the cells caused by the acoustic radiation forces shown in Figure 5.4B. (n = 3, $\bar{x} + SD$)

Driving Parameter Set	**Mean Streaming Velocity (µm/min)**	**Mean Fluid Shear Stress (mPa)**
Fixed Frequency, 10 Vpp	640 ± 456	29.9 ± 21.3
100 kHz, 12.5 Hz, 10 Vpp	65.3 ± 4.66	3.06 ± 0.22
100 kHz, 50 Hz, 10 Vpp	65.4 ± 20.4	3.06 ± 0.95
200 kHz, 12.5 Hz, 10 Vpp	56.3 ± 6.57	2.63 ± 0.33
200 kHz, 50 Hz, 10 Vpp	52.0 ± 4.45	2.43 ± 0.21

Table 5.1: Summary of mean fluid velocities and shear stresses exerted by the acoustic streaming forces.

Acoustic streaming is the mean flow induced in a fluid due to absorption of the ultrasonic energy [80, 254]. In this case, it is boundary driven streaming, resulting from acoustic energy dissipated in the device walls [81, 255]. Motion of the media in our system due to acoustic streaming was found to be comparable in magnitude to previously reported pumped media-perfusion flow velocities [22]. In our system, block media changes mean that this is the sole source of perfusion flow. Acoustic theory [256, 257] predicts that streaming velocities are likely to be independent of the sweep repetition rate. My results uphold this as illustrated in Figure 5.2 and summarized in Table 5.1, where it was observed that the mean streaming velocities at a frequency sweep of 200 kHz and sweep repetition rates of 12.5 Hz and 50 Hz were 56.3 ± 6.57 and 52.0 ± 4.45 µm/min, respectively. At these same sweep repetition rates and frequency sweep of 100 kHz, the resulting mean streaming velocities are marginally higher than those at 200 kHz (Figure 5.2A). These velocities can also be compared to the perfusion flow of 34 µm/min previously reported [22]. It is important to note that the average acoustic energy entering the system is independent of the sweep repetition rate, hence other acoustic energy-based effects on cells (such as heating) will also be independent of this. The shear stresses ((Figure 5.2B) on the cell aggregates resulting from these streaming flows are calculated to be 2.63 ± 0.33 and 2.43 ± 0.21 mPa for a frequency sweep of 100 kHz and sweep repetition rate of 12.5 Hz and 50 Hz, respectively. These continuous stresses will be applied to the aggregates in addition to the typically larger time-varying ones derived from the periodic lateral movement discussed below.

5.3.1.2 Modulating aggregate displacement and fluidic shear stresses

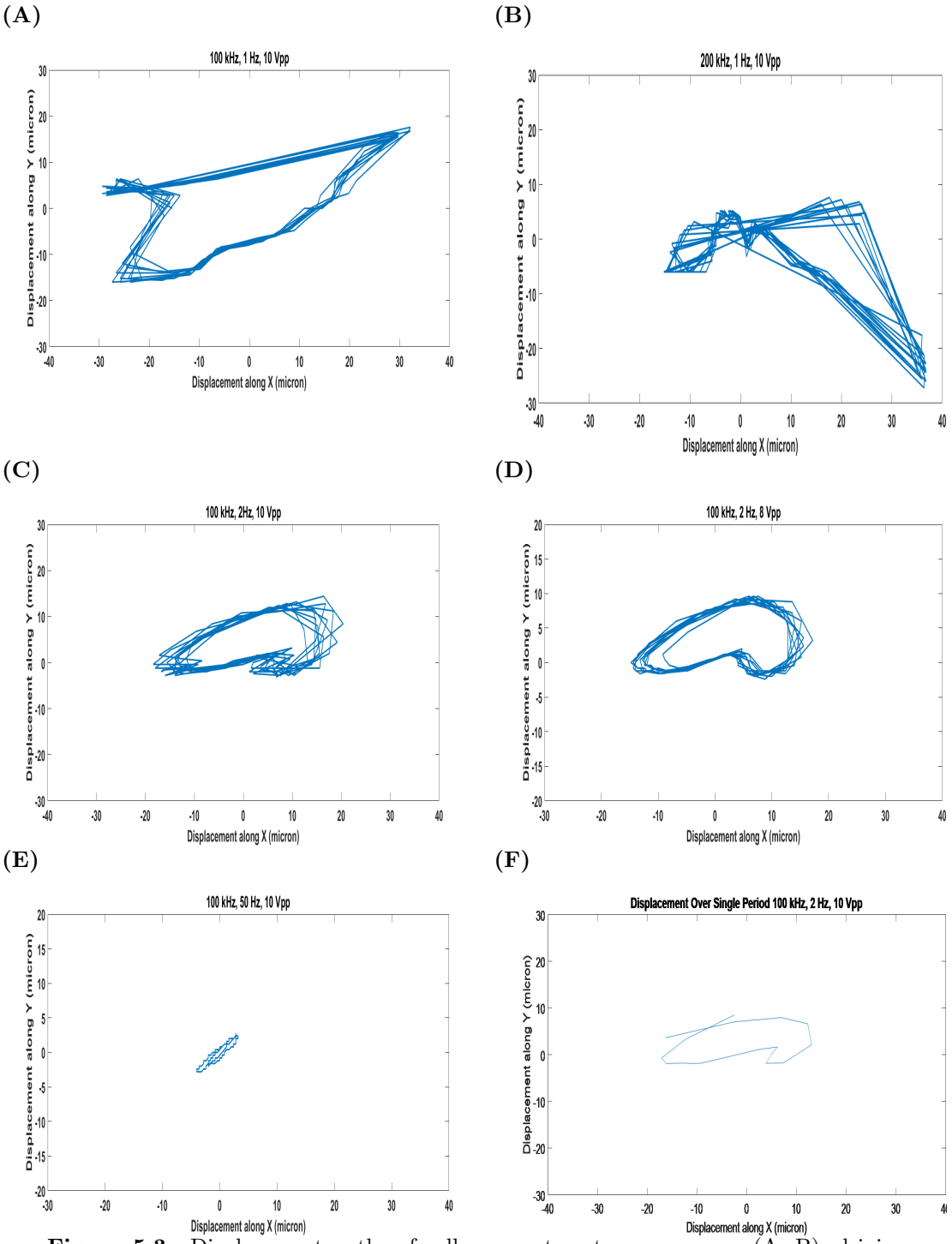

Figure 5.3: Displacement paths of cell aggregates at sweep ranges (A, B), driving voltages (C, D), and different sweep repetition rates (A, C, E). The particle displacement over a single period is denoted in (F) for 100 kHz, 2 Hz, 10 Vpp, indicating the repeatable nature of the cell movement. The displacement amplitude was found to vary with the sweep repetition rate as well as the driving voltage to the trap. Particle paths varied with for a given sweep repetition rate and range (AC), whereas altering the driving voltage changed the size of the particle path, but had little effect on the shape of the path taken by the cells.

To quantify how the acoustic driving parameters modulate the paths traced out by the cell aggregates, and the resulting fluidic shear stresses, ATDC5 cells were imaged in levitation. Figure 5.3 shows example paths derived from image processing. It was observed that the sweep repetition rate affected the shape of the path followed by ATDC5 cell aggregates (Figure 5.3), and the size of the area traced out. Higher sweep repetition rates displayed reduced lateral displacement of the cells, with 50 Hz displaying virtually no measurable displacement. I deduced that for the parameters explored, the aggregates are in dynamic motion, limited by viscous drag. Essentially, at higher rates the aggregates have less time to move significantly before being redirected towards another location.

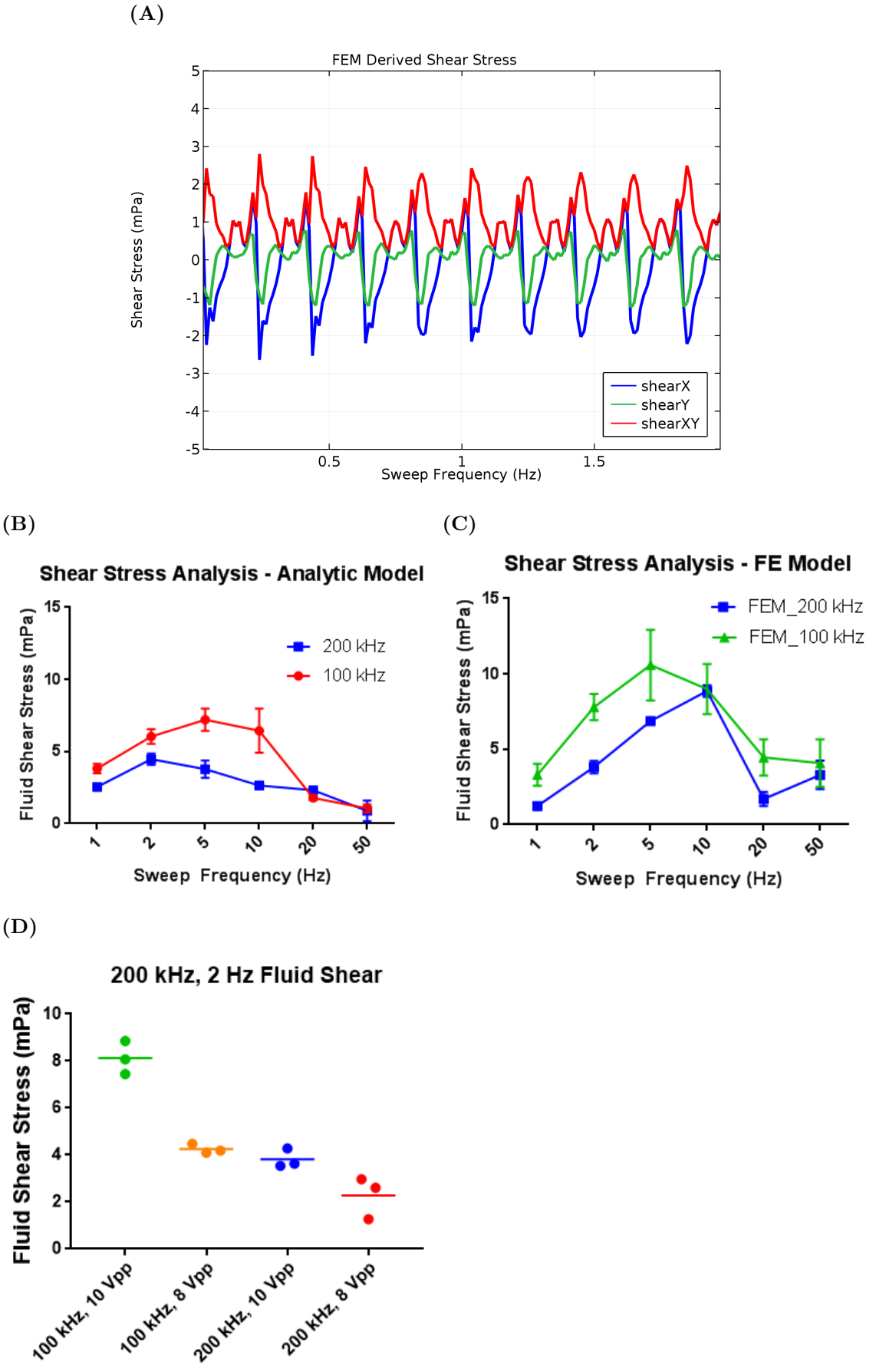

Figure 5.4: Shear analysis was determined at different sweep repetition rates by modelling the displacement profiles on the cells along a moving boundary. (A) It was observed that the resulting shear stress on the boundary was repeatable long multiple cycles through a (B) 100 kHz and (C) 200 kHz sweep range. (D) Finally, the stress magnitude was also quantified at different driving voltages to show that the degree of mechanical stimulation is highly tunable across a variety of parameters. All data points were constructed from n = 3 (mean ± SD)

The time-varying shear stress is plotted in Figure 5.4A, and is seen to be a steady, periodic waveform. Given the cyclic nature of the stress and complex two-dimensional movement of the cell aggregate movement I choose to extract the peak-to-peak value of the stress waveform for subsequent comparison. Relative to 100 and 200 kHz, the model also suggests a reduction in the shear applied onto the cells as the sweep range increases. The relationship between sweep repetition rate and shear stress is shown in Figure 5.4B, C, which shows a peak stress in the region of 5 Hz, decreasing either side of this. More detailed examination of the role of driving voltage and repeatability (at 2 Hz) is shown in Figure 5.4D—increased voltage leads to increased shear stresses, related to the expected squared dependence of acoustic forces on driving voltage. It should also be appreciated that the shear stresses exerted onto the cells is similar across multiple resonators (Figure B.2), meaning that there should be reasonable uniformity between tissue produced by multiple resonators on a single bioreactor plate.

As a result, it can be seen that by controlling both the sweep repetition rate, and the driving voltage our system is able to be programmed to deliver a specific frequency and amplitude of mechanical stimulation to the cells over the course of the culture period.

5.3.1.3 Time-Dependent Investigation to Aggregate Structure and Fluid Shear Stress

Following the shear stress determination at t0, the cells were cultured within the acoustic trap to determine any short-term changes to the aggregate and the acoustic environment. It was observed over the course of 22 hours that the cell nuclei became more circular and condensed in shape and further altered the aggregate structure to a multi-layered conformation (Figure B.1). Given this, it can be inferred that the ATDC5, following introduction to the trap, spread laterally whilst maintaining a multicellular structure axially due to the cell-cell interactions between chondrocytes.

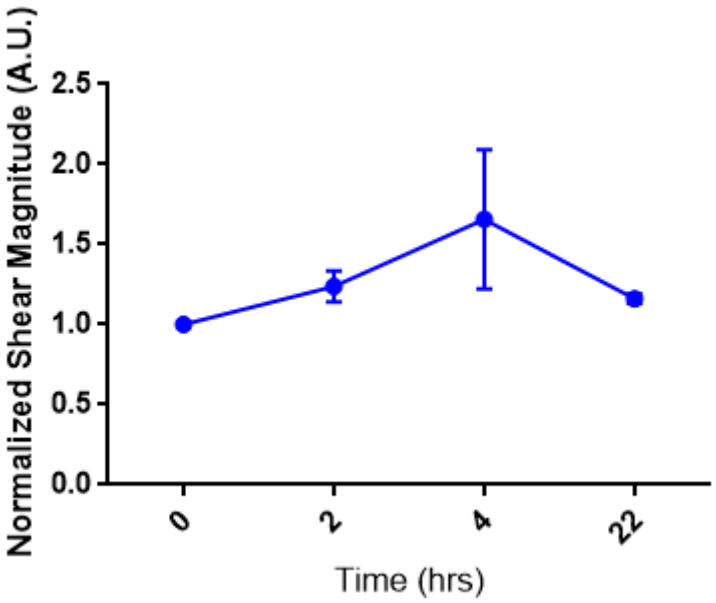

Figure 5.5: Shear stress was measured at various time points over 22 hours to determine how the aggregate changes in response to the applied forces. Resulting shear amplitude was normalized to the initial shear stress amplitude to better visualize changes to the stress magnitude over time. Within the first day of culture, it was noted that the stress on the cells increased between two and four hours following the start of the bioreactor culture. Towards the second day, however, the shear magnitude was noted to have decreased to better match the force applied to the cells within the first two hours of culture. All data points were constructed from n = 3 (mean ± SD).

The fluid shear applied on the cells was further investigated over a short-term culture to understand how the stress applied onto the cells changes as the aggregate grows and changes its structure over the culture period (Figure 5.5). Shear stress was measured at various time points over one day of culture to determine how the aggregate changes in response to the applied forces. Resulting shear amplitude was normalized to the initial shear stress amplitude to visualize change. It was noted that the stress on the cells increased between two and four hours following the start of the bioreactor culture. Towards the 22 hour point, however, the shear magnitude was noted to have decreased to be similar to the force applied to the cells within the first two hours of culture. The overall change in stress magnitude over time is not significantly different relative to t0, so it can be inferred that the overall shear stress on the cells stays constant over this time period in spite of the morphological change to the aggregate depicted in Figure B.1.

5.3.2 Biological response to physico-chemical environment within acoustic trap

The role of the physicochemical environment within the acoustic trap in stimulating cartilage development was assessed at different sweep repetition rates at constant drive voltage. The mechanical stimulation regime that promoted hyaline-like cartilage formation was then supplemented with the growth factor, PTHrP, to examine whether this provided additional chemical cues in combination with mechanical stimulation for improved human cartilage formation.

5.3.2.1 21 day culture of human articular chondrocyte (HAC) aggregates in presence of varying sweep repetition rates

HAC aggregates were cultured for 21 days in the acoustic traps using either a sweep repetition rate of 50 Hz (Figure 5.6) or 2 Hz (Figure 5.7) and the resulting 3-D tissue constructs were harvested for histological and immunohistochemical analyses of cartilage formation.

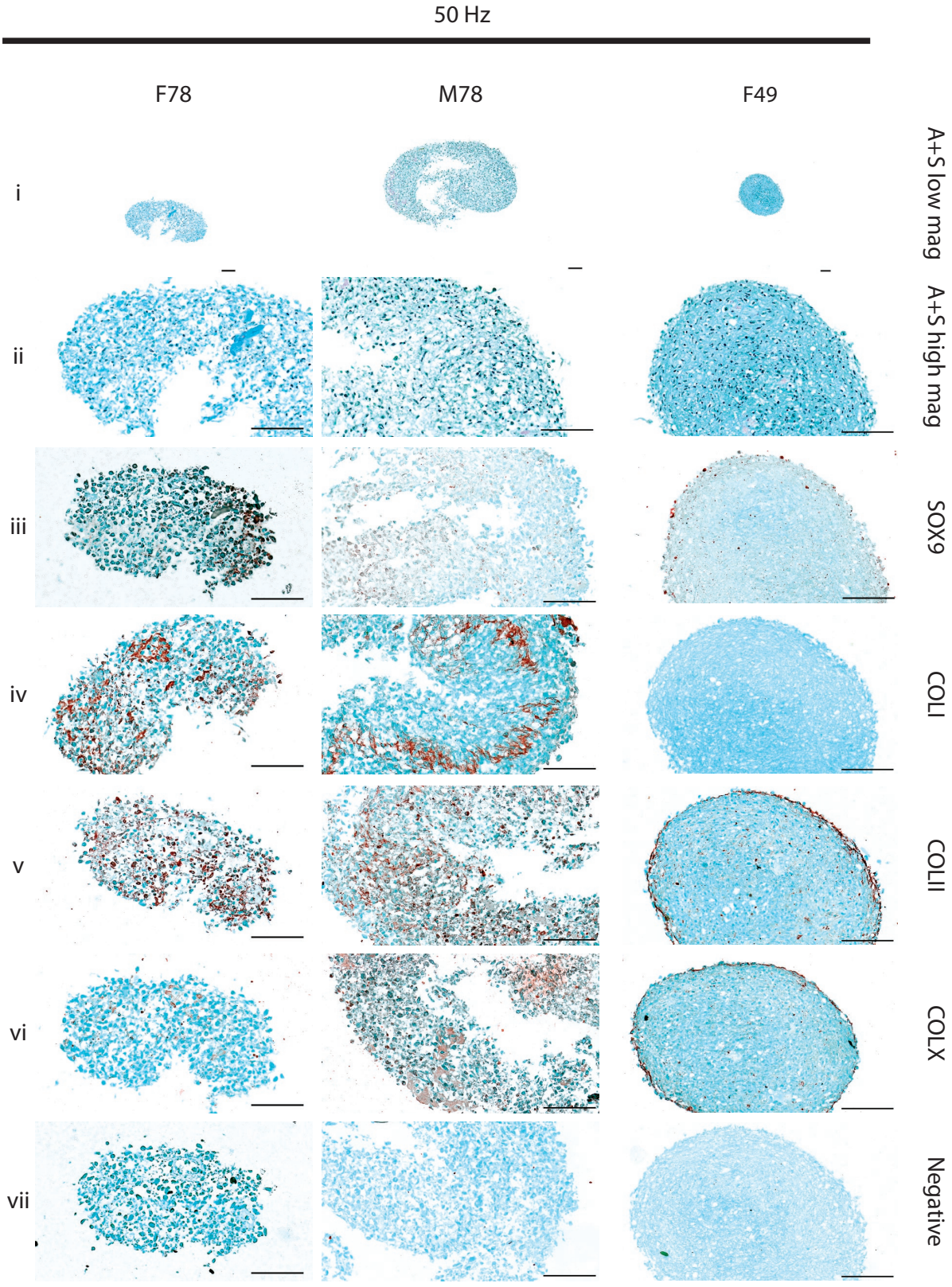

Figure 5.6: HAC tissue constructs following 21 days of culture within acoustic devices at 50 Hz. The 50 Hz regime produced subpar cartilage where type-II collagen (COLII) was primarily found on the tissue periphery and very few cells express SOX9 staining. Tissue sections were selected from a representative set of three patients. Scale bars = 100 µm

Day-21 constructs generated in the bioreactor in response to a sweep repetition rate of 50 Hz (Figure 5.6) were significantly small in size ($\tilde{3}$00 µm) and appeared as aggregates of cells held together by extracellular matrix, which was largely composed of proteoglycans stained with Alcian blue (Figure 5.6i-ii). The constructs exhibited negligible expression of the chondrogenic proteins, namely SOX-9 (Figure 5.6iii) and Type-II collagen (COLII) (Figure 5.6v), coupled with negligible immunostaining for collagens Type-I (COLI) and Type-X (COL X) (Figure 5.6vi).

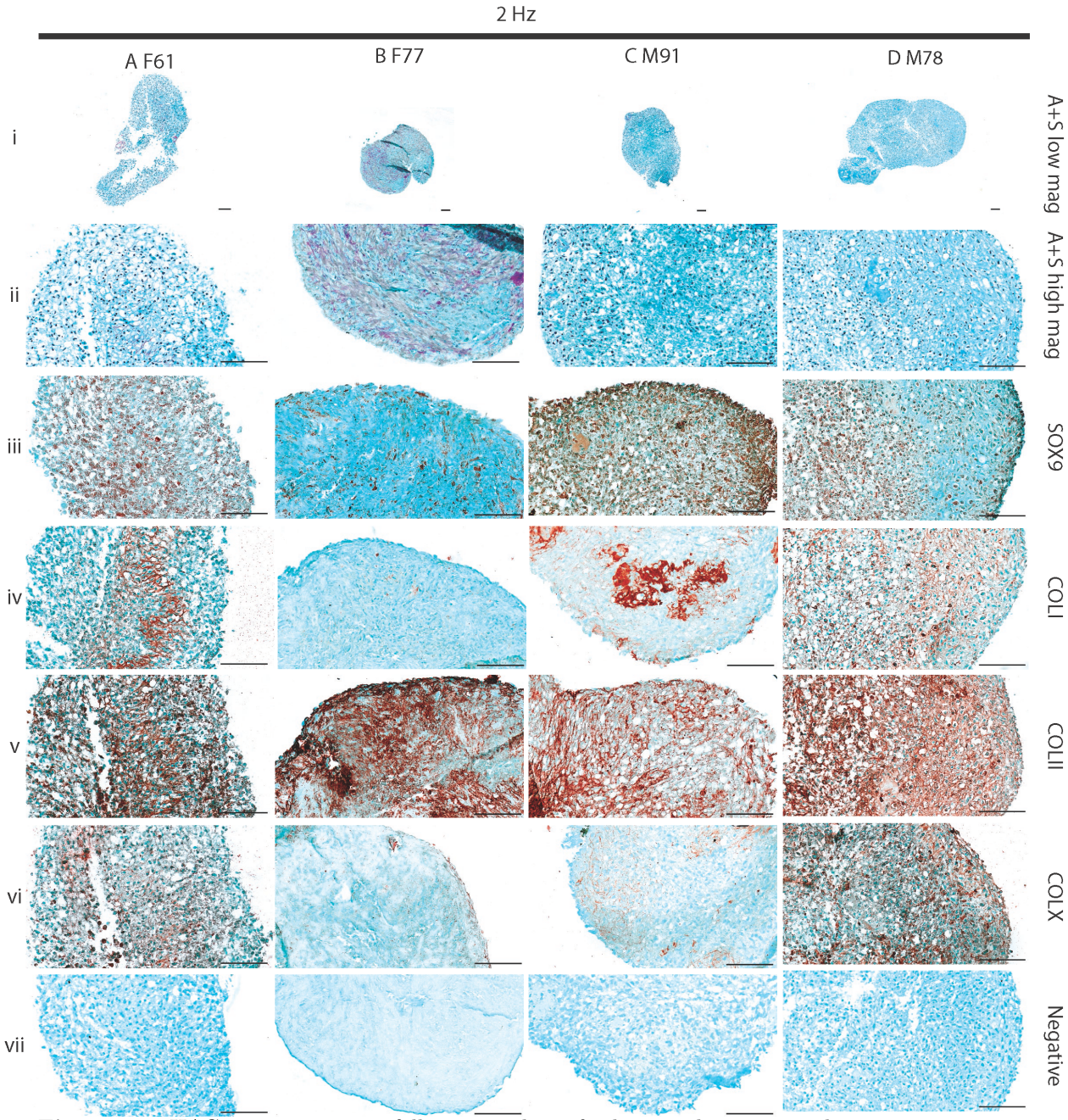

Figure 5.7: HAC tissue constructs following 21 days of culture within acoustic devices at 2 Hz. In contrast to the 50 Hz regime, the 2 Hz regime resulted in more COLII as well as type-I and type-X collagen (COLI and COLX, respectively) distributed within the matrix. SOX9 staining was also expressed within more of the cells in the case of the 2 Hz regime. Tissue sections were selected from a representative set of four patients. Scale bars = 100 µm

In contrast, day-21 constructs generated in the bioreactor in response to a sweep repetition rate of 2 Hz (Figure 5.7) were consistently larger in size (Figure 5.7i depicts a construct that is 1.42 mm by the longest length). Most cells in the cartilaginous constructs had organized themselves within distinct lacunae embedded in the Alcian

blue-stained, proteoglycan-rich extracellular matrix (Figure 5.7i, ii). Moreover, robust expression for SOX-9 and COLII were observed in the cells and the surrounding extracellular matrix, respectively (Figure 5.7iii, v). However, it was possible to detect distinct immunostaining for COLI and COLX in the extracellular matrix of the cartilaginous constructs (Figure 5.7iv, vi).

5.3.2.2 Supplementation of Bioreactor Culture with PTHrP

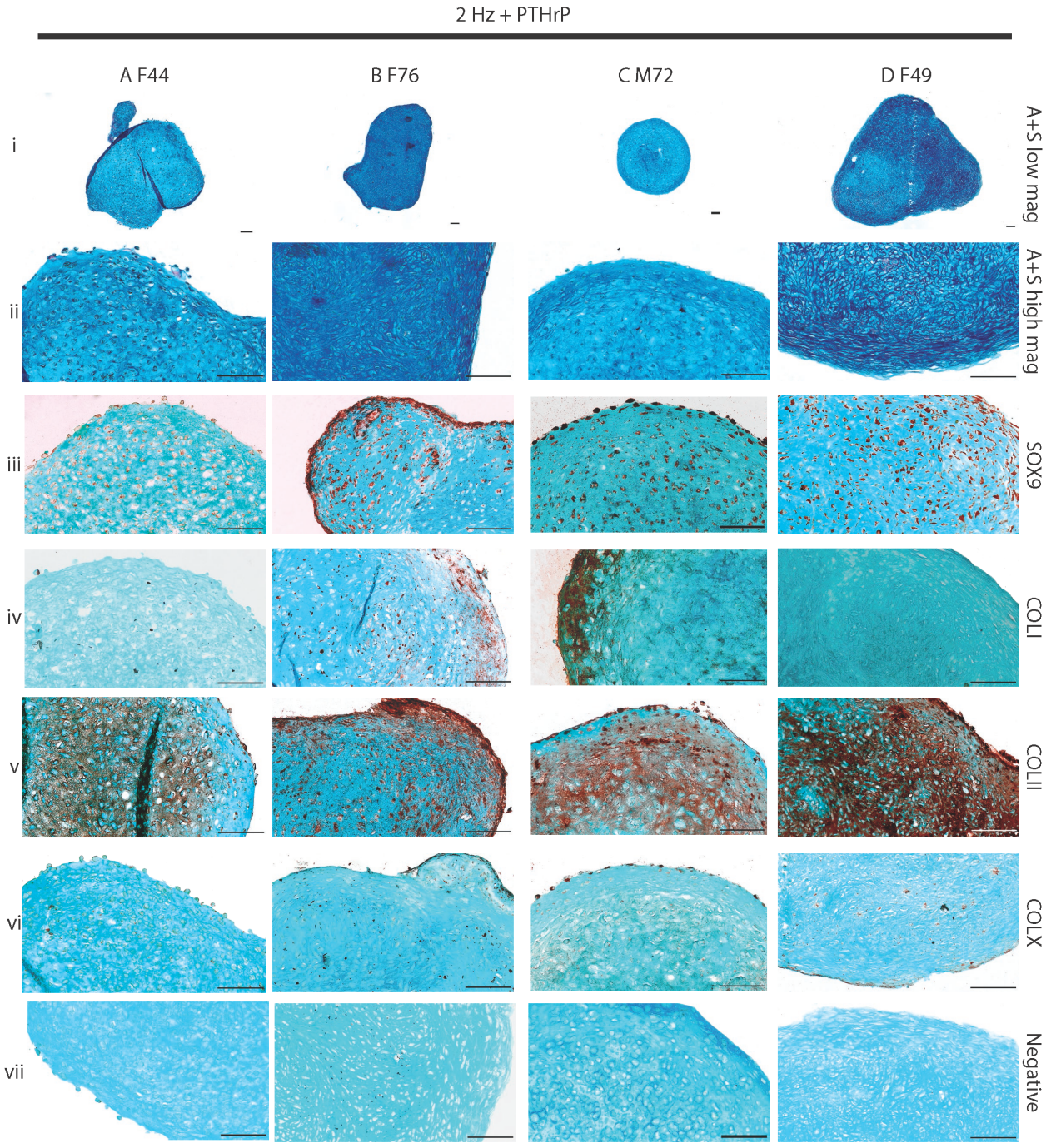

Figure 5.8: HAC tissue constructs following 21 days of culture within acoustic devices at 2 Hz. Culture was supplemented with PTHrP at D10-21. Supplementation of 2 Hz culture with PTHrP resulted in a more robust tissue structure and reduction of COLI and COLX within the matrix, relative to the 2 Hz regime. Tissue sections were selected from a representative set of four patients. Scale bars = 100 µm

To assess the possibility of further enhancing the cartilage structure, chondrocytes that were stimulated by a sweep repetition rate regime of 2Hz for three weeks were cultured

in the bioreactor in chondrogenic medium supplemented with PTHrP from day 10 to the end of culture (i.e. 2 Hz + PTHrP regime). Day-21 constructs generated using these culture conditions (Figure 5.8) were appreciably larger in size (1.71 mm along the longest length for Figure 5.8i) compared to constructs generated in response to sweep repetition rates of 50 Hz and 2 Hz without the supplementation of PTHrP. The cartilaginous constructs were reminiscent of native hyaline cartilage as they were composed of numerous chondrocytes, which expressed SOX-9 and were located within distinct lacunae embedded in dense extracellular matrix containing Alcian blue-stained proteoglycans and abundant COLII (Figure 5.8i–iii, v). Furthermore, expression of COLI was markedly reduced in the cartilaginous constructs and restricted to the peripheral layer of the constructs (Figure 5.8Div). Due to the inhibitory effect of PTHrP on chondrocyte hypertrophy, negligible expression of COLX was observed in the cells and the extracellular matrix of the cartilaginous constructs (Figure 5.8vi). This coupled with the marked absence of the two hypertrophic markers, namely Osteopontin (OPN) and Alkaline phosphatase (ALP), confirmed that the culture regime prevented terminal differentiation of the chondrocytes within the hyaline-like cartilaginous constructs (Figure 5.9).

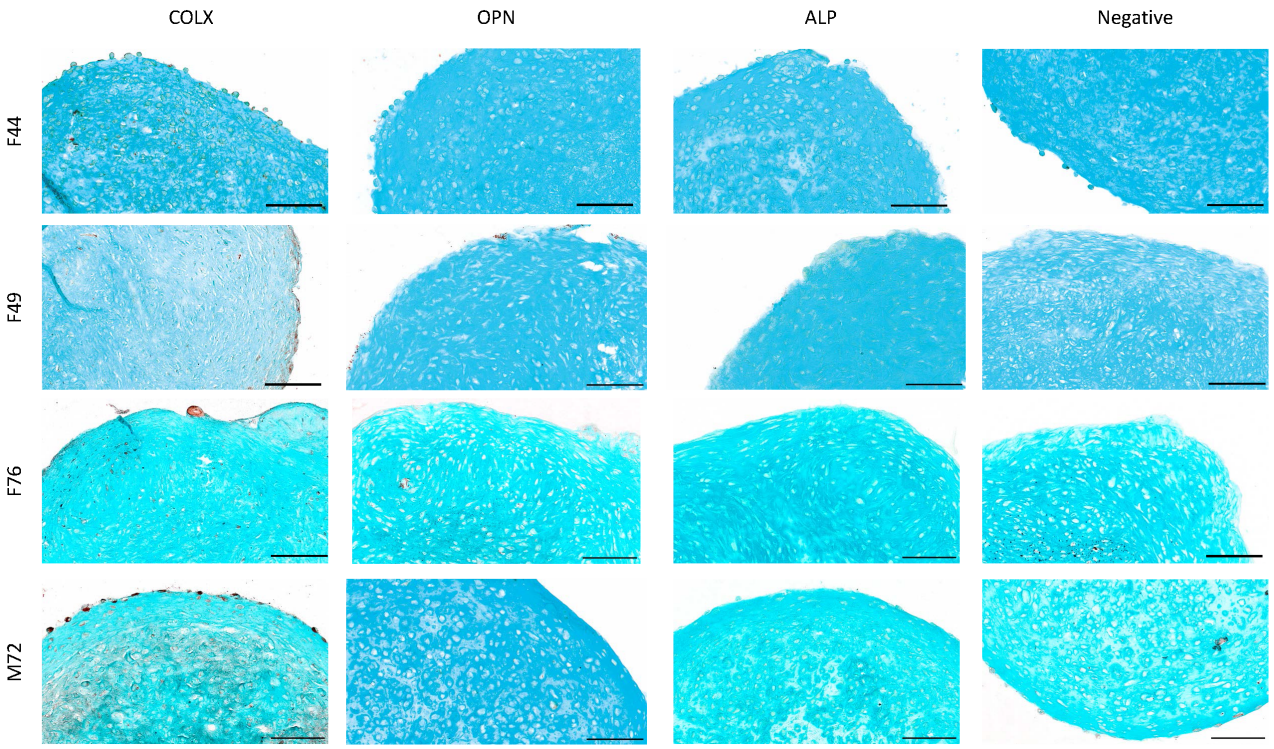

Figure 5.9: Further histological assessment of 2 Hz + PTHrP samples for hypertrophy. Samples were found to have noticeable intracellular staining of COLX. Further staining for osteogenic markers (alkaline phosphatase and osteopontin) was not appreciably observed, suggesting that tissue did not display significant development of hypertrophic cartilage. Scale bars = 100 µm

5.3.2.3 Integration with native tissue and mechanical testing

Constructs formed at 2 Hz + PTHrP were cultured for six weeks within native cartilage (Figure B.3). Nano-indentation was used to assess mechanical properties. Multiple indentations were made on both the engineered tissue and the native cartilage; at least 4 points were used to generate an average for a given patient (Figure 5.10). The reduced Young's modulus is proportional to the bulk modulus by Poisson's ratio, which literature has given to be 0.34 [250–252]. The native cartilage elastic modulus (187 ± 23 kPa), was of comparable stiffness to the engineered tissue (200 ± 63 kPa).

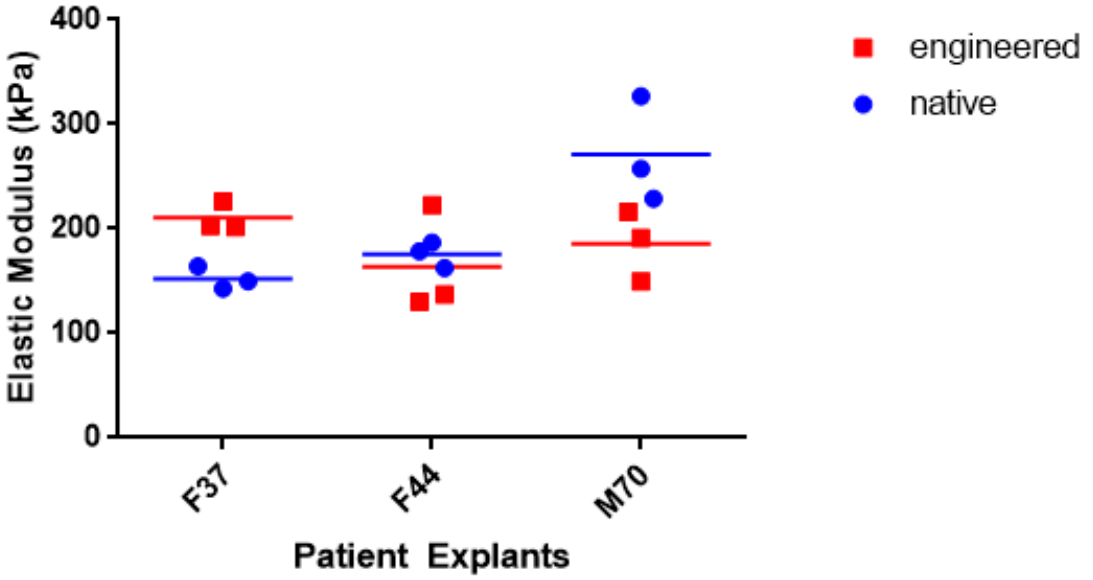

Figure 5.10: Mechanical properties of the engineered cartilage tissue was compared against native cartilage to further quantify the quality of the constructs. A spheroidal diamond tip was used to indent the tissue 3 µm below the surface. The resulting force measurements were used to compute the reduced Young's modulus and viscoelastic properties of the constructs. The reduced Young's modulus is proportional to the bulk modulus by Poisson's ratio, which was assumed to be 0.34.

5.4 Discussion

In this chapter, I designed a novel acoustofluidic bioreactor system to culture chondrocytes in levitation to generate hyaline-like cartilage. I have investigated and quantified how the fluidic shear stresses produced by the bioreactor could be modulated electronically, and assessed resulting differences in tissue constructs. I showed that the ability to modulate the stresses opens the possibility of tuning the system to promote better cartilage formation.

For this study, I describe the biomechanical interaction between the acoustic field and the cells as a result of the acoustic streaming drag forces and acoustic radiation forces. Acoustic streaming allows for nutrient exchange around the developing tissue at velocities comparable to previously reported perfusion culture [22]. The acoustic radiation forces direct both cell levitation and aggregation to certain energy sites within the pressure node. Additionally, it was recognized that sweep through a range of frequencies shifted the location of the aggregate within the pressure node. As a result, manipulation of the sweep repetition rate changed the displacement path and

amplitude of the cell aggregate; however, manipulation of the electrical driving parameters did not significantly affect the streaming velocities within the fluid.

The stimulation created by dragging the cell agglomerate laterally at a rate determined by the sweep repetition rate has some key advantages. Acoustic stimulation of cells has been reported to be complex and multifaceted, resulting in the repair, proliferation, and differentiation of numerous cell types [139, 152, 258]. In this system, both the acoustic energy absorbed by the system (and hence any heating) as well as the acoustic streaming velocities are independent of the sweep repetition rate, providing a means to isolate the mechanical component of the resulting stimulation as well as tailor it for specific goals. The contact-less nature of the stimulation is in contrast to contact-based methods, which can reduce the surface area of the aggregate available for perfusion [75].

The bio-effects of modulating the acoustic field on human cartilage generation were determined by comprehensive immunohistochemical analyses of the cartilage constructs, generated as a result of 3-D, scaffold-free culture of HACs in the acoustofluidic bioreactor over a period of 21 days. This study found that a higher sweep rate (50 Hz), which produces less stimulation, resulted in sub-optimal cartilage formation. In contrast, a 2 Hz regime resulted in the generation of cartilaginous constructs exhibiting regions of hyaline-like structure, characterized by robust SOX-9 and Type II collagen expression. However, the constructs were also characterized by the conspicuous presence of collagen Type I and Type X, normally expressed in fibrous and hypertrophic cartilage, respectively. This suggested that, although mechanical stimulation as a result of application of the sweep repetition rate of 2 Hz elicited a favourable chondrogenic response from the cells, further parameter optimization was necessary to promote the formation of robust hyaline-like cartilage and to minimize hypertrophy.

To improve cartilage formation, in addition to manipulating the mechanical environment, culture of the HAC aggregates within the acoustic field was investigated in the presence of PTHrP, a growth factor with defined roles in promoting chondrogenesis and inhibiting hypertrophy, especially in presence of mechanical stimulation [228, 234, 235]. Notably, 21-day constructs generated in the bioreactor in chondrogenic media supplemented with PTHrP, using a sweep repetition rate of 2 Hz

were: i) appreciably larger in size, ii) exhibited distinct hyaline-like cartilage structure, iii) demonstrated robust expression of SOX-9 and Type II collagen, and, importantly, iv) displayed negligible expression of collagen Type I and Type X. Additionally, mechanical analysis of the cartilage tissue using nano-indentation showed the engineered human cartilage constructs to have stiffness similar to that of native human cartilage tissue.

My findings demonstrate the capability of acoustofluidics as a tunable biomechanical technology for the culture and development of hyaline-like human cartilage constructs *in vitro* and provide a new platform to investigate scaffold-free cartilage tissue engineering. Similarly to the work presented in this chapter, Schatti *et al.* implemented a parametric analysis study of compressive loading on chondrocytes, to which they found that the rate of stimulation and force magnitude affected the matrix composition of the tissue [259]. These results correspond to the results in this chapter, where I have examined and quantified the biomechanical stimulation applied by the acoustically derived periodic fluidic shear to aggregates, and presented how the matrix composition of the tissue differs between a driving sweep rate of 2 Hz and 50 Hz. The matrix composition was shown to be further improved through supplementation of the culture media with PTHrP with the 2 Hz stimulation regime.

It should be appreciated, however, that while the streaming velocities were characterized separately from the lateral displacement on the cells, the acoustic field simultaneously exerts these forces into the resonant cavity, meaning that the streaming patterns and forces, particularly at the lower sweep repetition rates, may be influenced by the oscillatory motion of the levitating aggregate. Specifically, the aggregate would encounter higher displacement amplitudes at lower sweep repetition rates, which may add a mixing element to the system, thus affecting the streaming patterns around the aggregate and potentially its influence on the cells. Furthermore, as discussed previously, the shear stresses on the cells were reported early in the tissue development cycle and may further change as the aggregate density increases and changes conformation with matrix production. In summary, there are likely to be other interacting forces at play during the culture period, and further characterization of the interaction between the acoustic environment and the cells will be carried out in the future work, along with assessment of changes in chondrogenic gene expression in response to the acoustic environment.

Chapter 6

Conclusion

The primary aim of this thesis was to investigate the biomechanical role of the ultrasonic wave field during cell culture and tissue development. To validate the role of the acoustic environment to produce robust hyaline-like cartilage, an investigation of an appropriate cell source was first pursued. Co-cultures of human primary chondrocytes and skeletal stem cells were maintained in ratios of 1:2, 1:1, and 2:1 under normoxic conditions. The tissue quality was assessed by histological staining for proteoglycans, SOX9, COLI, II, and X. Analysis of pellets from three patients showed that the HAC biased mixture provided the most ideal staining with respect to the other co-culture conditions and SSC control. However, the tissue quality of the HAC control pellets were consistently better than the co-culture pellets, suggesting limited interaction between the chondrocytes and stem cells. This was the first study to show co-culture of STRO-1+ SSCs with HACs and further shown that the stem cells were unable to generate robust hyaline cartilage, despite the addition of HACs into the population.

After determining an effective cell source, a new bioreactor design was pursued. A new acoustofluidic bioreactor was designed to be a high-throughput and to quantify the interactions and repeatability of the acoustic interactions with the cells. Previously, our group has shown the potential of an acoustofluidic bioreactor for the scaffold-free development of cartilaginous tissue [22]. Inconsistencies with the hardware occasionally led to inadequate tissue development. Specifically, bubble formation within the medium reservoir would result in perfusion and trapping of bubbles within the acoustic trap. Surface tension would then push cells out of the trap, leading to either a smaller

tissue construct or nothing at all. As microbubble formation is prevalent in microfluidic systems, the present research addressed this issue by redesigning the system to a open sided chamber, whereby resonators were immersed in culture media within a sterile cavity. This bioreactor also allowed the investigation of the mechanical environment created by the acoustic forces within the fluid cavity and its contributions to tissue development. These mechanical-based findings were compared against tissue development with chemical supplementation into the media to further investigate the influence of the physicochemical environment within the acoustofluidic bioreactor during tissue development.

I demonstrated that the acoustic forces applied onto the cells were able to be manipulated by the driving parameters from a signal generator, specifically the driving voltage, sweep repetition rate, and sweep range. The acoustic forces investigated in this study, which were thought to mechanically influence the cells, were the acoustic streaming forces and secondary radiation forces. The acoustic streaming forces measured in the present study allow for nutrient exchange around the developing tissue at velocities comparable to the perfusion culture previously reported [22]. The drag forces are controllable through the sweep range and voltage applied into the trap, given that the streaming velocities were significantly higher at a single frequency and unaffected when sweeping at different rates.

The mechanical characterization of these forces was linked to cartilage development through long-term tissue culture within the bioreactor. The results from this study found that a high sweep rate (50 Hz) resulted in sub-par cartilage formation, whilst a lower sweep rate (2 Hz) resulted in substantially more cartilage-specific matrix production and formation of a very hyaline-like structure, including lacunae. In addition to manipulating the mechanical environment, chondrocyte culture within the acoustic field was also investigated in the presence of PTHrP. It has been reported that PTHrP inhibits hypertrophy and further promotes chondrogenesis in chondrocytes, especially when mechanically stimulated [234, 235, 259]. To test the influence of PTHrP within the bioreactor, the chondrogenic media was supplemented with the growth factor mid-way through a 2 Hz culture within the acoustofluidic bioreactor. It was observed that the structure of the tissue was greatly promoted to better define the lacunae, which was reproducible within multiple patient sets.

The work accomplished in this thesis provides a preliminary understanding into how modulation of the acoustic environment may yield bio-mechanically relevant forces for cartilage engineering. Future work would focus on (1) further refining the bioreactor system, (2) a deeper understanding of how the acoustic forces stimulate the cells—both in the short term and long term—(3) as well as extending the application of this bioacoustofluidics system for use with other cell/tissue types and the generation of tissue models for other bioengineering applications.

The acoustofluidic bioreactor system presented in this thesis was used to levitate and stimulate chondrocytes using a combination of acoustic radiation and streaming forces. As streaming stems from the acoustic energy attenuation into the fluid, it would not be possible to separately determine the biological contribution of the radiation and streaming forces. An analogue system may be developed to assess streaming-like forces on a spatially fixed aggregate to simulate levitation. Additionally, mesenchymal/skeletal stem cell culture within the resonator can be explored to compare against the pellet culture model results as discussed in Chapter 3. Considering that a different cell type may react differently to the incident shear stress, further evaluation of the sweep repetition rate and the shear magnitude applied onto the cells would be required to ensure an optimal mechanical stimulation regime to induce differentiation down the appropriate lineage. Furthermore, as discussed by Fischer *et al.*, optimization of biochemical factor interaction with the cells and developing cells may be required to limit an adverse reaction from the cells (such as hypertrophy), while maintaining and improving the expression of desired markers [236]. Literature has also presented application of acoustic trap for the engineering of vascular [19–21, 73] and neuronal [24] tissue models; however, engineering either more clinically relevant tissue or more complex tissue structure, such as osteochondral or aortic tissue, would require a more complicated bioreactor design to permit culture and integration of multiple cell types.

The concept presented in this thesis of a layered resonator for acoustic stimulation and levitation can be expanded on to design a more efficient system for cell and tissue culture. The system design presented in this thesis is sufficient for a preliminary investigation to cartilage engineering, however, it should be appreciated that the output constructs are not of a clinically relevant size for implantation. Development of a larger construct may be possible by transitioning from a layered resonator system to

a transverse resonator or a Scholte-wave system [260]. The primary benefit of these system types over a layered resonator structure is that the acoustic wave propagation occurs perpendicular to the transducer face, where a transverse standing wave field propagates through the bulk of the fluid and a Scholte wave is generated near the surface of the carrier layer [261] and would allow for the development of an open well system, such as the transverse well-plate design reported by Christakou *et al.* [183]. An open well-type system would allow for improved culture maintenance, identification and acquisition of the growing tissue construct at different time points, which would allow for further assessment of the biomechanical relevance of the acoustic trap for stimulating the cells. It should be appreciated, however, that the mechanistic differences in how the acoustic trap is generated between a layered resonator, transverse, and Scholte wave system may change the driving parameters needed to assemble viable aggregates to develop into robust cartilage from the bioreactor and comprehensive re-characterization of the culture environment would be required.

Considering the limited understanding of the mechanotransduction pathways involved in acoustofluidic cell stimulation, a further extension from this thesis work would involve improved parametric analysis into the characterization and influence of the acoustic forces, both laterally and axially, on levitating cells. This may be accomplished via super resolution microscopy to better visualize the cell membrane and potential changes to its morphology and how the deformation may translate into a stimulating force. The lipid order imaging investigation would provide some insight into the short-term (day 0) response of the cells to the acoustic stimulation and can be linked to a quantitative gene expression analysis with cells acoustically stimulated at high (20–50 Hz) and low (1–5 Hz) sweep repetition rates cultured to day 1–5 within the resonator. In addition to this change in the lipid order, Bazou *et al.* previously reported actin stress fibre formation and the relevance of gap junction formation for promoting cell-cell interactions in levitation [180, 184]. Additionally, G-protein couple receptors (GPCRs) and subsequently Rho kinase activation and F-actin polymerization have been extensively reported to be associated with fluid shear-based stimulation [262–264]. These proteins are further associated with the Hippo signalling pathway, which also includes yes-associated protein (YAP)—a transcriptional regulator reported to be linked to mediating mechanical cues from the cellular microenvironment in MSCs and regulated by different shear flow patterns in endothelial cells [265–268].

Given that YAP functions by translocating from the cytoplasm to the nucleus to activate genes upon mechanical stimuli, gene expression analysis by real time quantitative-polymerase chain reaction (RT-qPCR) of YAP targets, such as connective tissue growth factor (CTGF) and cysteine-rich angiogenic inducer 61 (Cyr61) [268–270]. Both CTGF and Cyr61 have been implicated in cellular response to shear stress [270]. To further provide insight into how acoustic environment affects the cells, Western Blotting of the nuclear and cytoplasmic protein fractions from cells driven at different regimes can provide evidence of YAP nuclear accumulation upon receiving stimuli. Immunofluorescence staining of YAP in cells stimulated at high and low sweep rates, using non-stimulated cells as control, would allow visualization and quantification of YAP nuclear intensity upon stimulation. Furthermore, actin polymerisation and dynamics can be studied with the use of fluorescently-tagged actin constructs or LifeACT constructs to specifically label F-actin. Fluorescent small molecule probes such as Spirochrome probes with high specificity for F-actin can also be useful for this purpose.

In summary, this research presents an initial assessment to the biomechanical relevance of acoustofluidics for engineering tissue. While the physical system described in this thesis proved to be limited, further optimization of the system design and exploration of new bioreactor systems, as well as elucidating the biomechanical signalling involved in acoustic-cell interactions may yield an improved foundation for acoustically enhanced tissue engineering.

References

[1] N. W. Choi, M. Cabodi, B. Held, J. P. Gleghorn, L. J. Bonassar, and A. D. Stroock, "Microfluidic scaffolds for tissue engineering," *Nature Materials*, vol. 6, no. 11, pp. 908–15, 2007.

[2] R. M. Schek, J. M. Taboas, S. J. Segvich, S. J. Hollister, and P. H. Krebsbach, "Engineered osteochondral grafts using biphasic composite solid free-form fabricated scaffolds," *Tissue Engineering*, vol. 10, no. 9-10, pp. 1376–85, 2004.

[3] J. S. Temenoff and A. G. Mikos, "Review: tissue engineering for regeneration of articular cartilage," *Biomaterials*, vol. 21, no. 5, pp. 431–40, 2000.

[4] R. Langer and J. Vacanti, "Tissue engineering," *Science*, vol. 260, no. 5110, pp. 920–926, 1993.

[5] A. Khademhosseini, R. Langer, J. Borenstein, and J. P. Vacanti, "Microscale technologies for tissue engineering and biology," *Proceedings of the National academy of Sciences of the United States of America*, vol. 103, no. 8, pp. 2480–7, 2006.

[6] H. Da, S. J. Jia, G. L. Meng, J. H. Cheng, W. Zhou, Z. Xiong, Y. J. Mu, and J. Liu, "The impact of compact layer in biphasic scaffold on osteochondral tissue engineering," *PLOS ONE*, vol. 8, no. 1, p. e54838, 2013.

[7] Y. Ishihara, K. Ueki, M. Sotobori, K. Marukawa, and A. Moroi, "Bone regeneration by statin and low-intensity pulsed ultrasound (lipus) in rabbit nasal bone," *Journal of Cranio-Maxillo-Facial Surgery*, 2013.

[8] T. Xu, K. W. Binder, M. Z. Albanna, D. Dice, W. Zhao, J. J. Yoo, and A. Atala, "Hybrid printing of mechanically and biologically improved constructs for cartilage tissue engineering applications," *Biofabrication*, vol. 5, no. 1, p. 015001, 2013.

[9] I. T. Ozbolat and Y. Yu, "Bioprinting toward organ fabrication: challenges and future trends," *IEEE Transactions on Biomedical Engineering*, vol. 60, no. 3, pp. 691–9, 2013.

[10] K. C. Hribar, P. Soman, J. Warner, P. Chung, and S. Chen, "Light-assisted direct-write of 3D functional biomaterials," *Lab on a Chip*, vol. 14, no. 2, pp. 268–75, 2014.

[11] M.-H. Wu, H.-Y. Wang, C.-L. Tai, Y.-H. Chang, Y.-M. Chen, S.-B. Huang, T.-K. Chiu, T.-C. Yang, and S.-S. Wang, "Development of perfusion-based microbioreactor platform capable of providing tunable dynamic compressive loading to 3-D cell culture construct: Demonstration study of the effect of compressive stimulations on articular chondrocyte functions," *Sensors and Actuators B: Chemical*, vol. 176, pp. 86–96, 2013.

[12] B. Labbe, G. Marceau-Fortier, and J. Fradette, "Cell sheet technology for tissue engineering: the self-assembly approach using adipose-derived stromal cells," *Methods in Molecular Biology*, vol. 702, pp. 429–41, 2011.

[13] M. Sato, M. Yamato, K. Hamahashi, T. Okano, and J. Mochida, "Articular cartilage regeneration using cell sheet technology," *The Anatomical Record*, vol. 297, no. 1, pp. 36–43, 2014.

[14] S. P. Nukavarapu and D. L. Dorcemus, "Osteochondral tissue engineering: current strategies and challenges," *Biotechnology Advances*, vol. 31, no. 5, pp. 706–21, 2013.

[15] G. VunjakNovakovic, I. Martin, B. Obradovic, S. Treppo, A. J. Grodzinsky, R. Langer, and L. E. Freed, "Bioreactor cultivation conditions modulate the composition and mechanical properties of tissueengineered cartilage," *Journal of Orthopaedic Research*, vol. 17, no. 1, pp. 130–138, 2016.

[16] A. J. Grodzinsky, M. E. Levenston, M. Jin, and E. H. Frank, "Cartilage tissue remodeling in response to mechanical forces," *Annual review of biomedical engineering*, vol. 2, no. 1, pp. 691–713, 2000.

[17] H. Ogawa, E. Kozhemyakina, H.-H. Hung, A. J. Grodzinsky, and A. B. Lassar, "Mechanical motion promotes expression of prg4 in articular cartilage via multiple

creb-dependent, fluid flow shear stress-induced signaling pathways," *Genes and Development*, 2014.

[18] D. Bazou, A. Castro, and M. Hoyos, "Controlled cell aggregation in a pulsed acoustic field," *Ultrasonics*, vol. 52, no. 7, pp. 842–50, 2012.

[19] K. A. Garvin, D. C. Hocking, and D. Dalecki, "Controlling the spatial organization of cells and extracellular matrix proteins in engineered tissues using ultrasound standing wave fields," *Ultrasound in medicine & biology*, vol. 36, no. 11, pp. 1919–1932, 2010.

[20] K. A. Garvin, J. VanderBurgh, D. C. Hocking, and D. Dalecki, "Controlling collagen fiber microstructure in three-dimensional hydrogels using ultrasound," *The Journal of the Acoustical Society of America*, vol. 134, no. 2, pp. 1491–1502, 2013.

[21] K. A. Garvin, D. Dalecki, M. Yousefhussien, M. Helguera, and D. C. Hocking, "Spatial patterning of endothelial cells and vascular network formation using ultrasound standing wave fields," *The Journal of the Acoustical Society of America*, vol. 134, no. 2, pp. 1483–1490, 2013.

[22] S. Li, P. Glynne-Jones, O. G. Andriotis, K. Y. Ching, U. S. Jonnalagadda, R. O. Oreffo, M. Hill, and R. S. Tare, "Application of an acoustofluidic perfusion bioreactor for cartilage tissue engineering," *Lab on a Chip*, 2014.

[23] J. Liu, L. A. Kuznetsova, G. O. Edwards, J. Xu, M. Ma, W. M. Purcell, S. K. Jackson, and W. T. Coakley, "Functional three-dimensional hepg2 aggregate cultures generated from an ultrasound trap: Comparison with hepg2 spheroids," *Journal of Cellular Biochemistry*, vol. 102, no. 5, pp. 1180–9, 2007.

[24] C. Bouyer, P. Chen, S. Guven, T. T. Demirtas, T. J. Nieland, F. Padilla, and U. Demirci, "A bio-acoustic levitational (bal) assembly method for engineering of multilayered, 3D brain-like constructs, using human embryonic stem cell derived neuro-progenitors," *Advanced Materials*, vol. 28, no. 1, pp. 161–7, 2016.

[25] P. Mishra, M. Hill, and P. Glynne-Jones, "Acoustic deformation of cells," in *Proceedings of Meetings on Acoustics*, vol. 19, p. 045013, Acoustical Society of America, 2013.

[26] A. M. Bhosale and J. B. Richardson, "Articular cartilage: structure, injuries and review of management," *British Medical Bulletin*, vol. 87, pp. 77–95, 2008.

[27] T. J. Klein, J. Malda, R. L. Sah, and D. W. Hutmacher, "Tissue engineering of articular cartilage with biomimetic zones," *Tissue Eng Part B Rev*, vol. 15, no. 2, pp. 143–57, 2009.

[28] M. B. Goldring and K. B. Marcu, "Cartilage homeostasis in health and rheumatic diseases," *Arthritis Research and Therapy*, vol. 11, no. 3, p. 224, 2009.

[29] K. R. Vincent, B. P. Conrad, B. J. Fregly, and H. K. Vincent, "The pathophysiology of osteoarthritis: a mechanical perspective on the knee joint," *PM R*, vol. 4, no. 5 Suppl, pp. S3–9, 2012.

[30] P. K. Sacitharan, S. J. Snelling, and J. R. Edwards, "Aging mechanisms in arthritic disease," *Discovery Medicine*, vol. 14, no. 78, pp. 345–52, 2012.

[31] S. N. Redman, S. F. Oldfield, and C. W. Archer, "Current strategies for articular cartilage repair," *European Cells and Materials*, vol. 9, pp. 23–32, 2005.

[32] J. K. Sherwood, S. L. Riley, R. Palazzolo, S. C. Brown, D. C. Monkhouse, M. Coates, L. G. Griffith, L. K. Landeen, and A. Ratcliffe, "A three-dimensional osteochondral composite scaffold for articular cartilage repair," *Biomaterials*, vol. 23, no. 24, pp. 4739–51, 2002.

[33] A. Panagopoulos, L. van Niekerk, and I. Triantafillopoulos, "Autologous chondrocyte implantation for knee cartilage injuries: moderate functional outcome and performance in patients with high-impact activities," *Orthopedics*, vol. 35, no. 1, pp. e6–14, 2012.

[34] G. Bentley, L. Biant, S. Vijayan, S. Macmull, J. Skinner, and R. Carrington, "Minimum ten-year results of a prospective randomised study of autologous chondrocyte implantation versus mosaicplasty for symptomatic articular cartilage lesions of the knee," *Journal of Bone & Joint Surgery, British Volume*, vol. 94, no. 4, pp. 504–509, 2012.

[35] W. Bartlett, J. A. Skinner, C. R. Gooding, R. W. Carrington, A. M. Flanagan, T. W. Briggs, and G. Bentley, "Autologous chondrocyte implantation versus matrix-induced autologous chondrocyte implantation for osteochondral defects of

the knee: a prospective, randomised study," *Journal of Bone and Joint Surgery. British Volume*, vol. 87, no. 5, pp. 640–5, 2005.

[36] A. Sionkowska, "Current research on the blends of natural and synthetic polymers as new biomaterials: Review," *Progress in polymer science*, vol. 36, no. 9, pp. 1254–1276, 2011.

[37] B. Dhandayuthapani, Y. Yoshida, T. Maekawa, and D. S. Kumar, "Polymeric scaffolds in tissue engineering application: a review," *International Journal of Polymer Science*, vol. 2011, 2011.

[38] A. Hoppe, N. S. Güldal, and A. R. Boccaccini, "A review of the biological response to ionic dissolution products from bioactive glasses and glass-ceramics," *Biomaterials*, vol. 32, no. 11, pp. 2757–2774, 2011.

[39] M. Ramalingam, E. Jabbari, S. Ramakrishna, and A. Khademhosseini, *Micro and Nanotechnologies in Engineering Stem Cells and Tissues*, vol. 39. John Wiley & Sons, 2013.

[40] G. Chen, T. Sato, J. Tanaka, and T. Tateishi, "Preparation of a biphasic scaffold for osteochondral tissue engineering," *Materials Science and Engineering: C*, vol. 26, no. 1, pp. 118–123, 2006.

[41] Y. M. Ju, J. S. Choi, A. Atala, J. J. Yoo, and S. J. Lee, "Bilayered scaffold for engineering cellularized blood vessels," *Biomaterials*, vol. 31, no. 15, pp. 4313–4321, 2010.

[42] C. Norotte, F. S. Marga, L. E. Niklason, and G. Forgacs, "Scaffold-free vascular tissue engineering using bioprinting," *Biomaterials*, vol. 30, no. 30, pp. 5910–7, 2009.

[43] K. Jakab, C. Norotte, B. Damon, F. Marga, A. Neagu, C. L. Besch-Williford, A. Kachurin, K. H. Church, H. Park, V. Mironov, R. Markwald, G. Vunjak-Novakovic, and G. Forgacs, "Tissue engineering by self-assembly of cells printed into topologically defined structures," *Tissue Engineering Part A*, vol. 14, no. 3, pp. 413–21, 2008.

[44] J. M. Kelm and M. Fussenegger, "Scaffold-free cell delivery for use in regenerative medicine," *Adv Drug Deliv Rev*, vol. 62, no. 7-8, pp. 753–64, 2010.

[45] J. M. Kelm, V. Lorber, J. G. Snedeker, D. Schmidt, A. Broggini-Tenzer, M. Weisstanner, B. Odermatt, A. Mol, G. Zund, and S. P. Hoerstrup, "A novel concept for scaffold-free vessel tissue engineering: self-assembly of microtissue building blocks," *Journal of Biotechnology*, vol. 148, no. 1, pp. 46–55, 2010.

[46] B. Mohanraj, A. J. Farran, R. L. Mauck, and G. R. Dodge, "Time-dependent functional maturation of scaffold-free cartilage tissue analogs," *Journal of biomechanics*, 2013.

[47] C. C. Chang, E. D. Boland, S. K. Williams, and J. B. Hoying, "Direct-write bioprinting three-dimensional biohybrid systems for future regenerative therapies," *Journal of Biomedical Materials Research. Part B, Applied Biomaterials*, vol. 98, no. 1, pp. 160–70, 2011.

[48] B. Guillotin and F. Guillemot, "Cell patterning technologies for organotypic tissue fabrication," *Trends in Biotechnology*, vol. 29, no. 4, pp. 183–90, 2011.

[49] J. L. Drury and D. J. Mooney, "Hydrogels for tissue engineering: scaffold design variables and applications," *Biomaterials*, vol. 24, no. 24, pp. 4337–51, 2003.

[50] H. A. Awad, M. Q. Wickham, H. A. Leddy, J. M. Gimble, and F. Guilak, "Chondrogenic differentiation of adipose-derived adult stem cells in agarose, alginate, and gelatin scaffolds," *Biomaterials*, vol. 25, no. 16, pp. 3211–22, 2004.

[51] V. Karageorgiou and D. Kaplan, "Porosity of 3D biomaterial scaffolds and osteogenesis," *Biomaterials*, vol. 26, no. 27, pp. 5474–91, 2005.

[52] P. Zorlutuna, N. E. Vrana, and A. Khademhosseini, "The expanding world of tissue engineering: the building blocks and new applications of tissue engineered constructs," *IEEE Reviews in Biomedical Engineering*, vol. 6, pp. 47–62, 2013.

[53] W. Ando, K. Tateishi, D. A. Hart, D. Katakai, Y. Tanaka, K. Nakata, J. Hashimoto, H. Fujie, K. Shino, H. Yoshikawa, and N. Nakamura, "Cartilage repair using an in vitro generated scaffold-free tissue-engineered construct derived from porcine synovial mesenchymal stem cells," *Biomaterials*, vol. 28, no. 36, pp. 5462–70, 2007.

[54] H. Takahashi, N. Matsuzaka, M. Nakayama, A. Kikuchi, M. Yamato, and T. Okano, "Terminally functionalized thermoresponsive polymer brushes for simultaneously promoting cell adhesion and cell sheet harvest," *Biomacromolecules*, vol. 13, no. 1, pp. 253–260, 2012.

[55] H. Takahashi, M. Nakayama, T. Shimizu, M. Yamato, and T. Okano, "Anisotropic cell sheets for constructing three-dimensional tissue with well-organized cell orientation," *Biomaterials*, vol. 32, no. 34, pp. 8830–8838, 2011.

[56] S. A. Skoog, P. L. Goering, and R. J. Narayan, "Stereolithography in tissue engineering," *Journal of Materials Science: Materials in Medicine*, vol. 25, no. 3, pp. 845–56, 2014.

[57] T. Kimura, Y. Sato, F. Kimura, M. Iwasaka, and S. Ueno, "Micropatterning of cells using modulated magnetic fields," *Langmuir*, vol. 21, no. 3, pp. 830–2, 2005.

[58] C. C. Wang, K. C. Yang, K. H. Lin, H. C. Liu, and F. H. Lin, "A highly organized three-dimensional alginate scaffold for cartilage tissue engineering prepared by microfluidic technology," *Biomaterials*, vol. 32, no. 29, pp. 7118–26, 2011.

[59] L. A. Hockaday, K. H. Kang, N. W. Colangelo, P. Y. Cheung, B. Duan, E. Malone, J. Wu, L. N. Girardi, L. J. Bonassar, H. Lipson, C. C. Chu, and J. T. Butcher, "Rapid 3D printing of anatomically accurate and mechanically heterogeneous aortic valve hydrogel scaffolds," *Biofabrication*, vol. 4, no. 3, p. 035005, 2012.

[60] S. Chung, R. Sudo, V. Vickerman, I. K. Zervantonakis, and R. D. Kamm, "Microfluidic platforms for studies of angiogenesis, cell migration, and cell-cell interactions," *Annals of Biomedical Engineering*, vol. 38, no. 3, pp. 1164–1177, 2010.

[61] R. Gauvin, Y.-C. Chen, J. W. Lee, P. Soman, P. Zorlutuna, J. W. Nichol, H. Bae, S. Chen, and A. Khademhosseini, "Microfabrication of complex porous tissue engineering scaffolds using 3D projection stereolithography," *Biomaterials*, vol. 33, no. 15, pp. 3824–3834, 2012.

[62] S. Guven, P. Chen, F. Inci, S. Tasoglu, B. Erkmen, and U. Demirci, "Multiscale assembly for tissue engineering and regenerative medicine," *Trends in biotechnology*, vol. 33, no. 5, pp. 269–279, 2015.

[63] Y. Zheng, J. Chen, M. Craven, N. W. Choi, S. Totorica, A. Diaz-Santana, P. Kermani, B. Hempstead, C. Fischbach-Teschl, J. A. López, *et al.*, "In vitro microvessels for the study of angiogenesis and thrombosis," *Proceedings of the National Academy of Sciences*, vol. 109, no. 24, pp. 9342–9347, 2012.

[64] J. He, R. Chen, Y. Lu, L. Zhan, Y. Liu, D. Li, and Z. Jin, "Fabrication of circular microfluidic network in enzymatically-crosslinked gelatin hydrogel," *Materials Science and Engineering: C*, vol. 59, pp. 53–60, 2016.

[65] J. M. Chan, I. K. Zervantonakis, T. Rimchala, W. J. Polacheck, J. Whisler, and R. D. Kamm, "Engineering of in vitro 3D capillary beds by self-directed angiogenic sprouting," *PLOS ONE*, vol. 7, no. 12, p. e50582, 2012.

[66] Y. K. Park, T.-Y. Tu, S. H. Lim, I. J. Clement, S. Y. Yang, and R. D. Kamm, "In vitro microvessel growth and remodeling within a three-dimensional microfluidic environment," *Cellular and molecular bioengineering*, vol. 7, no. 1, pp. 15–25, 2014.

[67] H. Mulvana, S. Cochran, and M. Hill, "Ultrasound assisted particle and cell manipulation on-chip," *Adv Drug Deliv Rev*, 2013.

[68] Y. Qiu, C. Zhang, J. Tu, and D. Zhang, "Microbubble-induced sonoporation involved in ultrasound-mediated DNA transfection in vitro at low acoustic pressures," *Journal of Biomechanics*, vol. 45, no. 8, pp. 1339–1345, 2012.

[69] F. Padilla, R. Puts, L. Vico, and K. Raum, "Stimulation of bone repair with ultrasound: A review of the possible mechanic effects," *Ultrasonics*, vol. 54, no. 5, pp. 1125–1145, 2014.

[70] M. Groschl, "Ultrasonic separation of suspended particles-part i: Fundamentals," *Acta Acustica*, vol. 84, pp. 432–447, 1998.

[71] M. Weiser, R. Apfel, and E. Neppiras, "Interparticle forces on red cells in a standing wave field," *Acta Acustica united with Acustica*, vol. 56, no. 2, pp. 114–119, 1984.

[72] H. Bruus, "Acoustofluidics 7: The acoustic radiation force on small particles," *Lab on a Chip*, vol. 12, no. 6, pp. 1014–1021, 2012.

[73] K. A. Garvin, D. Dalecki, and D. C. Hocking, "Vascularization of three-dimensional collagen hydrogels using ultrasound standing wave fields," *Ultrasound in Medicine & Biology*, vol. 37, no. 11, pp. 1853–1864, 2011.

[74] D. Bazou, R. Kearney, F. Mansergh, C. Bourdon, J. Farrar, and M. Wride, "Gene expression analysis of mouse embryonic stem cells following levitation in an ultrasound standing wave trap," *Ultrasound in Medicine and Biology*, vol. 37, no. 2, pp. 321–330, 2011.

[75] M. Evander, L. Johansson, T. Lilliehorn, J. Piskur, M. Lindvall, S. Johansson, M. Almqvist, T. Laurell, and J. Nilsson, "Noninvasive acoustic cell trapping in a microfluidic perfusion system for online bioassays," *Analytical Chemistry*, vol. 79, no. 7, pp. 2984–91, 2007.

[76] L. A. Crum, "Bjerknes forces on bubbles in a stationary sound field," *The Journal of the Acoustical Society of America*, vol. 57, no. 6, pp. 1363–1370, 1975.

[77] G. O. Edwards, W. T. Coakley, J. R. Ralphs, and C. W. Archer, "Modelling condensation and the initiation of chondrogenesis in chick wing bud mesenchymal cells levitated in an ultrasound trap," *European Cells and Materials*, vol. 19, pp. 1–12, 2010.

[78] M. Wiklund, S. Radel, and J. J. Hawkes, "Acoustofluidics 21: ultrasound-enhanced immunoassays and particle sensors," *Lab on a Chip*, vol. 13, no. 1, pp. 25–39, 2013.

[79] M. Hill and N. R. Harris, "Ultrasonic microsystems for bacterial cell manipulation," in *Principles of Bacterial Detection: Biosensors, Recognition Receptors and Microsystems*, pp. 909–928, Springer, 2008.

[80] M. Wiklund, R. Green, and M. Ohlin, "Acoustofluidics 14: Applications of acoustic streaming in microfluidic devices," *Lab on a Chip*, vol. 12, no. 14, pp. 2438–2451, 2012.

[81] J. Lei, P. Glynne-Jones, and M. Hill, "Acoustic streaming in the transducer plane in ultrasonic particle manipulation devices," *Lab on a Chip*, vol. 13, no. 11, pp. 2133–2143, 2013.

[82] A. Bernassau, P. Glynne-Jones, F. Gesellchen, M. Riehle, M. Hill, and D. Cumming, "Controlling acoustic streaming in an ultrasonic heptagonal tweezers with application to cell manipulation," *Ultrasonics*, vol. 54, no. 1, pp. 268–274, 2014.

[83] T. M. Squires and S. R. Quake, "Microfluidics: Fluid physics at the nanoliter scale," *Reviews of modern physics*, vol. 77, no. 3, p. 977, 2005.

[84] J. Spengler, W. Coakley, and K. Christensen, "Microstreaming effects on particle concentration in an ultrasonic standing wave," *AIChE journal*, vol. 49, no. 11, pp. 2773–2782, 2003.

[85] L. A. Kuznetsova and W. T. Coakley, "Microparticle concentration in short path length ultrasonic resonators: Roles of radiation pressure and acoustic streaming," *The Journal of the Acoustical Society of America*, vol. 116, no. 4, pp. 1956–1966, 2004.

[86] L. A. Kuznetsova, S. P. Martin, and W. T. Coakley, "Sub-micron particle behaviour and capture at an immuno-sensor surface in an ultrasonic standing wave," *Biosensors and Bioelectronics*, vol. 21, no. 6, pp. 940–948, 2005.

[87] C. Devendran, I. Gralinski, and A. Neild, "Separation of particles using acoustic streaming and radiation forces in an open microfluidic channel," *Microfluidics and Nanofluidics*, vol. 17, no. 5, pp. 879–890, 2014.

[88] M. Ohlin, A. E. Christakou, T. Frisk, Ö. Björn, and M. Wiklund, "Influence of acoustic streaming on ultrasonic particle manipulation in a 100-well ring-transducer microplate," *Journal Of Micromechanics And Microengineering*, vol. 23, no. 3, p. 035008, 2013.

[89] K. G. Baker, V. J. Robertson, and F. A. Duck, "A review of therapeutic ultrasound: biophysical effects," *Physical Therapy*, vol. 81, no. 7, pp. 1351–8, 2001.

[90] L. A. Kuznetsova and W. T. Coakley, "Applications of ultrasound streaming and radiation force in biosensors," *Biosensors and Bioelectronics*, vol. 22, no. 8, pp. 1567–77, 2007.

[91] M. Wiklund, "Acoustofluidics 12: Biocompatibility and cell viability in microfluidic acoustic resonators," *Lab on a Chip*, vol. 12, no. 11, pp. 2018–2028, 2012.

[92] D. Dalecki, "Mechanical bioeffects of ultrasound," *Annual Review of Biomedical Engineering*, vol. 6, pp. 229–248, 2004.

[93] M. F. Hamilton, Y. A. Ilinskii, and E. A. Zabolotskaya, "Thermal effects on acoustic streaming in standing waves," *The Journal of the Acoustical Society of America*, vol. 114, no. 6, pp. 3092–3101, 2003.

[94] P. B. Muller, M. Rossi, A. G. Marin, R. Barnkob, P. Augustsson, T. Laurell, C. J. Kahler, and H. Bruus, "Ultrasound-induced acoustophoretic motion of microparticles in three dimensions," *Phys. Rev. E*, vol. 88, p. 023006, Aug. 2013.

[95] E. S. Ebbini and G. Ter Haar, "Ultrasound-guided therapeutic focused ultrasound: current status and future directions," *International Journal of Hyperthermia*, vol. 31, no. 2, pp. 77–89, 2015.

[96] R. Mettin, I. Akhatov, U. Parlitz, C. Ohl, and W. Lauterborn, "Bjerknes forces between small cavitation bubbles in a strong acoustic field," *Physical review E*, vol. 56, no. 3, p. 2924, 1997.

[97] I. Lentacker, I. De Cock, R. Deckers, S. De Smedt, and C. Moonen, "Understanding ultrasound induced sonoporation: Definitions and underlying mechanisms," *Advanced drug delivery reviews*, vol. 72, pp. 49–64, 2014.

[98] M. Bazan-Peregrino, C. D. Arvanitis, B. Rifai, L. W. Seymour, and C.-C. Coussios, "Ultrasound-induced cavitation enhances the delivery and therapeutic efficacy of an oncolytic virus in an in vitro model," *Journal of Controlled Release*, vol. 157, no. 2, pp. 235–242, 2012.

[99] J. J. Choi, J. A. Feshitan, B. Baseri, S. Wang, Y.-S. Tung, M. A. Borden, and E. E. Konofagou, "Microbubble-size dependence of focused ultrasound-induced blood–brain barrier opening in mice in vivo," *Biomedical Engineering, IEEE Transactions on*, vol. 57, no. 1, pp. 145–154, 2010.

[100] Z. Kyriakou, M. I. Corral-Baques, A. Amat, and C.-C. Coussios, "Hifu-induced cavitation and heating in ex vivo porcine subcutaneous fat," *Ultrasound in Medicine & Biology*, vol. 37, no. 4, pp. 568–579, 2011.

[101] J. Kwan, G. Lajoinie, N. de Jong, E. Stride, M. Versluis, and C. Coussios, "Ultrahigh-speed dynamics of micrometer-scale inertial cavitation from nanoparticles," *Physical review applied*, vol. 6, no. 4, p. 044004, 2016.

[102] D. Carugo, D. N. Ankrett, P. Glynne-Jones, L. Capretto, R. J. Boltryk, X. Zhang, P. A. Townsend, and M. Hill, "Contrast agent-free sonoporation: The use of an ultrasonic standing wave microfluidic system for the delivery of pharmaceutical agents," *Biomicrofluidics*, vol. 5, no. 4, p. 044108, 2011.

[103] Y. H. Lee and C. A. Peng, "Enhanced retroviral gene delivery in ultrasonic standing wave fields," *Gene Therapy*, vol. 12, no. 7, pp. 625–33, 2005.

[104] Y. Sakakima, S. Hayashi, Y. Yagi, A. Hayakawa, K. Tachibana, and A. Nakao, "Gene therapy for hepatocellular carcinoma using sonoporation enhanced by contrast agents," *Cancer Gene Therapy*, vol. 12, no. 11, pp. 884–889, 2005.

[105] G. ter Haar, "Therapeutic applications of ultrasound," *Progress in Biophysics and Molecular biology*, vol. 93, no. 1-3, pp. 111–29, 2007.

[106] B.-H. Min, B. H. Choi, and S. R. Park, "Low intensity ultrasound as a supporter of cartilage regeneration and its engineering," *Biotechnology and Bioprocess Engineering*, vol. 12, no. 1, pp. 22–31, 2007.

[107] K. Erikson, F. Fry, and J. Jones, "Ultrasound in medicine-a review," *IEEE Transactions on Sonics and Ultrasonics*, vol. 21, no. 3, pp. 144–170, 1974.

[108] W. L. Nyborg, "Biological effects of ultrasound: Development of safety guidelines. part ii: General review," *Ultrasound in Medicine and Biology*, vol. 27, no. 3, pp. 301–333, 2001.

[109] B. H. Min, J. I. Woo, H. S. Cho, B. H. Choi, S. J. Park, M. J. Choi, and S. R. Park, "Effects of low-intensity ultrasound (lius) stimulation on human cartilage explants," *Scandinavian Journal of Rheumatology*, vol. 35, no. 4, pp. 305–11, 2006.

[110] W. Cui, S. Tavri, M. J. Benchimol, M. Itani, E. S. Olson, H. Zhang, M. Decyk, R. G. Ramirez, C. V. Barback, Y. Kono, and R. F. Mattrey, "Neural progenitor cells labeling with microbubble contrast agent for ultrasound imaging in vivo," *Biomaterials*, vol. 34, no. 21, pp. 4926–35, 2013.

[111] M. Schone, N. Mannicke, M. Gottwald, F. Gobel, and K. Raum, "3-d high-frequency ultrasound improves the estimation of surface properties in degenerated cartilage," *Ultrasound in Medicine and Biology*, vol. 39, no. 5, pp. 834–44, 2013.

[112] A. Karpiouk, S. Aglyamov, Y. Ilinskii, E. Zabolotskaya, and S. Emelianov, "Assessment of shear modulus of tissue using ultrasound radiation force acting on a spherical acoustic inhomogeneity," *Ultrasonics, Ferroelectrics and Frequency Control, IEEE Transactions on*, vol. 56, pp. 2380–2387, Nov. 2009.

[113] L. Chen and L. Liu, "Current progress and prospects of induced pluripotent stem cells," *Science in China. Series C, Life Sciences*, vol. 52, no. 7, pp. 622–36, 2009.

[114] H. J. Nieminen, S. Saarakkala, M. S. Laasanen, J. Hirvonen, J. S. Jurvelin, and J. Toyras, "Ultrasound attenuation in normal and spontaneously degenerated articular cartilage," *Ultrasound in Medicine and Biology*, vol. 30, no. 4, pp. 493–500, 2004.

[115] E. E. Drakonaki, G. M. Allen, and D. J. Wilson, "Ultrasound elastography for musculoskeletal applications," *British Journal of Radiology*, vol. 85, no. 1019, pp. 1435–45, 2012.

[116] N. M. Pounder and A. J. Harrison, "Low intensity pulsed ultrasound for fracture healing: a review of the clinical evidence and the associated biological mechanism of action," *Ultrasonics*, vol. 48, no. 4, pp. 330–338, 2008.

[117] H. Nieminen, A. Salmi, P. Karppinen, E. Hæggström, and S. Hacking, "The potential utility of high-intensity ultrasound to treat osteoarthritis," *Osteoarthritis and Cartilage*, vol. 22, no. 11, pp. 1784–1799, 2014.

[118] K. Cheng, P. Xia, Q. Lin, S. Shen, M. Gao, S. Ren, and X. Li, "Effects of low-intensity pulsed ultrasound on integrin-fak-pi3K/akt mechanochemical transduction in rabbit osteoarthritis chondrocytes," *Ultrasound in medicine & biology*, vol. 40, no. 7, pp. 1609–1618, 2014.

[119] R. Takeuchi, A. Ryo, N. Komitsu, Y. Mikuni-Takagaki, A. Fukui, Y. Takagi, T. Shiraishi, S. Morishita, Y. Yamazaki, K. Kumagai, *et al.*, "Low-intensity pulsed ultrasound activates the phosphatidylinositol 3 kinase/akt pathway and stimulates the growth of chondrocytes in three-dimensional cultures: a basic science study," *Arthritis research and therapy*, vol. 10, no. 4, p. R77, 2008.

[120] C.-H. Tang, R.-S. Yang, T.-H. Huang, D.-Y. Lu, W.-J. Chuang, T.-F. Huang, and W.-M. Fu, "Ultrasound stimulates cyclooxygenase-2 expression and increases bone formation through integrin, focal adhesion kinase, phosphatidylinositol 3-kinase, and akt pathway in osteoblasts," *Molecular pharmacology*, vol. 69, no. 6, pp. 2047–2057, 2006.

[121] P. H. Tsui, S. H. Wang, and C. C. Huang, "In vitro effects of ultrasound with different energies on the conduction properties of neural tissue," *Ultrasonics*, vol. 43, no. 7, pp. 560–5, 2005.

[122] S. Noriega, G. Hasanova, and A. Subramanian, "The effect of ultrasound stimulation on the cytoskeletal organization of chondrocytes seeded in three-dimensional matrices," *Cells, Tissues, Organs*, vol. 197, no. 1, pp. 14–26, 2013.

[123] V. F. Humphrey, "Ultrasound and matterphysical interactions," *Progress in biophysics and molecular biology*, vol. 93, no. 1, pp. 195–211, 2007.

[124] G. ter Haar, "Therapeutic ultrasound," *European Journal of Ultrasound*, vol. 9, no. 1, pp. 3–9, 1999.

[125] A. Bystritsky, A. S. Korb, P. K. Douglas, M. S. Cohen, W. P. Melega, A. P. Mulgaonkar, A. DeSalles, B. K. Min, and S. S. Yoo, "A review of low-intensity focused ultrasound pulsation," *Brain Stimul*, vol. 4, no. 3, pp. 125–36, 2011.

[126] D. Dalecki and D. C. Hocking, "Ultrasound technologies for biomaterials fabrication and imaging," *Annals of biomedical engineering*, pp. 1–15, 2014.

[127] G. ter Haar, A. Shaw, S. Pye, B. Ward, F. Bottomley, R. Nolan, and A.-M. Coady, "Guidance on reporting ultrasound exposure conditions for bio-effects studies," *Ultrasound in Medicine & Biology*, vol. 37, no. 2, pp. 177–183, 2011.

[128] Y. Lv, P. Zhao, G. Chen, Y. Sha, and L. Yang, "Effects of low-intensity pulsed ultrasound on cell viability, proliferation and neural differentiation of induced pluripotent stem cells-derived neural crest stem cells," *Biotechnology Letters*, 2013.

[129] W. Z. Chen, H. Qiao, W. Zhou, J. Wu, and Z. B. Wang, "Upgraded nerve growth factor expression induced by low-intensity continuous-wave ultrasound accelerates regeneration of neurotometicly injured sciatic nerve in rats," *Ultrasound in Medicine and Biology*, vol. 36, no. 7, pp. 1109–17, 2010.

[130] M. D. Menz, O. Oralkan, P. T. Khuri-Yakub, and S. A. Baccus, "Precise neural stimulation in the retina using focused ultrasound," *Journal of Neuroscience*, vol. 33, no. 10, pp. 4550–60, 2013.

[131] R. T. Mihran, F. S. Barnes, and H. Wachtel, "Temporally-specific modification of myelinated axon excitability in vitro following a single ultrasound pulse," *Ultrasound in Medicine and Biology*, vol. 16, no. 3, pp. 297–309, 1990.

[132] S. C. Park, S. H. Oh, T. B. Seo, U. Namgung, J. M. Kim, and J. H. Lee, "Ultrasound-stimulated peripheral nerve regeneration within asymmetrically porous plga/pluronic f127 nerve guide conduit," *Journal of Biomedical Materials Research. Part B, Applied Biomaterials*, vol. 94, no. 2, pp. 359–66, 2010.

[133] T. Watson, "Ultrasound in contemporary physiotherapy practice," *Ultrasonics*, vol. 48, no. 4, pp. 321–9, 2008.

[134] Y. Imai, T. Hasegawa, D. Takeda, M. Akashi, S. Y. Lee, T. Niikura, Y. Shibuya, M. Kurosaka, and T. Komori, "The osteogenic activity of human mandibular fracture haematoma-derived cells is stimulated by low-intensity pulsed ultrasound in vitro," *International Journal of Oral and Maxillofacial Surgery*, 2013.

[135] K. Lim, J. Kim, H. Seonwoo, S. H. Park, P.-H. Choung, and J. H. Chung, "In vitro effects of low-intensity pulsed ultrasound stimulation on the osteogenic differentiation of human alveolar bone-derived mesenchymal stem cells for tooth tissue engineering," *BioMed Research International*, vol. 2013, pp. 1–15, 2013.

[136] N. Vaughan, J. Grainger, D. Bader, and M. Knight, "The potential of pulsed low intensity ultrasound to stimulate chondrocytes matrix synthesis in agarose and monolayer cultures," *Medical and Biological Engineering and Computing*, pp. 1–8, 2010.

[137] P. A. Nolte, J. Klein-Nulend, G. H. Albers, R. K. Marti, C. M. Semeins, S. W. Goei, and E. H. Burger, "Low-intensity ultrasound stimulates endochondral ossification in vitro," *Journal of Orthopaedic Research*, vol. 19, no. 2, pp. 301–7, 2001.

[138] S. Angle, K. Sena, D. Sumner, and A. Virdi, "Osteogenic differentiation of rat bone marrow stromal cells by various intensities of low-intensity pulsed ultrasound," *Ultrasonics*, vol. 51, no. 3, pp. 281–288, 2011.

[139] C. H. Fung, W. H. Cheung, N. M. Pounder, F. J. de Ana, A. Harrison, and K. S. Leung, "Investigation of rat bone fracture healing using pulsed 1.5MHz, 30mW/cm(2) burst ultrasound - axial distance dependency," *Ultrasonics*, vol. 54, no. 3, pp. 850–9, 2014.

[140] K. Wien and D. Harder, "Characteristics of the pulsed ultrasound field.," *The British journal of cancer. Supplement*, vol. 5, p. 59, 1982.

[141] F.-Y. Wei, K.-S. Leung, G. Li, J. Qin, S. K.-H. Chow, S. Huang, M.-H. Sun, L. Qin, and W.-H. Cheung, "Low intensity pulsed ultrasound enhanced mesenchymal stem cell recruitment through stromal derived factor-1 Signaling in fracture healing," *PLOS ONE*, vol. 9, no. 9, p. e106722, 2014.

[142] J. Kusuyama, K. Bandow, M. Shamoto, K. Kakimoto, T. Ohnishi, and T. Matsuguchi, "Low intensity pulsed ultrasound (lipus) influences the multilineage differentiation of mesenchymal stem and progenitor cell lines through rock-cot/tpl2-mek-erk signaling pathway," *Journal of Biological Chemistry*, vol. 289, no. 15, pp. 10330–10344, 2014.

[143] K. Ebisawa, K.-i. Hata, K. Okada, K. Kimata, M. Ueda, S. Torii, and H. Watanabe, "Ultrasound enhances transforming growth factor β-mediated chondrocyte differentiation of human mesenchymal stem cells," *Tissue Engineering*, vol. 10, no. 5-6, pp. 921–929, 2004.

[144] S. R. Park, B. H. Choi, and B. H. Min, "Low-intensity ultrasound (lius) as an innovative tool for chondrogenesis of mesenchymal stem cells (mscs)," *Organogenesis*, vol. 3, no. 2, pp. 74–8, 2007.

[145] H. J. Lee, B. H. Choi, B. H. Min, Y. S. Son, and S. R. Park, "Low-intensity ultrasound stimulation enhances chondrogenic differentiation in alginate culture of mesenchymal stem cells," *Artificial Organs*, vol. 30, no. 9, pp. 707–15, 2006.

[146] J. H. Cui, S. R. Park, K. Park, B. H. Choi, and B. H. Min, "Preconditioning of mesenchymal stem cells with low-intensity ultrasound for cartilage formation in vivo," *Tissue Engineering*, vol. 13, no. 2, pp. 351–60, 2007.

[147] T. M. Louw, G. Budhiraja, H. J. Viljoen, and A. Subramanian, "Mechanotransduction of ultrasound is frequency dependent below the cavitation threshold," *Ultrasound in Medicine & Biology*, vol. 39, no. 7, pp. 1303–1319, 2013.

[148] S. R. Park, K. W. Jang, S. H. Park, H. S. Cho, C. Z. Jin, M. J. Choi, S. I. Chung, and B. H. Min, "The effect of sonication on simulated osteoarthritis. part i: effects of 1 MHz ultrasound on uptake of hyaluronan into the rabbit synovium," *Ultrasound in Medicine and Biology*, vol. 31, no. 11, pp. 1551–8, 2005.

[149] A. Subramanian, J. A. Turner, G. Budhiraja, S. G. Thakurta, N. P. Whitney, and S. S. Nudurupati, "Ultrasonic bioreactor as a platform for studying cellular response," *Tissue Engineering Part C-Methods*, vol. 19, no. 3, pp. 244–255, 2013.

[150] S. Noriega, G. Budhiraja, and A. Subramanian, "Remodeling of chromatin under low intensity diffuse ultrasound," *The international journal of biochemistry & cell biology*, vol. 44, no. 8, pp. 1331–1336, 2012.

[151] G. I. Hasanova, S. E. Noriega, T. G. Mamedov, S. Guha Thakurta, J. A. Turner, and A. Subramanian, "The effect of ultrasound stimulation on the gene and protein expression of chondrocytes seeded in chitosan scaffolds," *Journal of Tissue Engineering and Regenerative Medicine*, vol. 5, no. 10, pp. 815–22, 2011.

[152] N. P. Whitney, A. C. Lamb, T. M. Louw, and A. Subramanian, "Integrin-mediated mechanotransduction pathway of low-intensity continuous ultrasound in human chondrocytes," *Ultrasound in Medicine and Biology*, vol. 38, no. 10, pp. 1734–43, 2012.

[153] X. Ding, Z. Peng, S.-C. S. Lin, M. Geri, S. Li, P. Li, Y. Chen, M. Dao, S. Suresh, and T. J. Huang, "Cell separation using tilted-angle standing surface acoustic waves," *Proceedings of the National Academy of Sciences*, vol. 111, no. 36, pp. 12992–12997, 2014.

[154] M. Bok, H. Y. Li, L. Y. Yeo, and J. R. Friend, "The dynamics of surface acoustic wave-driven scaffold cell seeding," *Biotechnology And Bioengineering*, vol. 103, no. 2, pp. 387–401, 2009.

[155] X. Ding, P. Li, S.-C. S. Lin, Z. S. Stratton, N. Nama, F. Guo, D. Slotcavage, X. Mao, J. Shi, F. Costanzo, *et al.*, "Surface acoustic wave microfluidics," *Lab on a Chip*, vol. 13, no. 18, pp. 3626–3649, 2013.

[156] X. Ding, J. Shi, S.-C. S. Lin, S. Yazdi, B. Kiraly, and T. J. Huang, "Tunable patterning of microparticles and cells using standing surface acoustic waves," *Lab on a Chip*, vol. 12, no. 14, pp. 2491–2497, 2012.

[157] J. Shi, D. Ahmed, X. Mao, S.-C. S. Lin, A. Lawit, and T. J. Huang, "Acoustic tweezers: patterning cells and microparticles using standing surface acoustic waves (ssaw)," *Lab on a Chip*, vol. 9, no. 20, p. 2890, 2009.

[158] P. Glynne-Jones, R. J. Boltryk, and M. Hill, "Acoustofluidics 9: Modelling and applications of planar resonant devices for acoustic particle manipulation," *Lab on a Chip*, vol. 12, no. 8, pp. 1417–1426, 2012.

[159] A. Lenshof, C. Magnusson, and T. Laurell, "Acoustofluidics 8: applications of acoustophoresis in continuous flow microsystems," *Lab on a Chip*, vol. 12, no. 7, pp. 1210–23, 2012.

[160] O. Manneberg, B. Vanherberghen, B. Önfelt, and M. Wiklund, "Flow-free transport of cells in microchannels by frequency-modulated ultrasound," *Lab on a Chip*, vol. 9, no. 6, pp. 833–837, 2009.

[161] C. R. P. Courtney, C.-K. Ong, B. W. Drinkwater, P. D. Wilcox, C. Demore, S. Cochran, P. Glynne-Jones, and M. Hill, "Manipulation of microparticles using phase-controllable ultrasonic standing waves," *Journal of the Acoustical Society of America*, vol. 128, no. 4, p. 5, 2010.

[162] F. Gesellchen, A. Bernassau, T. Déjardin, D. Cumming, and M. O. Riehle, "Cell patterning with a heptagon acoustic tweezer–application in neurite guidance," *Lab on a Chip*, vol. 14, no. 13, pp. 2266–2275, 2014.

[163] P. Glynne-Jones, C. E. Demore, C. Ye, Y. Qiu, S. Cochran, and M. Hill, "Array-controlled ultrasonic manipulation of particles in planar acoustic resonator," *Ultrasonics, Ferroelectrics and Frequency Control, IEEE Transactions on*, vol. 59, no. 6, pp. 1258–1266, 2012.

[164] R. Zmijan, U. S. Jonnalagadda, D. Carugo, Y. Kochi, E. Lemm, G. Packham, M. Hill, and P. Glynne-Jones, "High throughput imaging cytometer with acoustic focussing," *RSC Advances*, vol. 5, no. 101, pp. 83206–83216, 2015.

[165] T. M. Llewellyn-Jones, B. W. Drinkwater, and R. S. Trask, "3-D printed composites with ultrasonically arranged complex microstructure," in *SPIE Smart Structures and Materials+ Nondestructive Evaluation and Health Monitoring*, pp. 97970A–97970A, International Society for Optics and Photonics, 2016.

[166] G. Sitters, D. Kamsma, G. Thalhammer, M. Ritsch-Marte, E. J. Peterman, and G. J. Wuite, "Acoustic force spectroscopy," *Nature methods*, vol. 12, no. 1, pp. 47–50, 2015.

[167] L. Y. Yeo and J. R. Friend, "Surface acoustic wave microfluidics," *Annual Review of Fluid Mechanics*, vol. 46, pp. 379–406, 2014.

[168] M. Gedge and M. Hill, "Acoustofluidics 17: Theory and applications of surface acoustic wave devices for particle manipulation," *Lab on a Chip*, vol. 12, no. 17, pp. 2998–3007, 2012.

[169] F. Guo, P. Li, J. B. French, Z. Mao, H. Zhao, S. Li, N. Nama, J. R. Fick, S. J. Benkovic, and T. J. Huang, "Controlling cell–cell interactions using surface acoustic waves," *Proceedings of the National Academy of Sciences*, vol. 112, no. 1, pp. 43–48, 2015.

[170] Y. Chen, S. Li, Y. Gu, P. Li, X. Ding, L. Wang, J. P. McCoy, S. J. Levine, and T. J. Huang, "Continuous enrichment of low-abundance cell samples using standing surface acoustic waves (ssaw)," *Lab on a Chip*, vol. 14, no. 5, pp. 924–930, 2014.

[171] D. Ahmed, A. Ozcelik, N. Bojanala, N. Nama, A. Upadhyay, Y. Chen, W. Hanna-Rose, and T. J. Huang, "Rotational manipulation of single cells and organisms using acoustic waves," *Nature communications*, vol. 7, 2016.

[172] R. Elbez, B. H. McNaughton, L. Patel, K. J. Pienta, and R. Kopelman, "Nanoparticle induced cell magneto-rotation: monitoring morphology, stress and drug sensitivity of a suspended single cancer cell," *PLOS ONE*, vol. 6, no. 12, p. e28475, 2011.

[173] J. Friend and L. Yeo, "Microscale acoustofluidics: Microfluidics driven via acoustics and ultrasonics," *Reviews of Modern Physics*, vol. 83, pp. 647–704, June 2011.

[174] Y. Qiu, H. Wang, C. E. Demore, D. A. Hughes, P. Glynne-Jones, S. Gebhardt, A. Bolhovitins, R. Poltarjonoks, K. Weijer, A. Schönecker, *et al.*, "Acoustic devices for particle and cell manipulation and sensing," *Sensors*, vol. 14, no. 8, pp. 14806–14838, 2014.

[175] M. Evander and J. Nilsson, "Acoustofluidics 20: applications in acoustic trapping," *Lab on a Chip*, vol. 12, no. 22, pp. 4667–4676, 2012.

[176] D. N. Ankrett, D. Carugo, J. Lei, P. Glynne-Jones, P. A. Townsend, X. Zhang, and M. Hill, "The effect of ultrasound-related stimuli on cell viability in microfluidic channels," *J Nanobiotechnology*, vol. 11, p. 20, 2013.

[177] R. M. Johann, "Cell trapping in microfluidic chips," *Analytical and Bioanalytical Chemistry*, vol. 385, no. 3, pp. 408–12, 2006.

[178] K. Halvorsen and W. P. Wong, "Massively parallel single-molecule manipulation using centrifugal force," *Biophysical journal*, vol. 98, no. 11, pp. L53–L55, 2010.

[179] D. Bazou, E. J. Blain, and W. T. Coakley, "Ncam and psa-ncam dependent membrane spreading and f-actin reorganization in suspended adhering neural cells," *Molecular Membrane Biology*, vol. 25, no. 2, pp. 102–14, 2008.

[180] D. Bazou, G. A. Foster, J. R. Ralphs, and W. T. Coakley, "Molecular adhesion development in a neural cell monolayer forming in an ultrasound trap," *Molecular Membrane Biology*, vol. 22, no. 3, pp. 229–40, 2005.

[181] T. W. Frisk, M. A. Khorshidi, K. Guldevall, B. Vanherberghen, and B. Önfelt, "A silicon-glass microwell platform for high-resolution imaging and high-content screening with single cell resolution," *Biomedical microdevices*, vol. 13, no. 4, pp. 683–693, 2011.

[182] A. E. Christakou, M. Ohlin, B. Vanherberghen, M. A. Khorshidi, N. Kadri, T. Frisk, M. Wiklund, and B. Önfelt, "Live cell imaging in a micro-array of acoustic traps facilitates quantification of natural killer cell heterogeneity," *Integrative Biology*, vol. 5, no. 4, pp. 712–719, 2013.

[183] A. E. Christakou, M. Ohlin, B. Önfelt, and M. Wiklund, "Ultrasonic three-dimensional on-chip cell culture for dynamic studies of tumor immune surveillance by natural killer cells," *Lab on a Chip*, vol. 15, no. 15, pp. 3222–3231, 2015.

[184] D. Bazou, G. P. Dowthwaite, I. M. Khan, C. W. Archer, J. R. Ralphs, and W. T. Coakley, "Gap junctional intercellular communication and cytoskeletal organization in chondrocytes in suspension in an ultrasound trap," *Molecular Membrane Biology*, vol. 23, no. 2, pp. 195–205, 2006.

[185] M. Antfolk, C. Antfolk, H. Lilja, T. Laurell, and P. Augustsson, "A single inlet two-stage acoustophoresis chip enabling tumor cell enrichment from white blood cells," *Lab on a chip*, vol. 15, no. 9, pp. 2102–2109, 2015.

[186] M. Antfolk, C. Magnusson, P. Augustsson, H. Lilja, and T. Laurell, "Acoustofluidic, label-free separation and simultaneous concentration of rare tumor cells from white blood cells," *Analytical chemistry*, vol. 87, no. 18, pp. 9322–9328, 2015.

[187] P. Augustsson, J. T. Karlsen, H.-W. Su, H. Bruus, and J. Voldman, "Iso-acoustic focusing of cells for size-insensitive acousto-mechanical phenotyping," *Nature communications*, vol. 7, 2016.

[188] J. T. Karlsen, P. Augustsson, and H. Bruus, "Acoustic force density acting on inhomogeneous fluids in acoustic fields," *Physical Review Letters*, vol. 117, p. 114504, Sept. 2016.

[189] A. Garbin, I. Leibacher, P. Hahn, H. Le Ferrand, A. Studart, and J. Dual, "Acoustophoresis of disk-shaped microparticles: A numerical and experimental study of acoustic radiation forces and torques," *The Journal of the Acoustical Society of America*, vol. 138, no. 5, pp. 2759–2769, 2015.

[190] P. Hahn, I. Leibacher, T. Baasch, and J. Dual, "Numerical simulation of acoustofluidic manipulation by radiation forces and acoustic streaming for complex particles," *Lab on a Chip*, vol. 15, no. 22, pp. 4302–4313, 2015.

[191] E. S. Comeau, D. C. Hocking, and D. Dalecki, "Ultrasound patterning technologies for studying vascular morphogenesis in 3D," *J Cell Sci*, vol. 130, no. 1, pp. 232–242, 2017.

[192] L. Kock, C. C. van Donkelaar, and K. Ito, "Tissue engineering of functional articular cartilage: the current status," *Cell and Tissue Research*, vol. 347, no. 3, pp. 613–27, 2012.

[193] C. Chung and J. A. Burdick, "Engineering cartilage tissue," *Advanced Drug Delivery Reviews*, vol. 60, no. 2, pp. 243–62, 2008.

[194] R. S. Tare, J. C. Babister, J. Kanczler, and R. O. Oreffo, "Skeletal stem cells: phenotype, biology and environmental niches informing tissue regeneration," *Molecular and Cellular Endocrinology*, vol. 288, no. 1-2, pp. 11–21, 2008.

[195] A. Cheng, T. E. Hardingham, and S. J. Kimber, "Generating cartilage repair from pluripotent stem cells," *Tissue Engineering Part B*, 2013.

[196] A. Inui, T. Iwakura, and A. H. Reddi, "Human stem cells and articular cartilage regeneration," *Cells*, vol. 1, no. 4, pp. 994–1009, 2012.

[197] B. Johnstone, M. Alini, M. Cucchiarini, G. R. Dodge, D. Eglin, F. Guilak, H. Madry, A. Mata, R. L. Mauck, C. E. Semino, and M. J. Stoddart, "Tissue engineering for articular cartilage repair–the state of the art," *European Cells and Materials*, vol. 25, pp. 248–67, 2013.

[198] J. M. Jukes, C. A. van Blitterswijk, and J. de Boer, "Skeletal tissue engineering using embryonic stem cells," *Journal of tissue engineering and regenerative medicine*, vol. 4, no. 3, pp. 165–180, 2010.

[199] M. Tang, W. Chen, J. Liu, M. D. Weir, L. Cheng, and H. H. Xu, "Human induced pluripotent stem cell-derived mesenchymal stem cell seeding on calcium phosphate scaffold for bone regeneration," *Tissue Engineering Part A*, vol. 20, no. 7-8, pp. 1295–1305, 2014.

[200] J. Kramer, C. Hegert, K. Guan, A. M. Wobus, P. K. Muller, and J. Rohwedel, "Embryonic stem cell-derived chondrogenic differentiation in vitro: activation by bmp-2 and bmp-4," *Mechanisms of Development*, vol. 92, no. 2, pp. 193–205, 2000.

[201] K. Umeda, J. Zhao, P. Simmons, E. Stanley, A. Elefanty, and N. Nakayama, "Human chondrogenic paraxial mesoderm, directed specification and prospective isolation from pluripotent stem cells," *Scientific Reports*, vol. 2, p. 455, 2012.

[202] G. E. Salazar-Noratto, F. P. Barry, and R. E. Guldberg, "Application of biomaterials to in vitro pluripotent stem cell disease modeling of the skeletal system," *Journal of Materials Chemistry B*, vol. 4, no. 20, pp. 3482–3489, 2016.

[203] R. S. Tare, J. Kanczler, A. Aarvold, A. M. Jones, D. G. Dunlop, and R. O. Oreffo, "Skeletal stem cells and bone regeneration: translational strategies from bench to clinic," *Proceedings of the Institution of Mechanical Engineers, Part H*, vol. 224, no. 12, pp. 1455–70, 2010.

[204] R. S. Tare, D. Howard, J. C. Pound, H. I. Roach, and R. O. Oreffo, "Tissue engineering strategies for cartilage generation–micromass and three dimensional

cultures using human chondrocytes and a continuous cell line," *Biochemical and Biophysical Research Communications*, vol. 333, no. 2, pp. 609–21, 2005.

[205] P. Bianco and P. G. Robey, *Skeletal Stem Cells*, vol. 2, book section 39, pp. 415–424. New York: Academic Press, 2004.

[206] A. J. Friedenstein, R. K. Chailakhjan, and K. S. Lalykina, "The development of fibroblast colonies in monolayer cultures of guinea-pig bone marrow and spleen cells," *Cell and Tissue Kinetics*, vol. 3, no. 4, pp. 393–403, 1970.

[207] J. I. Dawson, J. Kanczler, R. Tare, M. Kassem, and R. O. Oreffo, "Concise review: bridging the gap: bone regeneration using skeletal stem cell-based strategies - where are we now?," *Stem Cells*, vol. 32, no. 1, pp. 35–44, 2014.

[208] A. Muraglia, R. Cancedda, and R. Quarto, "Clonal mesenchymal progenitors from human bone marrow differentiate in vitro according to a hierarchical model," *Journal of cell science*, vol. 113, no. 7, pp. 1161–1166, 2000.

[209] F.-J. Lv, R. S. Tuan, K. Cheung, and V. Y. Leung, "Concise review: the surface markers and identity of human mesenchymal stem cells," *Stem Cells*, vol. 32, no. 6, pp. 1408–1419, 2014.

[210] D. Gothard, K. Cheung, J. M. Kanczler, D. I. Wilson, and R. O. Oreffo, "Regionally-derived cell populations and skeletal stem cells from human foetal femora exhibit specific osteochondral and multi-lineage differentiation capacity in vitro and ex vivo," *Stem Cell Research & Therapy*, vol. 6, pp. 1–17, Dec. 2015.

[211] S. Gronthos, A. C. Zannettino, S. J. Hay, S. Shi, S. E. Graves, A. Kortesidis, and P. J. Simmons, "Molecular and cellular characterisation of highly purified stromal stem cells derived from human bone marrow," *Journal of Cell Science*, vol. 116, no. Pt 9, pp. 1827–35, 2003.

[212] P. Bianco, X. Cao, P. S. Frenette, J. J. Mao, P. G. Robey, P. J. Simmons, and C. Y. Wang, "The meaning, the sense and the significance: translating the science of mesenchymal stem cells into medicine," *Nature Medicine*, vol. 19, no. 1, pp. 35–42, 2013.

[213] J. C. Pound, D. W. Green, J. B. Chaudhuri, S. Mann, H. I. Roach, and R. O. Oreffo, "Strategies to promote chondrogenesis and osteogenesis from human bone

marrow cells and articular chondrocytes encapsulated in polysaccharide templates," *Tissue Engineering*, vol. 12, no. 10, pp. 2789–99, 2006.

[214] S. Wakitani, T. Mitsuoka, N. Nakamura, Y. Toritsuka, Y. Nakamura, and S. Horibe, "Autologous bone marrow stromal cell transplantation for repair of full-thickness articular cartilage defects in human patellae: two case reports," *Cell Transplantation*, vol. 13, no. 5, pp. 595–600, 2004.

[215] X. Houard, M. B. Goldring, and F. Berenbaum, "Homeostatic mechanisms in articular cartilage and role of inflammation in osteoarthritis," *Current Rheumatology Reports*, vol. 15, no. 11, p. 375, 2013.

[216] L. Danisovic, I. Varga, R. Zamborsky, and D. Bohmer, "The tissue engineering of articular cartilage: cells, scaffolds and stimulating factors," *Exp Biol Med (Maywood)*, vol. 237, no. 1, pp. 10–7, 2012.

[217] E. B. Hunziker, "Articular cartilage repair: basic science and clinical progress. a review of the current status and prospects," *Osteoarthritis and Cartilage*, vol. 10, no. 6, pp. 432–63, 2002.

[218] E. J. Levorson, M. Santoro, F. K. Kasper, and A. G. Mikos, "Direct and indirect co-culture of chondrocytes and mesenchymal stem cells for the generation of polymer/extracellular matrix hybrid constructs," *Acta biomaterialia*, vol. 10, no. 5, pp. 1824–1835, 2014.

[219] R. L. Dahlin, M. Ni, V. V. Meretoja, F. K. Kasper, and A. G. Mikos, "Tgf-β3-induced chondrogenesis in co-cultures of chondrocytes and mesenchymal stem cells on biodegradable scaffolds," *Biomaterials*, vol. 35, no. 1, pp. 123–132, 2014.

[220] L. Bian, D. Y. Zhai, R. L. Mauck, and J. A. Burdick, "Coculture of human mesenchymal stem cells and articular chondrocytes reduces hypertrophy and enhances functional properties of engineered cartilage," *Tissue Engineering Part A*, vol. 17, no. 7-8, pp. 1137–45, 2011.

[221] K. Tsuchiya, G. Chen, T. Ushida, T. Matsuno, and T. Tateishi, "The effect of coculture of chondrocytes with mesenchymal stem cells on their cartilaginous phenotype in vitro," *Materials Science and Engineering: C*, vol. 24, no. 3, pp. 391–396, 2004.

[222] J. C. Robins, N. Akeno, A. Mukherjee, R. R. Dalal, B. J. Aronow, P. Koopman, and T. L. Clemens, "Hypoxia induces chondrocyte-specific gene expression in mesenchymal cells in association with transcriptional activation of sox9," *Bone*, vol. 37, no. 3, pp. 313–322, 2005.

[223] K. Arvidson, B. Abdallah, L. Applegate, N. Baldini, E. Cenni, E. Gomez-Barrena, D. Granchi, M. Kassem, Y. Konttinen, K. Mustafa, *et al.*, "Bone regeneration and stem cells," *Journal of cellular and molecular medicine*, vol. 15, no. 4, pp. 718–746, 2011.

[224] D. Gothard, J. Greenhough, E. Ralph, and R. O. Oreffo, "Prospective isolation of human bone marrow stromal cell subsets: A comparative study between stro-1-, CD146-and CD105-enriched populations," *Journal of tissue engineering*, vol. 5, p. 2041731414551763, 2014.

[225] S. Li, B. G. Sengers, R. O. Oreffo, and R. S. Tare, "Chondrogenic potential of human articular chondrocytes and skeletal stem cells: a comparative study," *Journal of Biomaterials Applications*, vol. 29, no. 6, pp. 824–36, 2015.

[226] J. Hendriks, J. Riesle, and C. A. van Blitterswijk, "Co-culture in cartilage tissue engineering," *Journal of tissue engineering and regenerative medicine*, vol. 1, no. 3, pp. 170–178, 2007.

[227] T. S. de Windt, J. A. Hendriks, X. Zhao, L. A. Vonk, L. B. Creemers, W. J. Dhert, M. A. Randolph, and D. B. Saris, "Concise review: unraveling stem cell cocultures in regenerative medicine: which cell interactions steer cartilage regeneration and how?," *Stem cells translational medicine*, vol. 3, no. 6, pp. 723–733, 2014.

[228] J. Fischer, A. Dickhut, M. Rickert, and W. Richter, "Human articular chondrocytes secrete parathyroid hormone-related protein and inhibit hypertrophy of mesenchymal stem cells in coculture during chondrogenesis," *Arthritis and Rheumatism*, vol. 62, no. 9, pp. 2696–706, 2010.

[229] R. S. Tare, P. D. Mitchell, J. Kanczler, and R. O. Oreffo, "Isolation, differentiation, and characterisation of skeletal stem cells from human bone marrow in vitro and in vivo," *Methods in Molecular Biology*, vol. 816, pp. 83–99, 2012.

[230] M. C. de Andres, K. Imagawa, K. Hashimoto, A. Gonzalez, M. B. Goldring, H. I. Roach, and R. O. Oreffo, "Suppressors of cytokine signalling (socs) are reduced in

osteoarthritis," *Biochemical and Biophysical Research Communications*, vol. 407, no. 1, pp. 54–9, 2011.

[231] L. Lison, "Alcian blue 8 g with chlorantine fast red 5 B. a technic for selective staining of mucopolysaccharides," *Biotechnic & Histochemistry*, vol. 29, no. 3, pp. 131–138, 1954.

[232] S. Giovannini, J. Diaz-Romero, T. Aigner, P. Heini, P. Mainil-Varlet, and D. Nesic, "Micromass co-culture of human articular chondrocytes and human bone marrow mesenchymal stem cells to investigate stable neocartilage tissue formation in vitro," *European Cells and Materials*, vol. 20, pp. 245–59, 2010.

[233] W. H. Chen, M. T. Lai, A. T. Wu, C. C. Wu, J. G. Gelovani, C. T. Lin, S. C. Hung, W. T. Chiu, and W. P. Deng, "In vitro stage-specific chondrogenesis of mesenchymal stem cells committed to chondrocytes," *Arthritis and Rheumatism*, vol. 60, no. 2, pp. 450–9, 2009.

[234] Y. J. Kim, H. J. Kim, and G. I. Im, "Pthrp promotes chondrogenesis and suppresses hypertrophy from both bone marrow-derived and adipose tissue-derived mscs," *Biochemical and Biophysical Research Communications*, vol. 373, no. 1, pp. 104–8, 2008.

[235] T. Xu, K. Yang, H. You, A. Chen, J. Wang, K. Xu, C. Gong, J. Shao, Z. Ma, F. Guo, and J. Qi, "Regulation of pthrp expression by cyclic mechanical strain in postnatal growth plate chondrocytes," *Bone*, vol. 56, no. 2, pp. 304–11, 2013.

[236] J. Fischer, M. Ortel, S. Hagmann, A. Hoeflich, and W. Richter, "Role of pthrp (1-34) pulse frequency versus pulse duration to enhance mesenchymal stromal cell chondrogenesis," *Journal of Cellular Physiology*, 2016.

[237] D. Tang, R. S. Tare, L. Y. Yang, D. F. Williams, K. L. Ou, and R. O. Oreffo, "Biofabrication of bone tissue: approaches, challenges and translation for bone regeneration," *Biomaterials*, vol. 83, pp. 363–82, 2016.

[238] I. Moreno-Jimenez, G. Hulsart-Billstrom, S. A. Lanham, A. A. Janeczek, N. Kontouli, J. M. Kanczler, N. D. Evans, and R. O. Oreffo, "The chorioallantoic membrane (cam) assay for the study of human bone regeneration: a refinement animal model for tissue engineering," *Scientific Reports*, vol. 6, p. 32168, 2016.

[239] K. E. Sisti, M. C. de Andres, D. Johnston, E. Almeida-Filho, A. C. Guastaldi, and R. O. Oreffo, "Skeletal stem cell and bone implant interactions are enhanced by laser titanium modification," *Biochemical and Biophysical Research Communications*, vol. 473, no. 3, pp. 719–25, 2016.

[240] D. M. Gibbs, C. R. Black, J. I. Dawson, and R. O. Oreffo, "A review of hydrogel use in fracture healing and bone regeneration," *Journal of Tissue Engineering and Regenerative Medicine*, vol. 10, no. 3, pp. 187–98, 2016.

[241] C. R. Black, V. Goriainov, D. Gibbs, J. Kanczler, R. S. Tare, and R. O. Oreffo, "Bone tissue engineering," *Current Molecular Biology Reports*, vol. 1, no. 3, pp. 132–140, 2015.

[242] K. Y. Ching, O. G. Andriotis, S. Li, P. Basnett, B. Su, I. Roy, R. S. Tare, B. G. Sengers, and M. Stolz, "Nanofibrous poly (3-hydroxybutyrate)/poly (3-hydroxyoctanoate) scaffolds provide a functional microenvironment for cartilage repair," *Journal of biomaterials applications*, p. 0885328216639749, 2016.

[243] M. Vaezi and S. Yang, "A novel bioactive peek/ha composite with controlled 3D interconnected ha network," *2015*, vol. 1, no. 1, 2015.

[244] H. W. Kang, S. J. Lee, I. K. Ko, C. Kengla, J. J. Yoo, and A. Atala, "A 3D bioprinting system to produce human-scale tissue constructs with structural integrity," *Nature Biotechnology*, vol. 34, no. 3, pp. 312–9, 2016.

[245] M. Hill, Y. Shen, and J. J. Hawkes, "Modelling of layered resonators for ultrasonic separation," *Ultrasonics*, vol. 40, no. 1-8, pp. 385–92, 2002.

[246] L. Gor'kov, "On the forces acting on a small particle in an acoustical field in an ideal fluid," *Soviet Physics Doklady*, vol. 6, no. 9, pp. 773–5, 1962.

[247] A. Lamprecht, S. Lakamper, I. A. Schaap, and J. Dual, "Measurement of 3D-forces on a micro particle in acoustofluidic devices using an optical trap," *Physics Procedia*, vol. 70, pp. 89–93, 2015.

[248] G. K. Batchelor, "Flow of a uniform incompressible viscous fluid," in *An Introduction to Fluid Dynamics:*, pp. 174–263, Cambridge: Cambridge University Press, Feb. 2000.

[249] C. Gamonpilas and E. P. Busso, "On the effect of substrate properties on the indentation behaviour of coated systems," *Materials Science and Engineering*, vol. 380, no. 12, pp. 52–61, 2004.

[250] S. Tomkoria, R. V. Patel, Mao, and J. J, "Heterogeneous nanomechanical properties of superficial and zonal regions of articular cartilage of the rabbit proximal radius condyle by atomic force microscopy," *Medical Engineering & Physics*, vol. 26, no. 10, pp. 815–822, 2004.

[251] V. C. Mow and R. Huiskes, *Basic orthopaedic biomechanics & mechano-biology*. Lippincott Williams & Wilkins, 2005.

[252] K. Hu, P. Radhakrishnan, R. V. Patel, and J. J. Mao, "Regional structural and viscoelastic properties of fibrocartilage upon dynamic nanoindentation of the articular condyle," *Journal of Structural Biology*, vol. 136, no. 1, pp. 46–52, 2001.

[253] W. C. Oliver and G. M. Pharr, "Measurement of hardness and elastic modulus by instrumented indentation: Advances in understanding and refinements to methodology," *Journal of materials research*, vol. 19, no. 01, pp. 3–20, 2004.

[254] S. Sadhal, "Acoustofluidics 13: Analysis of acoustic streaming by perturbation methods," *Lab on a Chip*, vol. 12, no. 13, pp. 2292–2300, 2012.

[255] J. Lei, P. Glynne-Jones, and M. Hill, "Modal Rayleigh-like streaming in layered acoustofluidic devices," *Physics of Fluids (1994-present)*, vol. 28, no. 1, p. 012004, 2016.

[256] P. B. Muller, R. Barnkob, M. J. Jensen, and H. Bruus, "A numerical study of microparticle acoustophoresis driven by acoustic radiation forces and streaming-induced drag forces," *Lab on a Chip*, vol. 12, no. 22, pp. 4617–27, 2012.

[257] P. B. Muller and H. Bruus, "Theoretical study of time-dependent, ultrasound-induced acoustic streaming in microchannels," *Physical Review E*, vol. 92, no. 6, p. 063018, 2015.

[258] X. Chen, F. He, D.-Y. Zhong, and Z.-P. Luo, "Acoustic-frequency vibratory stimulation regulates the balance between osteogenesis and adipogenesis of human bone marrow-derived mesenchymal stem cells," *BioMed research international*, vol. 2015, 2015.

[259] O. R. Schatti, L. M. Gallo, and P. A. Torzilli, "A model to study articular cartilage mechanical and biological responses to sliding loads," *Annals of Biomedical Engineering*, 2015.

[260] V. Aubert, R. Wunenburger, T. Valier-Brasier, D. Rabaud, J.-P. Kleman, and C. Poulain, "A simple acoustofluidic chip for microscale manipulation using evanescent scholte waves," *Lab on a Chip*, vol. 16, no. 13, pp. 2532–2539, 2016.

[261] T. Yamashita, K.-y. Hashimoto, and M. Yamaguchi, "Highly piezoelectric shear-horizontal-type boundary waves," *Japanese journal of applied physics*, vol. 36, no. 5S, p. 3057, 1997.

[262] Y.-C. Kuo, T.-H. Chang, W.-T. Hsu, J. Zhou, H.-H. Lee, J. Hui-Chun Ho, S. Chien, and O. Kuang-Sheng, "Oscillatory shear stress mediates directional reorganization of actin cytoskeleton and alters differentiation propensity of mesenchymal stem cells," *Stem Cells*, vol. 33, no. 2, pp. 429–442, 2015.

[263] M. Chachisvilis, Y.-L. Zhang, and J. A. Frangos, "G protein-coupled receptors sense fluid shear stress in endothelial cells," *Proceedings of the National Academy of Sciences*, vol. 103, no. 42, pp. 15463–15468, 2006.

[264] L. Liu, W. Yuan, and J. Wang, "Mechanisms for osteogenic differentiation of human mesenchymal stem cells induced by fluid shear stress," *Biomechanics and modeling in mechanobiology*, vol. 9, no. 6, pp. 659–670, 2010.

[265] K. M. Kim, Y. J. Choi, J.-H. Hwang, A. R. Kim, H. J. Cho, E. S. Hwang, J. Y. Park, S.-H. Lee, and J.-H. Hong, "Shear stress induced by an interstitial level of slow flow increases the osteogenic differentiation of mesenchymal stem cells through taz activation," *PloS one*, vol. 9, no. 3, p. e92427, 2014.

[266] L. Wang, J.-Y. Luo, B. Li, X. Y. Tian, L.-J. Chen, Y. Huang, J. Liu, D. Deng, C. W. Lau, S. Wan, *et al.*, "Integrin-yap/taz-jnk cascade mediates atheroprotective effect of unidirectional shear flow," *Nature*, 2016.

[267] S. Dupont, L. Morsut, M. Aragona, E. Enzo, S. Giulitti, M. Cordenonsi, F. Zanconato, J. Le Digabel, M. Forcato, S. Bicciato, *et al.*, "Role of yap/taz in mechanotransduction," *Nature*, vol. 474, no. 7350, pp. 179–183, 2011.

[268] X. Guo and B. Zhao, "Integration of mechanical and chemical signals by yap and taz transcription coactivators," *Cell & bioscience*, vol. 3, no. 1, p. 33, 2013.

[269] H. Y. Chun-do Oh, W. Zhao, S. P. Henry, Z. Zhang, M. Xue, B. De Crombrugghe, and D. Chen, "Sox9 directly regulates ctgf/ccn2 transcription in growth plate chondrocytes and in nucleus pulposus cells of intervertebral disc," *Scientific Reports*, vol. 6, 2016.

[270] B. Chaqour and M. Goppelt-Struebe, "Mechanical regulation of the cyr61/ccn1 and ctgf/ccn2 proteins," *FEBS Journal*, vol. 273, no. 16, pp. 3639–3649, 2006.

Appendix A

MATLAB Code

A.1 Image analysis script for quantifying the section staining and section total area for histochemical and immuno stains.

```
1  % close all
2 %Batch processing script to compute staining area and total area of
3 %section.
4 function [] = histochemAnalysis
5     close all
6     pathToDir = 'D:\test\gag test'; gagFlag = true;
7
8     if(isdir(pathToDir))
9         content = dir(pathToDir);
10        output = containers.Map;
11        for i = 4:length(content)
12            fileObj = content(i);
13            %Iterate through file list for images to process
14             if(fileObj.isdir == 0 && length(strfind(fileObj.name, '.txt'))
      == 0)
15                pathToFile = strcat(pathToDir, '/', fileObj.name)
16                stainType = fileObj.name(1:strfind(fileObj.name, '.')-1);
17                [stainArea, backgroundArea] = processImage(imread(
      pathToFile), gagFlag);
18                outputToAppend = [stainArea, backgroundArea, stainArea /
      backgroundArea];
```

```
19                  temp = containers.Map(stainType, outputToAppend);
20                  output = [output; temp];
21                  break;
22              end
23          end
24          %Save area information to file
25          writeToFile(output, pathToDir);
26      end
27  end
28
29  %method uses k-means clustering to identify and sort pixel colors into
30  %three sets. This method reliably has red pixels in one cluster and blue
31  %pixels in another, allowing simplier and more accurate segmentationa nd
32  %area calculate.
33  function [stainArea] = kMeansProcessing(img, gagFlag)
34      cform = makecform('srgb2lab');
35      labImg = applycform(img, cform);
36
37      ab = double(labImg(:,:,2:3));
38      nrows = size(ab,1);
39      ncols = size(ab,2);
40      ab = reshape(ab,nrows*ncols,2);
41
42      nColors = 3;
43
44      [cluster_idx, cluster_center] = kmeans(ab,nColors,'distance','
        sqEuclidean', 'Replicates',3);
45      pixel_labels = reshape(cluster_idx,nrows,ncols);
46  %     figure; imshow(pixel_labels,[]), title('image labeled by cluster
        index');
47
48      segmentedImg = cell(1,3);
49      overlayImg = repmat(pixel_labels,[1 1 3]);
50
51      for k = 1:3
52          colorImg = img;
53          colorImg(overlayImg ~= k) = 0;
54          segmentedImg{k} = colorImg;
55      end
56
57      meanClusterValue = mean(cluster_center,2);
```

```
58      %the sort more uniformally identifies which cluster as which to ease
59      %staining identification and calculations.
60      [tmp, idx] = sort(meanClusterValue);
61      figure;imshow(img), title('Source Image');
62      figure;imshow(segmentedImg{idx(1)}), title('objects in cluster 1');
63      figure;imshow(segmentedImg{idx(2)}), title('objects in cluster 2'); %
        high gag staining
64      figure;imshow(segmentedImg{idx(3)}), title('objects in cluster 3'); %
        high collagen staining
65
66      if gagFlag == true %target staining is Alcian Blue
67          finalImg = (segmentedImg{idx(1)}+segmentedImg{idx(2)});
68          finalImg = finalImg(:,:,3)-finalImg(:,:,1);
69  %         figure;imshow(finalImg), title('Isolation of Stained Area');
70          avgIntensity = mean(mean(finalImg))
71          binaryImg = im2bw(finalImg);
72      else %target staining is AEC (perioxide rxn with enzyme to turn target
        area red
73          finalImg = segmentedImg{idx(3)} + segmentedImg{idx(2)};
74  %         figure;imshow(finalImg), title('Isolation of Stained Area');
75          finalImg = finalImg(:,:,1) - finalImg(:,:,3);
76          binaryImg = finalImg;
77      end
78
79      figure;imshow(binaryImg), title('Isolation of Stained Area without
        Background');
80      stainArea = sum(sum(binaryImg > 0))
81  end
82
83  %method processes each image by creating a mask over the whole section to
84  %compute the whole section pixel area. A helper method computes the
85  %target staining pixel area in order to determine the percent staining
86  %coverage in the section.
87  function [stainArea, backgroundArea] = processImage(img, gagFlag)
88  %     figure;imshow(img)
89
90      backgroundChannel = rgb2gray(img); %convert whole image to grayscale
91      imgScaling = 0.8; %pxl / micron
92
93      maxPxlValue = max(backgroundChannel(:)); %typically cell or other stain
94      minPxlValue = min(backgroundChannel(:)); %background pixel value
```

```
95      %separate section from background/noise
96      maxPxlValue = maxPxlValue - (maxPxlValue * .1);
97      backgroundChannel(backgroundChannel > maxPxlValue) = minPxlValue;
98      backgroundChannel(backgroundChannel < minPxlValue) = 0;
99
100     %segment section using Otsu
101     [backgroundLevel, backgroundEffectiveness] = graythresh(
        backgroundChannel);
102     backgroundBinary = im2bw(backgroundChannel, backgroundLevel);
103     backgroundBinary = backgroundChannel > minPxlValue;
104     %try to fill up any holes in the section to get as close to a proper
105     %mask
106     se = strel('disk',3);
107     backgroundBinary = imdilate(backgroundBinary, se);
108     backgroundBinary = bwareaopen(backgroundBinary,100);
109
110 %     figure;imshow(backgroundBinary), title('Whole Section (Background)
        Binary');
111
112     backgroundArea = sum(sum(backgroundBinary > 0)) / imgScaling
113     %call helper method to segment staining area in section
114     stainArea = kMeansProcessing(img, gagFlag) / imgScaling
115
116 end
117
118 %method to save area outputs
119 function writeToFile(output, outputFileDir)
120     outputFilePath = strcat(outputFileDir, '/', 'stainingResults.txt');
121     keySet = keys(output);
122     outputArray = {};
123
124     for i = keySet
125         key = char(i);
126         valueSet = output(key);
127         outputCell = {key, valueSet};
128         outputArray = [outputArray; outputCell];
129     end
130
131
132     fileID = fopen(outputFilePath,'w');
133     formatSpec = '%s, %d, %d, %f\n';
```

```
134
135     [nrows,ncols] = size(outputArray);
136     for row = 1:nrows
137         fprintf(fileID,formatSpec,outputArray{row,:});
138     end
139
140     fclose(fileID);
141 end
```

A.2 Script to parse image cross correlation information to determine displacement over time, curve fit and shear stress.

```
1  close all
2  clear all
3  %load mean displacement data calculated from toolbox described in Zmijan et
4  %al
5  pathname = 'G:\Inverted Transducer Design Data\Timelapse\multiTransducer
       Shear\Plate 7 March 16 2016\200 kHz\Transducer 4\10 Hz 160 fps\2\';
6  load(strcat(pathname, 'crossCorr.mat'))
7  frameRate = 160; %frame rate dependent on parameter set to analyze
8  meanXData = xDisp';
9  meanYData = yDisp';
10
11 scale = 2.5; %pixels/micron
12
13 %convert displacement data from pixels to microns
14 meanXData = meanXData / scale;
15 meanYData = meanYData / scale;
16
17 hrCount = 0;
18 period = 1 / (frameRate/16);
19 timeInterval = 1/frameRate;
20 timeMax = length(meanXData) * timeInterval
21 time = [0:timeInterval:timeMax - timeInterval]';
22 time = time + (hrCount * 3600);
23 periodIdx = find(mod(time, period) == 0); %save index to observe 1
       displacement cycle
```

```
24
25 %loess curve smoothing method to provide gentle anti-aliasing
26 meanXData = smooth(time,meanXData,0.05,'loess');
27 meanYData = smooth(time,meanYData,0.05,'loess');
28
29 %record median X/Y displacement values to focus later plots around the
30 %origin
31 [leftMostValue] = median(meanXData);
32 [bottomMostValue] = median(meanYData);
33
34 meanDisplacementX = (meanXData(2:end) - meanXData(1:end-1));
35 meanDisplacementX = [0; meanDisplacementX];
36 meanVelocityX = (meanDisplacementX .* 10^-6) ./ timeInterval;
37 meanDisplacementY = (meanYData(2:end) - meanYData(1:end-1));
38 meanDisplacementY = [0; meanDisplacementY];
39 meanVelocityY = (meanDisplacementY .* 10^-6) ./ timeInterval;
40
41 %FFT fit for displacement curve to more easily get the angular freq.
42 %coefficient
43 fitType = 'fourier2';
44 fitOptions = fitoptions(fitType);
45
46 kinematicVisc =  6.959*10^-7;
47 dynamicVisc = .78*10^-3;
48
49 velocityAmplitudeX = abs(max(meanVelocityX)) + abs(min(meanVelocityX))
50 velocityAmplitudeY = abs(max(meanVelocityY)) + abs(min(meanVelocityY))
51
52 [fitVelocity, goYFit] = fit(time, xFitVelocity, fitType, fitOptions);
53 coeff = coeffvalues(fitVelocity);
54 angularFreqX = 2 * coeff(end);
55
56 [fitVelocity, goYFit] = fit(time, yFitVelocity, fitType, fitOptions);
57 coeff = coeffvalues(fitVelocity);
58 angularFreqY = 2 * coeff(end);
59
60 shearStressX = -dynamicVisc * sqrt(angularFreqX/(kinematicVisc)) *
       velocityAmplitudeX * (sin((pi/4) - angularFreqX.* time));
61 shearStressY = -dynamicVisc * sqrt(angularFreqY/(kinematicVisc)) *
       velocityAmplitudeY * (sin((pi/4) - angularFreqY.* time));
62 %convert shear stress to mPa
```

```
63  shearStressX = shearStressX * 10^3;
64  shearStressY = shearStressY * 10^3;
65
66  %various plots for debugging and checking displacement/velocity/stress
67  %curves
68  figure
69  plot(fitForXCurve, time, meanXData, 'b -')
70  xlabel('Time (sec)')
71  ylabel('Average Displacement (micron)')
72  title('Displacement Along X')
73  legend('meanDisplacement', 'curveFit')
74
75  figure
76  plot(fitForYCurve, time, meanYData, 'b -')
77  xlabel('Time (sec)')
78  ylabel('Average Displacement (micron)')
79  title('Displacement Along Y')
80  legend('meanDisplacement', 'curveFit')
81  %
82  figure
83  plot(time, meanVelocityX / 10^-6)
84  xlabel('Time (sec)')
85  ylabel('Average Velocity (micron/sec)')
86  title('Average Velocity Along X')
87
88  figure
89  plot(time, meanVelocityY / 10^-6)
90  xlabel('Time (sec)')
91  ylabel('Average Velocity (micron/sec)')
92  title('Average Velocity Along Y')
93
94  figure
95  plot(meanXData - leftMostValue, meanYData - bottomMostValue)
96  xlabel('Displacement along X (micron)')
97  ylabel('Displacement along Y (micron)')
98  title('Average movement relative to time')
99
100 initIdx = periodIdx(1);
101 finalIdx = periodIdx(2) + 1;
102
103 figure
```

```
104 plot(meanXData(initIdx:finalIdx)- leftMostValue, meanYData(initIdx:finalIdx
        )- bottomMostValue)
105 xlabel('Displacement along X (micron)')
106 ylabel('Displacement along Y (micron)')
107 title('Average movement relative to time')
108
109 % figure
110 % plot3(f_x, f_y, time)
111 % plot(f_x, f_y)
112 % xlabel('Displacement along X (micron)')
113 % ylabel('Displacement along Y (micron)')
114 % zlabel('Time')
115 % title('Average movement relative to time (from curve fit)')
116 %
117 figure
118 plot(time, shearStressX)
119 xlabel('Time (sec)')
120 ylabel('Shear Stress (mPa)')
121 title('Shear Stress Along X')
122 %
123 figure
124 plot(time, shearStressY)
125 xlabel('Time (sec)')
126 ylabel('Shear Stress (mPa)')
127 title('Shear Stress Along Y')
128
129 %shear magnitude along x, y, and xy
130 shearMagnitudeX = abs(max(shearStressX)) + abs(min(shearStressX));
131
132 shearMagnitudeY = abs(max(shearStressY)) + abs(min(shearStressY));
133
134 shearMagnitudeXY = sqrt(shearMagnitudeX^2 + shearMagnitudeY^2);
135
136 %XXX: TEST CODE
137 %FFT to of displacement data to determine correlation between sweep
138 %repetition rate and peak freqeuncy from curve
139 meanDisplacement = sqrt( (meanXData(1:end-1) - meanXData(2:end)).^2 + (
        meanYData(1:end-1) - meanYData(2:end)).^2 );
140
141 fftTest = fft(meanDisplacement);
142 P1 = abs( fftTest / (length(meanDisplacement)));
```

```
143 P2 = P1(1:(length(meanDisplacement)/2 + 1));
144 P2(2:end-1) = 2*P2(2:end-1);
145 fs = frameRate;
146 fftTest = fs * (0:(length(meanDisplacement)/2))/length(meanDisplacement);
147 figure;
148 plot(fftTest(2:end), P2(2:end))
149 title('FFT Spectrum')
150 [m, idx] = max(P2(2:end));
151 oscilatingFreq = fftTest(idx)
152
153 [shearMagnitudeX; shearMagnitudeY; shearMagnitudeXY; oscilatingFreq]'
154 %save data in matlab package for easy access and revisitation later
155 save(char(strcat(pathname,'crossCorr.mat')), 'shearMagnitudeX', '
    shearMagnitudeY', 'shearMagnitudeXY', 'oscilatingFreq', 'meanXData', '
    meanYData', '-append');
```

Appendix B

Supplementary Figures - Biorector Culture

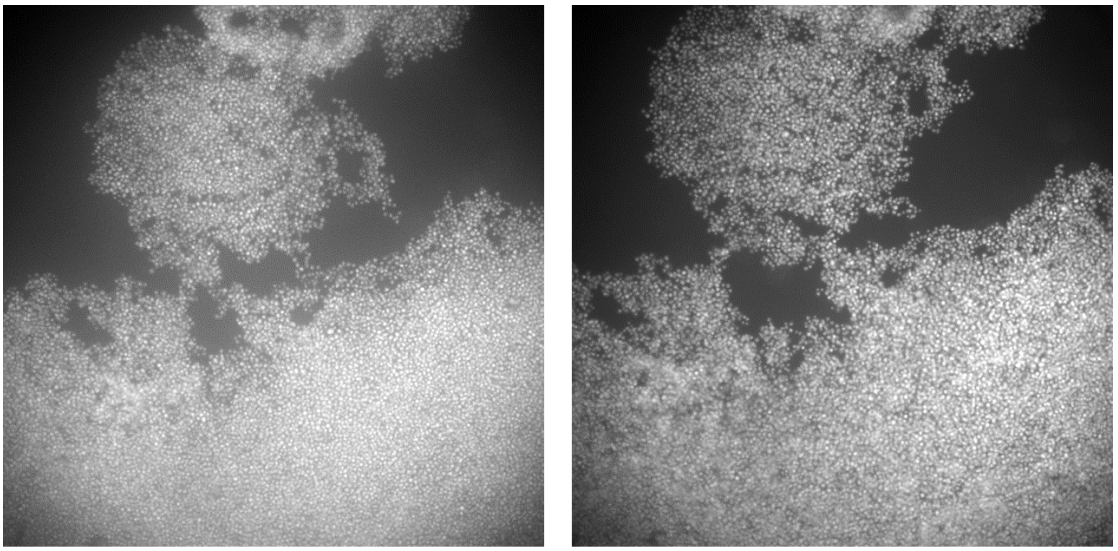

Figure B.1: ATDC5 cells in an aggregate at t=0 hrs and 22 hrs. Cells within the aggregate are structured into a monolayer, but spread out over time to increase their interstitial spacing. It should be appreciated, however, that the initial aggregate has near uniform fluorescent intensity, which changes to express higher fluorescent in local areas within the aggregate. This is likely a result of the cells reorganizing themselves into a multi-layered sheet toward the centre of the aggregate, whilst expanding towards the periphery.

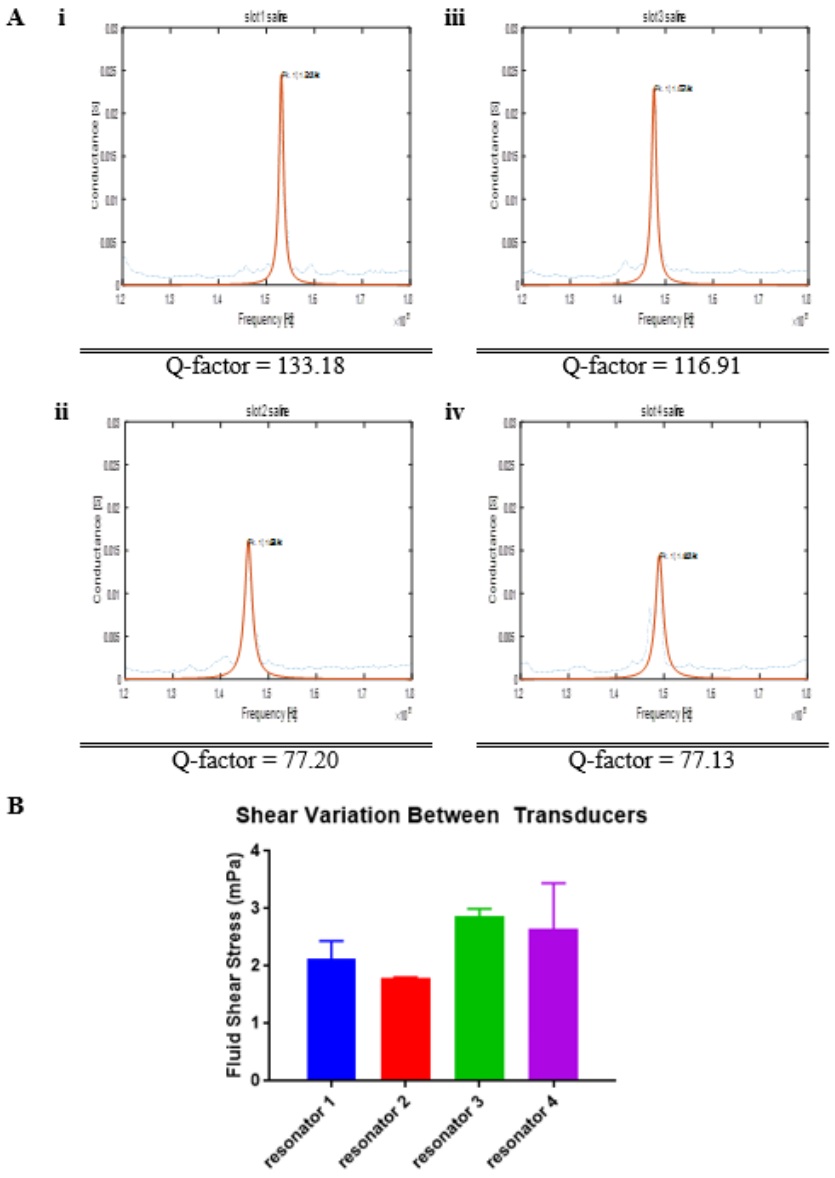

Figure B.2: (A) The reactance plots were acquired for the four resonators within the plate bioreactor plate to determine cavity resonance and q factor of the peaks. (B) While some difference in the conductance peaks was observed, the fluid shear at 100 kHz and 1 Hz sweep repetition rate across the resonators did not show significant differences in the mean values. Shear analysis for transducer 4 did demonstrate wide variance, which can likely be attributed to the image quality and subsequent tracking. All data points were constructed from n = 2 (mean ± SD).

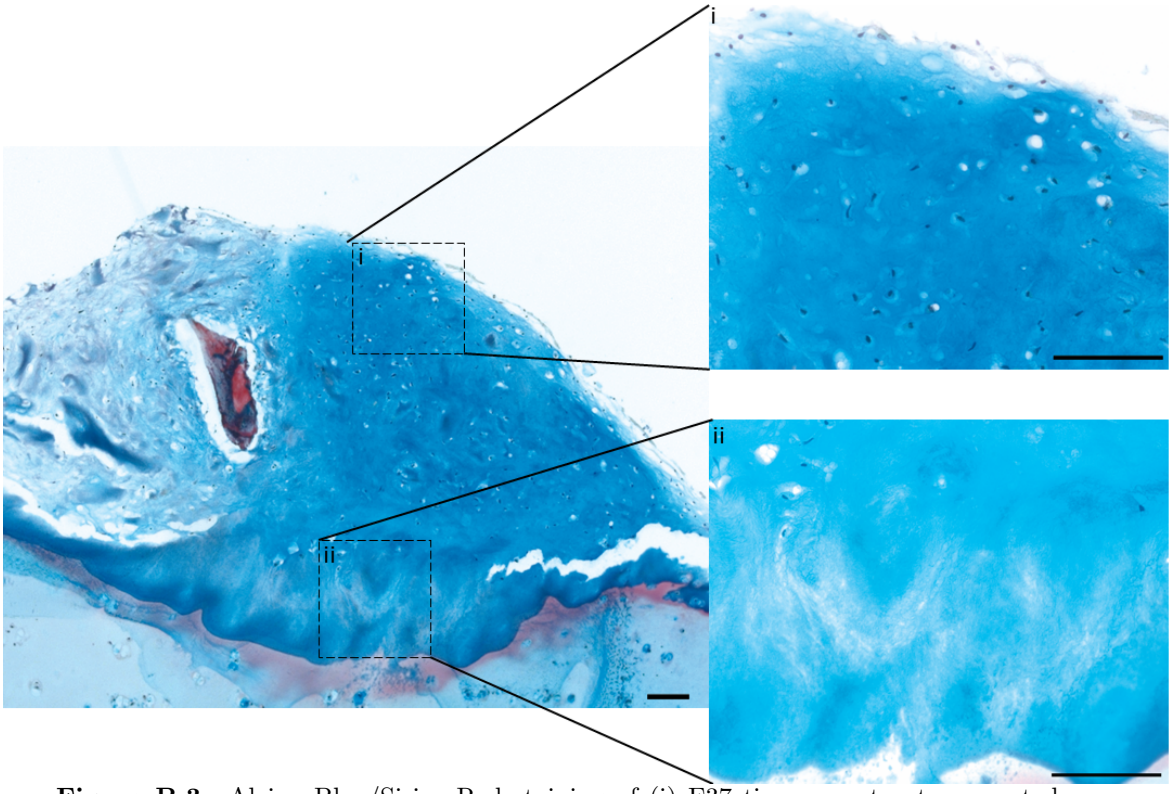

Figure B.3: Alcian Blue/Sirius Red staining of (i) F37 tissue construct, generated from a 21-day culture with 2 Hz sweep and PTHrP, integrated into an *ex vivo* defect model. The tissue was fixed following 6 weeks of culture within a transwell and mechanically tested prior to staining to assess the quality of integration into the native tissue structure. It was observed that the tissue managed to incorporate itself into the native structure (ii) over the course of the 6 week culture period. Scale bars = 100 µm